OPTOACOUSTIC DETECTION EMPLOYING STARK VOLTAGE MODULATION AND STARK POLARIZATION MODULATION

Thesis by

Michael Joseph Kavaya

In Partial Fulfillment of the Requirements

for the Degree of

Doctor of Philosophy

California Institute of Technology

Pasadena, California

1982

(Submitted November 30, 1981)

ACKNOWLEDGEMENTS

I wish to thank my thesis advisor, Professor William Bridges, for his help and support. I would also like to thank Dr. Robert Menzies for his generous academic and financial support.

I enjoyed many helpful discussions with my colleagues at the Jet Propulsion Laboratory: Dr. Jack Margolis, Dr. Michael Shumate, and Dr. Christopher Webster; and with my associates at Caltech: Arthur Chiou and Edgard Schweig. I would like to thank Ernest Nordquist for his excellent technical support, and Beth Cooper and Edith Huang for assistance with the word processing software.

I would also like to express my deep gratitude to Dr. Barbara Fass for many helpful and timely discussions.

I especially want to express my tremendous appreciation and love to my wife, Janet, who has injected boundless encouragement, support, joy, and love into my life since the day we met. Above all, I thank God for blessing me in so many ways.

ABSTRACT

The conventional chopped laser radiation technique of optoacoustic detection suffers from a sensitivity-limiting synchronous background signal. This thesis reports on theoretical and experimental studies of two novel optoacoustic modulation techniques designed to reduce the background signal and thereby improve the sensitivity. A specialized optoacoustic detector is described, which is capable of being operated in the conventional chopped-laser modulation mode as well as in the new Stark voltage modulation and Stark polarization modulation modes; experimental results are given using all three modes of operation. Stark voltage modulation produces more than two orders of magnitude improvement in sensitivity over conventional modulation under identical conditions. Even greater sensitivities are shown to be attainable. A basic theory of conventional optoacoustic detection is developed and then applied to the new optoacoustic modulation techniques. An introduction to and history of optoacoustic detection are also presented.

TABLE OF CONTENTS

1. INTRODUCTION

1.1 Guide to the Thesis

1.1.1 General Remarks

The past twenty years have witnessed a remarkable and exciting growth in the field of optoacoustic detection. The advent of the laser boosted the development of optoacoustic detection and resulted in a proliferation of new uses and improvements in the technique. It is surprising that this technology, which was first discovered by Alexander Graham Bell in 1880, took such a long time to achieve popularity.

Chapter 1 of this thesis provides the reader with an introduction to the principle of optoacoustic detection, describes some of the variations of the basic optoacoustic detector (OAD) which have been proposed or demonstrated, and outlines a brief history of optoacoustic detection. A glossary of symbols used in this work is also given.

Chapter 2 summarizes the physics of the signal generation process in an optoacoustic detector or spectrophone, the origin of the performance-limiting background signal, and the predicted sources of noise.

Chapter 3 describes the experimental apparatus used for this work, including the custom-designed Stark spectrophone, the condenser microphone, the carbon-dioxide laser, and the ammonia gas mixture which provided the necessary Stark effect.

Chapter 4 presents the results of operating the Stark spectrophone in the conventional chopped laser radiation mode.

Chapters 5 and 6 are devoted to two novel techniques of operating a spectrophone. They are, respectively, the Stark voltage modulated spectrophone and the

Stark polarization modulated spectrophone. First, the theory of the conventional spectrophone is modified to apply to the two new modulation techniques, and then, experimental results are reported and compared to the predictions of the theory and to the conventional modulation results.

Finally, Chapter 7 summarizes this work and states the conclusions which may be drawn.

1.1.2 Glossary of Symbols

a	thermal diffusion coefficient $\left(\frac{\omega}{2\beta}\right)^{\frac{1}{2}}$	m^{-1}
A	area	m^2
A_{eff}	effective capacitive area of condenser microphone	m^2
$A_j(\omega)$	normal pressure mode amplitudes	Pa
A_{ij}	Einstein spontaneous emission coefficients	s^{-1}
b_{ij}	collisional transition rates	s^{-1}
B_{ij}	Einstein stimulated emission coefficients	$m\ kg^{-1}$
c	speed of light in vacuum (2.998×10^8)	$m\ s^{-1}$
C	capacitance	F
C_b	biased microphone capacitance	F
C_v, C_p	specific heat at constant volume, pressure	$J\ kg^{-1}\ K^{-1}$
d	thickness	m
E	electric field intensity	$V\ m^{-1}$
f	acoustic frequency	s^{-1}
F	force	N
g	conductance	Ω^{-1}
g	gain	-
G	spectrophone responsivity	$V(W\ cm^{-1})^{-1}$
h	Planck's constant (6.625×10^{-34})	J-s
H	rate of heat input	$W\ m^{-3}$
i	$\sqrt{-1}$	-
I	Power density, intensity	$W\ m^{-2}$
$I(\nu)$	power density per unit frequency	$W\ m^{-2}\ Hz^{-1}$
J	current	A
J_g	preamplifier gate leakage current	A

k	thermal conductivity	$W\ m^{-1}\ K^{-1}$
k_j	$\omega_j u_s^{-1}$	m^{-1}
k_B	Boltzmann's constant (1.381×10^{-23})	$J\ K^{-1}$
l	length	m
l_c	cell length	m
l_h	acoustic thermal boundary layer $\left[\frac{2k}{\rho\omega C_p}\right]^{\frac{1}{2}}$	m
l_v	acoustic viscous boundary layer $\left[\frac{2\eta}{\rho\omega}\right]^{\frac{1}{2}}$	m
L_s	total surface loss	$J\ s^{-1}$
L_v	total volume loss	$J\ s^{-1}$
m	modulation coefficient	-
M	mass	kg
n	index of refraction	-
N	number density	m^{-3} , cm^{-3}
p	pressure	Pa, atm
p_A	ambient pressure	Pa
p_s	partial pressure of absorbing gas sample	Pa
$p_j(\vec{r})$	normal mode solutions of homogeneous wave equation	-
q	charge	A-s
q(z)	complex radius of curvature	m
Q	quality factor	-
r	radial coordinate	m
r_c	cell radius	m
r_d	diaphragm radius	m
r(z)	spherical radius of curvature	m
R	resistance	Ω
R_b	microphone bias resistance	Ω

R_h	heat conduction surface resistance	$m^2\ s\ kg^{-1}$
R_v	viscous surface resistance	$kg\ m^{-2}\ s^{-1}$
S	integrated spectral line intensity	cm
S_{oc}	open circuit microphone sensitivity	$V\ Pa^{-1}$
S_{mp}	coupled microphone-preamplifier sensitivity	$V\ Pa^{-1}$
t	time	s
t_c	thermal heat conduction time	s
t_r	trapezoid rise time	s
T	temperature	K
u	velocity	$m\ s^{-1}$
u_a	acoustic velocity	$m\ s^{-1}$
u_s	velocity of sound	$m\ s^{-1}$
U	energy	J
v	volts	V
v_b	microphone bias voltage	V
V	volume	m^3
V_c	spectrophone cell volume	m^3
V_e	equivalent volume	m^3
V_m	microphone volume	m^3
w(z)	beam spot size	m
w_0	minimum beam spot size	m
W	power	$J\ s^{-1}$
x_b	biased diaphragm-backplate separation	m
Y	tension	$N\ m^{-1}$
Z	impedance	Ω
$\alpha(\nu)$	linear attenuation coefficient	m^{-1} , cm^{-1}

β	thermal diffusivity $\frac{k}{\rho C_p}$	$m^2\ s^{-1}$
γ	half-width at half-maximum (HWHM) of spectral line	cm^{-1}
γ	$\frac{C_p}{C_v}$	-
δ	damping coefficient	$kg\ s^{-1}$
$\delta(x)$	Dirac delta function	x^{-1}
ε_0	permittivity of free space (8.854×10^{-12})	$F\ m^{-1}$
ζ	mol. transl. energy per unit vol.	$J\ m^{-3}$
η	dynamic viscosity	Pa-s, $kg\ m^{-1}s^{-1}$
κ	efficiency	-
λ	wavelength	m
μ	absorptivity	$atm^{-1}cm^{-1}$
ν	optical frequency	s^{-1}
ξ	(1-i)a	m^{-1}
ρ	mass density	$kg\ m^{-3}$
σ	absorption cross section	cm^2
τ	period, lifetime	s
τ_c	nonradiative relaxation time	s
τ_r	radiative relaxation time	s
Υ	electric dipole moment	A-s-m, Debye
Ψ	phase angle	radian
ω	radian frequency ($2\pi f$)	$rad\ s^{-1}$

$\tilde{A}$	phasor representation, $A(t) = \bar{A} + Re[\tilde{A}\ e^{-i\omega t}]$
$\bar{A}$	time average
$<A>$	spatial average

1.2 Optoacoustic Detection

1.2.1 The Principle of Optoacoustic Detection

When a gas sample absorbs radiation, the acquired energy may be lost by reradiation, may cause a photochemical change, or may serve to heat the sample. Any increase in the thermal (translational) energy corresponds to an increase in the gas pressure for a fixed volume cell ($pV = Nk_BT$). If the radiation is modulated at an audio frequency, a sound (pressure) wave is produced in the cell. Optoacoustic detection employs a microphone to detect this acoustic signal. The conventional optoacoustic detector or spectrophone is shown in Figure 1.1 and consists of a constant volume cell containing a sample to be investigated (solid, liquid or gas), one or more windows to allow incident radiation to interact with the sample, and a microphone to convert the pressure signal into electrical signals.

A simple experimental arrangement is shown in Figure 1.2. Monochromatic laser light is mechanically chopped and directed into the spectrophone. Assuming a gas sample partially absorbs the radiation, a portion of the absorbed energy will quickly be converted into translational energy of the gas molecules, thus causing a pressure modulation within the spectrophone at the same frequency as the mechanical chopper. The microphone converts this synchronous pressure signal into an electrical signal which is amplified and usually phase-synchronously detected. For small gas concentrations (absorption strengths), this output signal is proportional to the pressure of the absorbing sample gas, p_s, to the absorptivity $\mu(\nu)$ of the gas at the laser frequency ν, to the interaction length of the laser beam with the gas, l_c, and to the laser power W. The signal is inversely proportional to the spectrophone volume V_c.

There are many advantages to optoacoustic detection compared to conventional optical transmission measurements. The latter is limited by the requirement

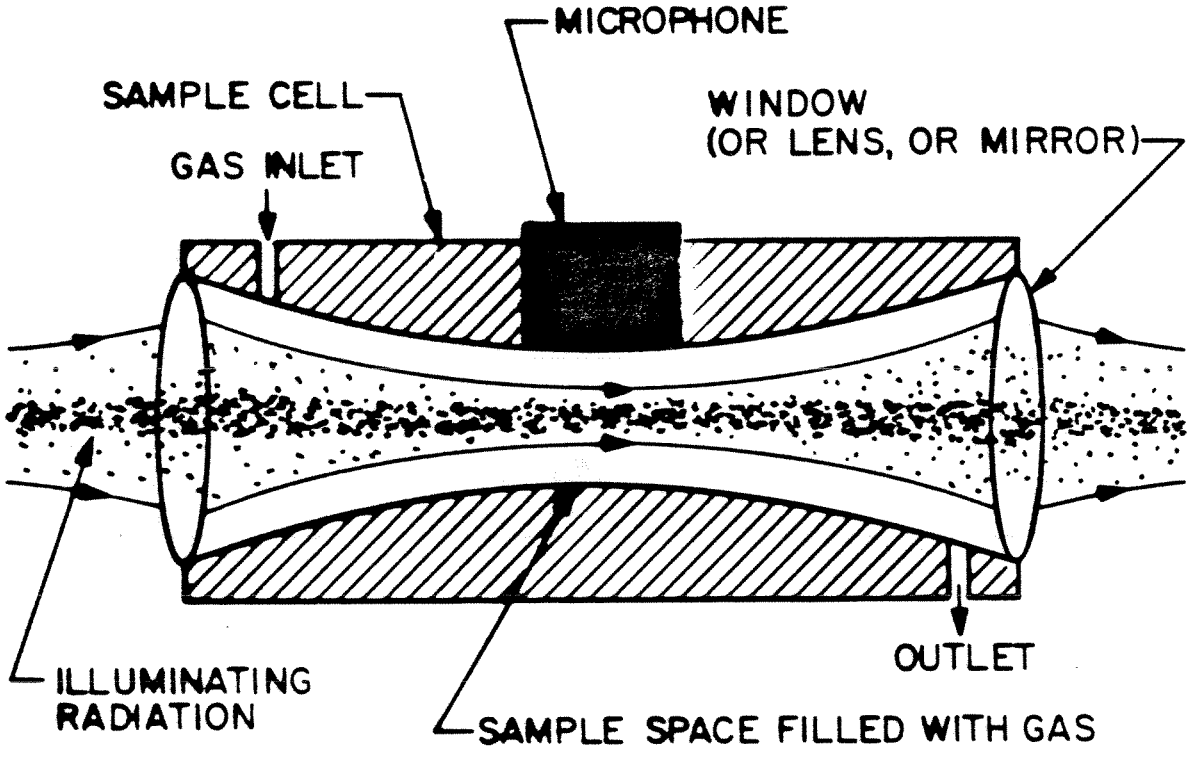

Figure 1.1. Schematic drawing of a simple optoacoustic detector or spectrophone.

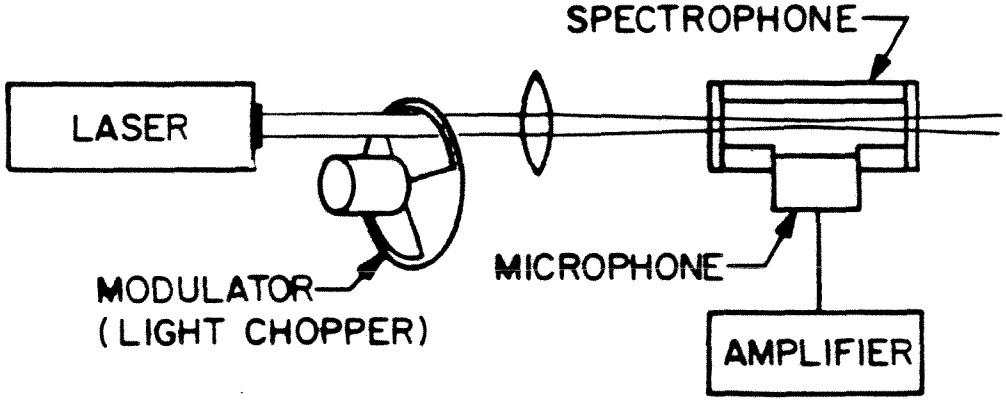

Figure 1.2. Block diagram of a typical optoacoustic experimental arrangement.

of measuring a small signal (at best 10^{-4}) on top of a large background signal. Optoacoustic detection, however, is similar to fluorescence detection in that the signal appears upon a (theoretically) zero background and, therefore, the sensitivity is greatly increased. For example, molecular absorptions that require kilometers of pathlength in conventional transmission spectroscopy (e.g. in a White cell) may be recorded with an optoacoustic cell that is only a cm or so in length. The two very sensitive techniques of optoacoustic detection and fluorescence detection are complementary in two ways:

(1) When no photochemical reactions occur, the added optoacoustic and fluorescence signals represent the total absorption signal;

(2) Optoacoustic detection is best suited at higher pressures due to its acoustic nature, while fluorescence detection favors lower pressures because of quenching.

Optoacoustic detectors are small, lightweight and relatively inexpensive. No optical-frequency detectors are required. They can be operated over a large dynamic range (eight orders of magnitude), and, because the output signal is proportional to the incident light intensity, there is no fundamental lower limit on the measurement of absorption strengths. Indeed, the high output power and collimation of lasers has produced a resurgence of interest in optoacoustic detection.

As with all detectors, optoacoustic detectors are subject to performance degradation due to noise and unwanted background signals. Each step in the process of generating the desired signal is subject to the addition of noise and background interference as shown in Figure 1.3. All spectrophones exhibit a synchronous signal even when filled with a nonabsorbing sample (or no sample at all). This background signal limits the sensitivity of the spectrophone in three ways:

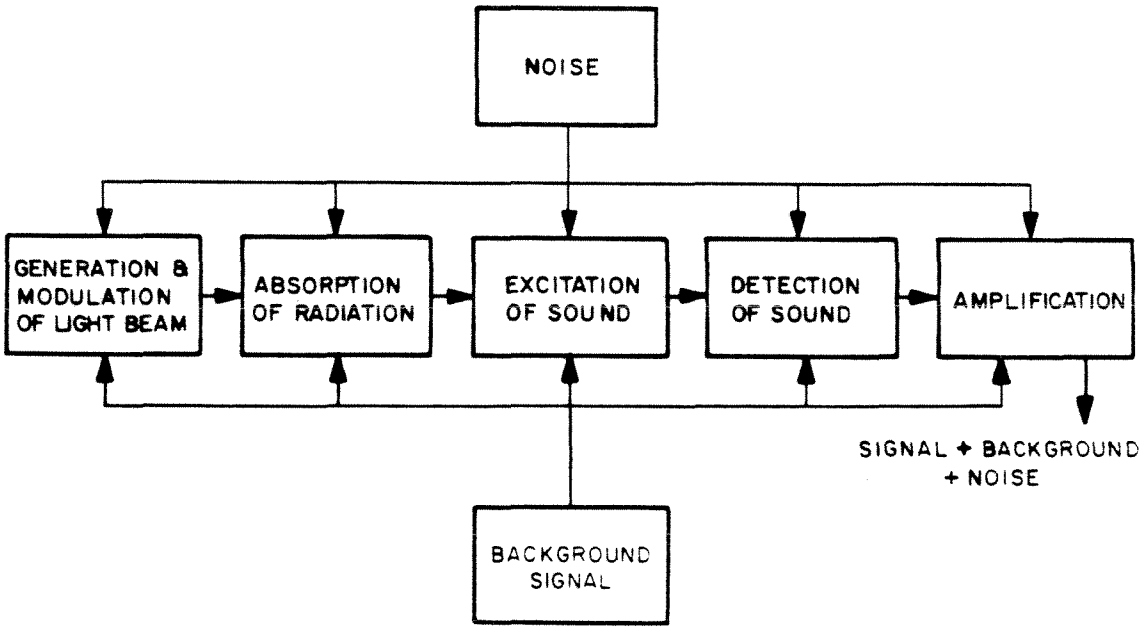

Figure 1.3. Block diagram of the optoacoustic signal generation process.

(1) It must be subtracted from the signal+background data, introducing the inherent inaccuracy associated with the subtraction of two almost equal numbers;

(2) It is difficult to maintain the exact experimental conditions, minus the absorbing gas, in order to measure the background signal;

(3) It may contribute to saturation of the signal processing electronics and, therefore, force an unwanted reduction in the laser power.

1.2.2 Spectrophone Configurations

Although the principle of optoacoustic detection is straightforward, a variety of different detectors and detection schemes have been proposed and described in the literature. These variations of the basic spectrophone experimental configuration (Figure 1.2) can be classified in terms of three goals:

(1) Improvement of the signal-to-noise ratio;

(2) Improvement of the signal-to-background ratio;

(3) Satisfaction of a specific application.

We may also label each idea as to whether it alters:

(1) The signal generation process;

(2) The spectrophone and/or experimental geometry;

(3) The signal detection method.

The basic experimental configuration consists of a mechanically-chopped cw laser which is directed into a constant volume cell where it is at least partially absorbed by the sample. A microphone mounted in the cell converts the resultant pressure fluctuations into electrical fluctuations. This electrical signal is phase-

synchronously detected at the chopping frequency. The primary limitation to this process is the synchronous background signal which is not due to absorption by the sample and which interferes with the measurement of the true absorption signal. In this basic spectrophone, the background signal is primarily the pressure signal generated by heating at the optical windows of the cell from the small absorption of the window material or contaminants on the window surface.

Many investigators have sought to increase the output signal of a spectrophone as a means to increase the signal-to-noise and/or the signal-to-background ratios. Dewey, et al [1] first reported on the operation of a cylindrical spectrophone at its natural acoustic resonant frequencies. The frequency of operation was controlled by the mechanical light chopper. They observed a sharp resonance peaking of the signal with a measured acoustic Q of 164 and claimed that the background signal could be discriminated against in this way. This technique has been used successfully by others [2,3] especially where a large volume is acceptable. A second method of increasing the signal is by arranging multiple passes of the laser beam through the spectrophone. This was first done by Goldan and Goto [2] who observed a factor of 10 increase in sensitivity. Other methods of increasing the signal include placing the spectrophone inside the cavity of a laser [4-6], and careful selection of the buffer gas [7]. Leslie and Trusty [6] reported a minimum detectable absorption of 7×10^{-8} cm^{-1} with a 10:1 SNR using an intracavity spectrophone.

An alternative approach to improving the signal-to-background ratio is to reduce the background signal. A number of clever techniques have been invented for this purpose. Deaton, Depatie and Walker [8] were the first to demonstrate a differential spectrophone in which there were two gas cells in series. The windows and gas mixture of each cell were identical except that one cell did not contain the absorbing species. The signal was taken as the modulated pressure difference between the two cells, and thus the identical background signals of each cell should

cancel out. Rosengren [9] provided a novel variation of this scheme with his "cross-path" spectrophone. The laser beam is directed through the spectrophone alternately between two paths which differ widely (10:1) in interaction length with the gas. In this way the desired pressure signal will arise from the large difference in absorption of the two paths while the undesired background (window absorption) signal will again cancel. Shtrikman and Slatkine [5] eliminated the windows altogether in a resonant intracavity spectrophone, but they also observed an increase in the detected room ambient acoustic noise.

All of the aforementioned ideas use a mechanical light chopper to modulate the incident laser power and thus modulate the absorption of energy by the sample. A number of other techniques replace the chopper with another form of modulator, for example, modulation of the absorptivity, $\mu(\nu)$. Dewey and Hocker [10] have proposed the modulation of the laser wavelength. To be successful, the laser power output and the spectrophone cell window absorption would have to remain fixed while the sample absorption changes with the laser wavelength shift. In many molecules, $\mu(\nu)$ can also be modulated with an external electric or magnetic field, i.e., the Stark and Zeeman effects. As applied to optoacoustic detection, these two forms of modulation were proposed by Patel and Kerl [11] and their successful use reported by Kavaya, Margolis and Shumate [12,13] and Bridges and Burkhardt [14], respectively. A fourth method of modulating $\mu(\nu)$ is to apply a constant electric or magnetic field to the sample and rotate the direction of polarization of the incident laser radiation. This technique, with an electric field, was demonstrated by Kavaya et al [13,15], and, with a magnetic field, by Bridges and Burkhardt [14].

Other special-purpose variations of the basic spectrophone have been reported; these include pulsed laser operation [16], the use of damping baffles to isolate the microphone from the window heating signal [16,17], a transversely excited spectrophone [18], an open-membrane spectrophone [19], and Helmholtz-

resonance enhanced detection [20]. Some of these alternate spectrophone configurations are shown in Figure 1.4.

1.2.3 The History of Optoacoustic Detection

1.2.3.1 Discovery and Early Work (1880)

In 1880, Alexander Graham Bell first reported "On the Production and Reproduction of Sound by Light" [21]. He and his assistant, Sumner Tainter, were investigating "that remarkable substance selenium" [22] which had recently been found to exhibit an illumination-dependent resistance. Bell's idea was to substitute the telephone for a galvanometer in observing the electrical effect of selenium and to interrupt a beam of sunlight falling on the selenium with a rotating perforated disk. He felt that by modulating the sunlight at an audible frequency, a sound should be heard from the telephone. He envisioned wireless communication by light between telephones "by the use of a parallel beam of light". He devised a voice-actuated device which modulated the amount of light passing through it and successfully transmitted a voice signal up to a distance of 213 meters. Using the perforated disk, he found that the signal continued despite placing two sheets of rubber in the beam of light (because of the transmitted infrared rays). He named the device "the Photophone", because "an ordinary beam of sunlight contains the operative rays".

During these experiments, Bell attempted to hear a sound from the selenium directly, but without success. He did, however, hear a distinct musical note from a sheet of hard rubber while holding it close to his ear in the intermittent beam. This led to rubber diaphragms, selenium disks, and many other investigations of the "Non-Electric Photonic Receivers". When the objects were placed in a sample cell, the sounds became stronger. Bell concluded that "sounds can be produced by the action of a variable light from substances of all kinds when in the form of thin diaphragms" and that "the molecular disturbance produced by light is chiefly a sur-

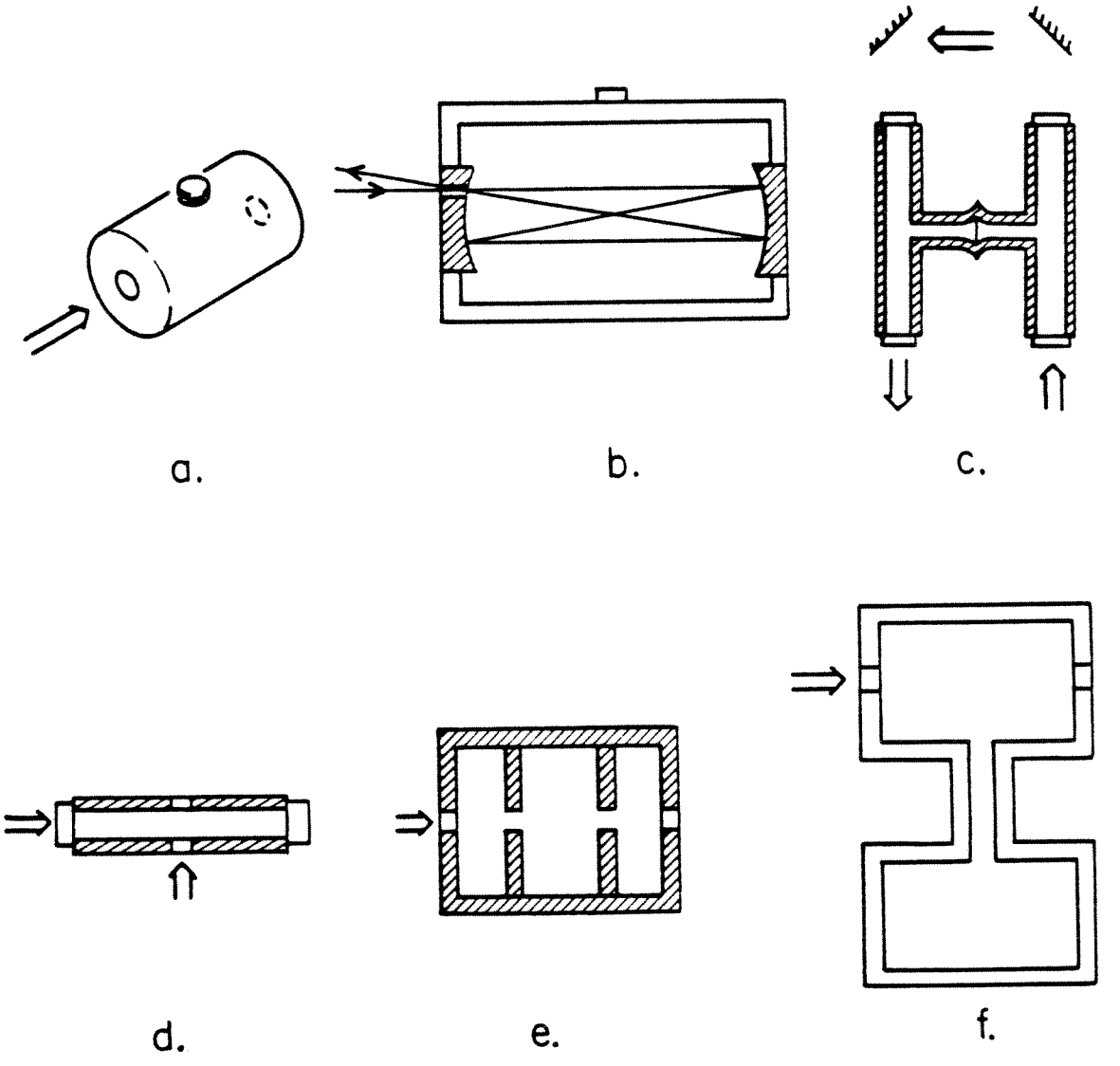

Figure 1.4. Various signal-to-noise and signal-to-background ratio improvement schemes: a) acoustically resonant cell, b) multiple-pass cell, c) differential cell, d) cross-path cell, e) cell with acoustic baffling, and f) Helmholtz resonance cell.

face action". He even succeeded in hearing a tone from an intermittent beam on the ear itself.

Bell and Tainter continued to develop and improve the photophone [23-28] and were joined in their investigation by Mercadier [29-36], Rontgen [37], Tyndall [38,39], Rayleigh [40], and Preece [41,42].

Mercadier [29] agreed with Bell that the phenomenon was primarily a surface effect, that it could be strengthened by blackening the absorbing surface, and that it resulted primarily from the red and infrared, or "caloric" wavelengths.

Tyndall [38] felt that the absorption of light by gases and vapors ought to produce the same musical sounds, and he demonstrated this in Bell's presence. He found that the use of glass lenses decreased the intensity of the sound, so he switched to silvered mirrors. He obtained sounds with many gases and vapors, including water vapor, and with many sources of light such as sunlight, a limelight, a candle, a hot coal or poker, and an incandescent platinum spiral.

Rayleigh [40] published a mathematical treatment of the plate-bending in Bell's experiments and concluded that the sounds were due to plate bending under unequal heating.

Preece [42] questioned whether the sounds were due to light or to radiant heat and he also questioned Rayleigh's explanation of plate-bending. His experiments with a number of materials using both a candle and a limelight showed that the disturbances are "produced by some thermic action rather than by any luminous effect" and that "the disk did not play a prime part in this phenomenon ... the result might be due wholly to an expansion and contraction of the air". He also produced sounds by placing a fine platinum wire inside a cavity and intermittently heating it with an electrical current. This led to a suggestion that the effect is due to contact of air molecules with the surface of the disk.

Bell disagreed with Preece [25,27,28] and supported Rayleigh's theory of plate-bending. He demonstrated the property of "sonorousness" in many solids, liquids, and gases and transmitted a voice signal for 40 meters using sunlight and a lamp-black photophone. In the case of solids, he stated that "the loudest sounds are produced from substances in a loose, porous, spongy condition, and from those that have the darkest or most absorbent colors". The sounds obtained from liquids were much weaker than those from solids or gases. To avoid confusion with the term "photophone", Bell suggested the term "radiophone" for apparatus producing sound from radiant energy and the terms "thermophone", "photophone", and "actinophone" for apparatus producing sound by thermal, luminous, or actinic (ultraviolet) rays respectively. Following Mercadier's lead, Bell passed sunlight through a prism and found that different substances require different portions of the spectrum to produce the strongest sonorous effects. He converted a spectroscope for this purpose and named the device a "spectrophone". Today the term "spectrophone" is used for all devices which convert light into sound, even in the absence of a spectroscope.

1.2.3.2 Renewed Interest (1938)

No further results were published for over 50 years until 1938 when three authors, in a relatively short period of time, independently reported using "radiophones" as a means of gas analysis.

Viengerov [43-47] developed a "spectrophone" or "optic-acoustical gas-analyser" which consisted of a Nernst filament, an optional filter, a chopper, an absorption cell coupled to a telephone earpiece, and an amplifier. He was able to detect 0.2% by volume CO_2 in N_2 and, later, 0.2 mg/l of ether vapor. He used a resonator coupled to the absorption cell to peak the signal and the filter to eliminate unwanted rays from the light source. He also devised a "differential" spectrophone consisting of two parallel absorption tubes and two parallel filter tubes which were alternated using a

mechanical chopper. He later improved his apparatus by using a heated platinum strip as a light source and a moving-coil microphone as a transducer. With a carbon arc source and a monochromator [45], he investigated the 2.7 μm and 4.3 μm absorption spectra of CO_2.

Pfund [48-50] followed Viengerov by one year in reporting on the detection of small concentrations of CO and CO_2. Using a jet of hot CO_2 as a source, and absorbing chamber, and a thermopile as a detector, he was able to detect less than 1 ppm of CO_2 in air. By detecting a temperature change in the gas rather than a pressure change, he simplified problems of acoustical noise isolation.

In 1943, Luft [51] described his work with a spectrophone which had begun five years earlier. Used for commercial gas analysis, his differential detector used two gas cells connected by a condenser microphone. His two radiation sources, heated nichrome wires, illuminated the cells through either a comparison tube or an analysis tube. His analysis tube contained only the component of the gas mixture to be measured. Luft also used his apparatus to measure absorption spectra of gases and vapors by converting his gas analyzer to use monochromatic radiation.

Gorelik [52], in 1946, published a paper which proposed using a spectrophone to investigate the rate of energy transfer in a gas between the vibrational and translational degrees of freedom. Using a physical argument and the conservation of energy, he showed that the amplitude and phase of the spectrophone signal depend on the modulation frequency in a way that yields information about the rate of energy transfer (i.e. the molecular collisional deactivation time).

The first measurements using Gorelik's proposed method were reported two years later by Slobodskaya [53]. She had adapted Viengerov's spectrophone and had measured the lifetimes of the excited vibrational CO_2 bands at 2.7, 4.3, and 14.8 μm. Slobodskaya continued her work in the area of relaxation times [54-61] and was

joined by Cottrell [62-64], Read [63-66], Jacox and Bauer [67], and others using a number of absorbing and buffer gases and light sources.

1.2.3.3 Laser Era (1968)

The discovery of the laser in 1960 injected new life into the development and uses of the spectrophone or optoacoustic detector. For the first time, high power light sources were available which were monochromatic and collimated. Because the linewidths of lasers are usually narrow compared to the absorption lines of gases, a mapping of the absorption lineshape was now possible with tunable lasers. The inherently good collimation of the light from a laser permitted the energy to be focused into a much smaller sample volume and even reflected many times through the sample in a multi-pass configuration. Both features provided greater sensitivity of detection. The high power levels available from lasers also increased the sensitivity for detection of very small absorption strengths.

The first reported use of laser illumination of a spectrophone was by Kerr and Atwood [68] in 1968. Using a pulsed ruby laser, they were able to measure absorption strengths of water vapor in air down to 10^{-6} cm^{-1}. With a cw CO_2 laser, they measured CO_2 in N_2 down to their background level of 5 x 10^{-8} cm^{-1}. They attributed their background to a window signal. Investigation of absorption spectra and coefficients has continued to the present. Deaton et al [8] have used a differential spectrophone design in their study of methane and nitrous oxide at DF (deuterium fluoride) laser wavelengths (3.8 μm) and they reported a background signal of 3.3 x 10^{-9} $cm^{-1}W^{-1}$. Stella et al [4] inserted a spectrophone in the cavity of a dye laser in order to study overtone transitions of CH_4 and NH_3. Menzies and Shumate and their coworkers [3,69] have used a resonant spectrophone extensively to study the absorption of water vapor at CO (5 μm) and CO_2 (10 μm) laser wavelengths. The analogous microwave optoacoustic effect was used to investigate molecular oxygen

by Diebold and McFadden [70]. Patel et al [71] employed a spin-flip Raman laser at 5.3 μm to examine the excited-state spectroscopy of NO. The need for an airport, bus terminal, etc., explosives detector has led Crane [72] to investigate the absorption of vapors from explosive materials at CO_2 laser wavelengths. Many other studies of gases and vapors have been done. We will discuss solids and liquids in a later section.

A related path of investigation is the detection of ultra-low concentrations of gas using a spectrophone. Kreuzer [73] first reported using a number of laser sources to detect methanol vapor and methane in air. He was able to detect 2×10^{-7} parts methane in air using a homemade absorption cell and microphone. Rosengren [74] published a theoretical model of the opto-acoustic gas concentration detector and then, akin to Pfund, proposed an opto-thermal gas concentration detector [75] which measures the temperature variations in the cell rather than pressure variations. Max and Rosengren [76] later described a resonant gas-concentration detector and predicted a background signal equivalent to only 10^{-4} ppm of ammonia using a 1 watt CO_2 laser and a 10 second integration time. Shtrikman and Slatkine [5] operated an intracavity optoacoustic trace gas analyzer using a CO_2 laser and a resonant spectrophone. Detection of 0.12 ppb SO_2 in air was reported by Koch and Lahmann [77] using a frequency-doubled dye laser and a multipass cell. Recently, an excellent paper on the detection of air pollution with optoacoustic detectors was published by Adamowicz and Koo [78].

Although the early spectrophone work (1880's) included solids, liquids, and gases, a revival of interest in solids and liquids did not occur until 1973 when Rosencwaig [79] reported using a xenon lamp and monochromator to illuminate solid samples in a cell containing an electret microphone. He reported absorption spectra of many solids including carbon black and Rhodamine-B and theorized that de-excitation and relaxation processes in solids could be studied. The investigation

of solids with spectrophones has become known as photoacoustic spectroscopy (PAS) versus the name optoacoustic spectroscopy for work with gases. Many PAS experiments and theoretical studies have since been published. In 1977, Murphy and Aamodt [80] deposited an electrically conductive substrate (similar to Preece's platinum wire) in their PAS cell as a means of calibrating it. They named this instrument a photothermophone. Wong, et al [81] investigated the subsurface structure of turbine blades using PAS and were able to detect hidden flaws. Other investigators have been concerned with electron-phonon interactions in semiconductors [82], dichroism spectra of $NdMoO_4$ [83], and photoacoustic imaging of microscopic structures [84], to name a few.

A fourth area of optoacoustic research has been photochemistry. Using a xenon lamp and monochromator, DeGroot, et al [85] have studied aldehyde photochemistry and have uncovered new intermediate reactives during photolysis of acetaldehyde. Similarly, Kaya, et al [86] have worked with biacetyl; and both groups have varied chopping frequency, cell pressure and wavelength in order to learn about the reactions taking place. Colles, et al [87] studied gas phase continuous photolysis of nitromethane with a tunable dye laser and Black et al [88] reported on collisionless multiphoton dissociation of SF_6.

A great deal of research has been done using the optoacoustic effect to investigate relaxation rates, absorption spectra, detection and photochemistry of gases, liquids and solids; recently, a number of researchers have branched into new areas. These include the study of multiple photon excitation [89], absolute quantum yields [90], laser line shape parameters [91], Stark and Zeeman modulation in spectrophones [11,12], aerosol absorption [92], new far-infrared laser lines [93], Fourier Transform spectroscopy [94], photoacoustic microscopy [95], liquid-solid phase transitions [96], photoacoustic Raman spectroscopy [97], Helmholtz resonances in OAD cells [98] (see also Viengerov [45]), thin-film absorption [99], OAD in optical

fibers [100], laser power monitors [101], detection of ferromagnetic resonance [102], laser-induced damage in optical materials [103], detection of circular dichroism [104], Doppler-free OAD [105], nanosecond time-resolved PAS [106], sub-millimeter microwave spectroscopy [107], overtone chemistry [108], and forbidden electronic transitions [109,110].

1.2.3.4 Patents

A number of patents have been issued concerning the optoacoustic phenomenon. Alexander Graham Bell [111-113] received three patents on his invention of the photophone. In 1972, Atwood and Kerr [114] patented the "Laser Excited Spectrophone". Also in 1972, Kreuzer [115] patented the technique of detecting the OAD pressure signal at a frequency which is a harmonic (e.g. second) of the modulation frequency and, in 1974, Kreuzer [116] patented the OAD technique of measuring each concentration in a mixture of known gases. W.E. Bell [117,118] patented the intra-laser cavity spectrophone and a normalization technique for using it. C.F. Dewey [119] patented the acoustically resonant spectrophone. Rosencwaig [120] was issued a patent in 1976 for the photoacoustic technique of analyzing solids. Rosengren [9] patented the cross-path spectrophone and both Rosencwaig [121] and Dewey [10] received their second patents for an improved photoacoustic cell and for a wavelength modulation technique, respectively. In 1978, Shumate [122] patented a differential spectrophone design. Also that year, Bell [123] received his third patent for a number of techniques of modulating the properties of the fluid within a spectrophone, and Bridges and Burkhardt [124] received a patent for the technique of Zeeman (or Stark) modulation. Amer [125] proposed investigating nonabsorbing gases by doping the gas mixture with a small amount of absorbing gas. Murphy and Aamodt [126] patented a self-calibrating PAS cell, and Kimble and Roessler [127] patented a detector with a large static cavity coupled to a small dynamic OAD cell to allow resonant excitation advantages while preserving fast response. Margolis and

Shumate [128] patented the technique of Stark-modulation to enhance molecular discrimination in a spectrophone and Kavaya [129] patented a spectrophone with a varying electric field along the optical axis which allows real-time recording of Stark spectra. Horiba [130] received a patent for an intra-laser cavity differential spectrophone.

1.2.3.5 Review Articles

A number of review papers have followed the development of optoacoustic and photoacoustic detection. These include Delany [131], Kaiser [132], Read [66], Somoano [133] and Patel [134].

1.2.3.6 Books

To date, three books have been devoted to optoacoustic detection. They are the 1968 work by Gorelik and Sakharov (in Russian) [135], the 1977 book edited by Pao [136], and the recent book by Rosencwaig [137]. Other books which discuss or are related to this field include Cottrell and McCoubrey [138], Hill and Powell [139], Smith, Jones and Chasmar [140], Mitra and Bendow [141], Hinkley [142], Rao [143], Marton [144], Zewail [108], and DiBartolo [145].

1.2.3.7 Dissertations

A list of Ph.D. dissertations and Masters theses related to optoacoustic detection is given in references 146-163.

1.3 Chapter 1 References

[1] C.F. Dewey, Jr., R.D. Kamm and C.E. Hackett: Appl. Phys. Lett. 23(11), 633-635(1973)

[2] P.D. Goldan and K. Goto: J. Appl. Phys. 45(10), 4350-4355(1974)

[3] M.S. Shumate, R.T. Menzies, J.S. Margolis and L.-G. Rosengren: Appl. Opt. 15(10), 2480-2488(1976)

[4] G. Stella, J. Gelfand and W.H. Smith: Chem. Phys. Lett. 39(1), 146-149(1976)

[5] S. Shtrikman and M. Slatkine: Appl. Phys. Lett. 31(12), 830-831(1977)

[6] D.H. Leslie and G.L Trusty: Applied Optics 20(11), 1941-1947(1981)

[7] L.J. Thomas III, M.J. Kelly, and N.M. Amer: Appl. Phys. Lett. 32(11), 736-738(1978)

[8] T.F. Deaton, D.A. Depatie and T.W. Walker: Appl. Phys. Lett. 26(6), 300-303(1975)

[9] L.-G. Rosengren: "Method and Apparatus for Background Signal Reduction in Opto-Acoustic Absorption Measurement", U.S. Patent 3,995,960 (Dec. 7, 1976)

[10] C.F. Dewey, Jr. and L.O. Hocker: "Opto-Acoustic Spectroscopy Employing Amplitude and Wavelength Modulation", U.S. Patent 4,051,371 (Sept. 27, 1977)

[11] C.K.N. Patel and R.J. Kerl: Appl. Phys. Lett. 30(11), 578-579(1977)

[12] M.J. Kavaya, J.S. Margolis and M.S. Shumate: Appl. Opt. 18(15), 2602-2606(1979)

[13] M.J. Kavaya, J.S. Margolis and M.S. Shumate: "Optoacoustic Detection Using Stark Modulation", paper WC9-1 presented at the OSA topical conference on Photoacoustic Spectroscopy in Ames, Iowa (Aug. 1, 1979)

[14] T.J. Bridges and E.G. Burkhardt: Opt. Comm. 22(2), 248-250(1977)

[15] M.J. Kavaya and J.S. Margolis: NASA Tech Briefs 4(1), 46(1979)

[16] C.W. Bruce, B.Z. Sojka, B.G. Hurd, W.R. Watkins, K.O. White and Z. Derzko: Appl. Opt. 15(12), 2970-2972(1976)

[17] C.F. Dewey, Jr.: Optical Engineering 13(6), 483-488(1974)

[18] N. Ioli, P. Violino and M. Meucci: J. Phys. E: Sci. Instrum. 12, __(1979)

[19] S.O. Kanstad and P.-E. Nordal: Infrared Physics 19, 413-422(1979)

[20] R.W. Shaw: Appl. Phys. Lett. 35(3), 253-255(1979)

[21] A.G. Bell: "On the Production and Reproduction of Sound by Light", Amer. Assoc. Proc. 29, 115(1880); Amer. J. Sci. 20, 305(1880); Annales de Chimie 21 399(1880); Telegr. Engin. J. 9, 404(1880); Moniteur Scientifique 23, 97(1881); J. Amer. Elect. Soc. 3, 3(1880)

[22] A.G. Bell: "Selenium and the Photophone", Nature 22, 500(1880)

[23] A.G. Bell: Paris Acad. Sci. Comptes Rendus 91, 726(1880)

[24] A.G. Bell: Paris Acad. Sci. Comptes Rendus 91, 595(1880)

[25] A.G. Bell: "Upon the Production of Sound by Radiant Energy", Amer. J. Sci. 21, 463(1881); Annales de Chimie 23, 397(1881); Nature 24, 42(1881); Paris Acad. Sci. Comptes Rendus 92, 1206(1881); Phil. Mag. 11, 510(1881); J. Franklin Institute of Pennsylvania 111, 401(1881)

[26] A.G. Bell: "The Photophone", Canadian Naturalist 9, 397(1881); London J. Soc. Arts 29, 38(1880); Science __,130(Sept. 11, 1880)

[27] A.G. Bell: "The Spectrophone", Washington Phil. Soc. Bull. 4, 143(1881); Science __, 242(May 28, 1881); Smithsonian Misc. Coll. 25, Art. 1(1883)

[28] A.G. Bell: "Upon a modification of Wheatstone's Microphone and its applicability to Radiophonic Researches", Washington Phil. Soc. Bull. 4, 183(1881); Amer. J. Sci. 22, 87(1881); Nature 24, 302(1881); Annales de Chimie 25, 135(1882); Smithsonian Misc. Coll. 25, Art. 1(1883)

[29] E. Mercadier: "On Radiophony", Paris Acad. Sci. Comptes Rendus 91, 929(1880); 982(1880); 92,409(1881); 450(1881); 1224(1881); 1226(1881); Paris Soc. Phys. Seances , 184(1880); Phil. Mag. 11, 78(1881)

[30] E. Mercadier: Annales Telegraph 7, 544(1880); 8, 44(1881); 8, 167(1881); J. de Physique 10, 53(1881); 147(1881); 234(1881); Paris Soc. Phys. Seances , 38(1881); 122(1881)

[31] E. Mercadier: Paris Acad. Sci. Comptes Rendus 92, 705(1881)

[32] id.: p.789

[33] id.: p.1407

[34] id.: 93, 457(1881)

[35] id.: p.541

[36] id.: Telegr. Engin. J. 10, 333(1881)

[37] W.C. Rontgen: "On Tones Produced by the Intermittent Irradiation of a Gas", Ann. Physik U. Chemie 12, 155(1881); Philos. Mag. 11, 308(1881)

[38] John Tyndall, F.R.S.: "Action of an Intermittent Beam of Radiant Heat upon Gaseous Matter", Royal Soc. Proc. 31, 307(1881); Archives Sci. Phys. Nat. 5, 113(1881); Chemical News 43, 63(1881); Revue Scientif. 1, 204(1881); Nature 23, 374(1881); Les Mondes 54, 315, 357(1881); Royal Instit. Proc. 10, 175(1884)

[39] John Tyndall, F.R.S.: 'Further Experiments on the Action of an Intermittent

Beam of Radiant Heat on Gaseous Matter. Thermometric Measurements.", Royal Soc. Proc. 31, 478(1881)

[40] Lord Rayleigh: "The Photophone", Nature 23, 274(1881)

[41] W.H. Preece: "The Photophone and the Conversion of Radiant Energy into Sound", Telegr. Engin. J. 9, 363(1880)

[42] W.H. Preece: "On the Conversion of Radiant Energy into Sonorous Vibrations", Proc. Royal Soc. London 31, 506(1881); Nature 23, 496(1881); Annales de Chimie 24, 253(1881)

[43] M.L. Viengerov: Dokl. Akad. Nauk SSSR 19, 687(1938)

[44] id.: IZVEST Akad. Nauk SSSR (Physics) 4, 94(1940)

[45] id.: Dokl. Akad. Nauk SSSR 46, 182(1945)

[46] id.: Dokl. Akad. Nauk SSSR 51, 195(1946)

[47] id.: Zavodskaya Laboratoriya 13, 426(1947)

[48] A.H. Pfund: Science 90, 326(1939)

[49] A.H. Pfund and C.L. Gemmill: Bull. Johns Hopkins Hosp. 67, 61(1940)

[50] W.G. Fastie and A.H. Pfund: J. Opt. Soc. Am. 37, 762(1947)

[51] K.F. Luft: Zeit. tech. Physik 24, 97(1943)

[52] G. Gorelik: Dokl. Akad. Nauk SSSR 54, 779(1946)

[53] P.V. Slobodskaya: Izv. Akad. Nauk SSSR Fiz. 12, 656(1948)

[54] id.: Dokl. Akad. Nauk SSSR 120, 1283(1958)

[55] P.V. Slobodskaya and E.S. Gasilevich: Opt. Spectrosc. 7, 58(1959)

[56] id.: 8, 358(1960)

[57] P.V. Slobodskaya: Opt. Spectrosc. 22, 14(1967)

[58] P.V Slobodskaya and N.F. Tkachenko: Opt. Spectrosc. 26, 105(1969)

[59] P.V. Slobodskaya: Opt. Spectrosc. 34, 391(1973)

[60] P.V. Slobodskaya and E.N. Rityn: Opt. Spectrosc. 38, 297(1975)

[61] id.: 47, 591(1979)

[62] T.L. Cottrell: Trans. Farad. Soc. 46, 1025(1950)

[63] T.L. Cottrell: I.M. MacFarlane, A.W. Read, and A.H. Young, Trans. Farad. Soc. 62, 2655(1966)

[64] T.L. Cottrell, I.M. MacFarlane and A.W. Read: Trans. Farad. Soc. 63, 2093(1967)

[65] M.G. Ferguson and A.W. Read: Trans. Farad. Soc. 61, 1559(1965)

[66] A.W. Read: Advan. Mol. Relax. Processes 1, 257(1967-68)

[67] M.E. Jacox and S.H. Bauer: J. Phys. Chem. 61, 833(1957)

[68] E.L. Kerr and J.G. Atwood: Appl. Opt. 7, 915(1968)

[69] R.T. Menzies and M.S. Shumate: Appl. Opt. 15, 2025(1976)

[70] G. Diebold and D.L. McFadden: Appl. Phys. Lett. 29, 447(1976)

[71] C.K.N. Patel, R.J. Kerl and E.G. Burkhardt: Phys. Rev. Lett. 38, 1204(1977)

[72] R.A. Crane: Appl. Opt. 17, 2097(1978)

[73] L.B. Kreuzer: J. Appl. Phys. 42, 2934(1971)

[74] L.-G. Rosengren: Infrared Physics 13, 109(1973)

[75] id.: p. 173

[76] E. Max and L.-G. Rosengren: Opt. Comm. 11, 422(1974)

[77] K.P. Koch and W. Lahmann: Appl. Phys. Lett. 32, 289(1978)

[78] R.F. Adamowicz and K.P. Koo: Appl. Opt. 18, 2938(1979)

[79] A. Rosencwaig: Opt. Comm. 7, 305(1973)

[80] J.C. Murphy and L.C. Aamodt: Appl. Phys. Lett. 31, 728(1977)

[81] Y.H. Wong, R.L. Thomas and G.F. Hawkins: Appl. Phys. Lett. 32, 538(1978)

[82] C.C.. Ghizoni, M.A.A. Siqueira, H. Vargas and L.C.M. Miranda: Appl. Phys. Lett. 32, 554(1978)

[83] D. Fournier, A.C. Boccara and J. Badoz: Appl. Phys. Lett. 32, 640(1978)

[84] H.K. Wickramasinghe, R.C. Bray, V. Jipson, C.F. Quate and J.R. Salcedo: Appl. Phys. Lett. 33, 923(1978)

[85] M.S. DeGroot, C.A. Emeis, I.A.M. Hesselman, E. Drent and E. Farenhorst: Chem. Phys. Lett. 17, 332(1972)

[86] K. Kaya, W.R. Harshbarger and M.B. Robin: J. Chem. Phys. 60, 4231(1974)

[87] M.J. Colles, A.M. Angus and E.E. Marinero: Nature 262, 681(1976)

[88] J.G. Black, E. Yablonovitch and N. Bloembergen: Phys. Rev. Lett. 38, 1131(1977)

[89] G.P. Quigley: Opt. Lett. 4, 84(1979)

[90] R.S. Quimby and W.M. Yen: J. Appl. Phys. 51, 1780(1980)

[91] R.L. Abrams: Appl. Phys. Lett. 25, 609(1974)

[92] D.M. Roessler and F.R. Faxvog: Appl. Opt. 19, 578(1980)

[93] G. Busse and R. Thurmaier: Appl. Phys. Lett. 31, 194(1977)

[94] G. Busse and B. Bullemer: Infrared Physics 18, 255(1978)

[95] L.D. Favro, P.K. Kuo, J.J. Pouch and R.L. Thomas: Appl. Phys. Lett. 36, 953(1980)

[96] J.F. McClelland and R.N. Kniseley: Appl. Phys. Lett. 35, 121(1979)

[97] D.R. Siebert, G.A. West and J.J. Barrett: Appl. Opt. 19, 53(1980)

[98] N.C. Fernelius: Appl. Opt. 18, 1784(1979)

[99] E.L. Kerr: Appl. Opt. 12, 2520(1973)

[100] J.A. Burt, K.J. Ebeling and D. Efthimiades: Opt. Comm. 32, 59(1980)

[101] G. Busse and S. Perkowitz: Intl. J. of Infrared and Millimeter Waves 1, 139(1980)

[102] C. Evora, R. Landers and H. Vargas: Appl. Phys. Lett. 36, 864(1980)

[103] H.E. Bennett, A.J. Glass, A.H. Guenther and B. Newnam: Appl. Opt. 19, 2375(1980)

[104] J.D. Saxe, T.R. Faulkner and F.S. Richardson: Chem. Phys. Lett. 68, 71(1979)

[105] A. Di Lieto, P. Minguzzi and M. Tonnelli: Opt. Comm. 31, 25(1979)

[106] M.G. Rockley and J.P. Devlin: Appl. Phys. Lett. 31, 24(1979)

[107] A.V. Burenin: Izvestiya Vysshikh Uchebnykh Zavedenii Radiofizika 17(9), 1291(Sept. 1974)

[108] K.V. Reddy, R.G. Bray, and M.J. Berry: "Dye Laser-Induced Photochemistry", in "Advances in Laser Chemistry", ed. by A.H. Zewail (Springer-Verlag, Berlin, 1978) pp. 48-61

[109] R.N. Dixon, D.A. Haner, and C.R. Webster: Chem. Phys. 22, 199(1977)

[110] C.R. Webster: New Scientist 73, 383(Feb. 1977)

[111] A.G. Bell: "Apparatus for Signaling and Communicating, called Photophone", U.S. Patent 235,199 (Dec. 7, 1880)

[112] A.G. Bell and S. Tainter: "Photophone Transmitter", U.S. Patent 235,496 (Dec.

14, 1880)

[113] A.G. Bell and S. Tainter: "Photophonic Receiver", U.S. Patent 241,909 (May 24, 1881)

[114] J.G. Atwood and E.L. Kerr: "Laser Excited Spectrophone", U.S. Patent 3,659,452 (May 2, 1972)

[115] L.B. Kreuzer: "Measurement of Gas Impurity Concentration by Infrared Absorption Spectroscopy", U.S. Patent 3,700,890 (Oct. 24, 1972)

[116] L.B. Kreuzer: "Measurement of Concentrations of Components of a Gaseous Mixture", U.S. Patent 3,820,901 (June 28, 1974)

[117] W.E. Bell: "Laser Absorption Spectroscopy", U.S. Patent 3,893,771 (July 8, 1975)

[118] W.E. Bell: "Laser Spectroscopy", U.S. Patent 3,911,276 (Oct. 7, 1975)

[119] C.F. Dewey, Jr.: "Detecting Trace Gaseous Species Acoustically in Response to Radiation from an Intense Light Source", U.S. Patent 3,938,365 (Feb. 17, 1976)

[120] A. Rosencwaig: "Methods and Means for Analyzing Substances", U.S. Patent 3,948,345 (Apr. 6, 1976)

[121] A. Rosencwaig: "Photo Acoustic Cell", U.S. Patent 4,028,932 (June 14, 1977)

[122] M.S. Shumate: "Differential Optoacoustic Absorption Detector", U.S. Patent 4,067,653 (Jan. 10, 1978)

[123] W.E. Bell: "Laser Absorption Sprectroscopy Employing Varying Absorption Conditions", U.S. Patent 4,068,125 (Jan. 10, 1978)

[124] T.J. Bridges and E.G. Burkhardt: "Spectrophone with Field Tuning of Absorption Cell", U.S. Patent 4,105,919 (Aug. 8, 1978)

[125] N.M. Amer: 'Method and Apparatus for Optoacoustic Spectroscopy", U.S. Patent 4,163,382 (Aug. 7, 1979)

[126] J.C. Murphy and L.C. Aamodt: 'Self-calibrating Photoacoustic Apparatus for Measuring Light Intensity and Light Absorption", U.S. Patent 4,184,768 (Jan. 22, 1980)

[127] H.J. Kimble and D.M. Roessler: 'Resonant Optoacoustic Spectroscopy Apparatus", U.S. Patent 4,200,399 (Apr. 29, 1980)

[128] J.S. Margolis and M.S. Shumate: 'Stark Cell Optoacoustic Detection of Constituent Gases in a Sample", U.S. Patent 4,234,258 (Nov. 18, 1980)

[129] M.J. Kavaya: 'Stark-Effect Spectrophone for Continuous Absorption Spectra Monitoring", U.S. Patent 4,253,769 (Mar. 3, 1981)

[130] A. Horiba: "Optoacoustic Analyzer", U.S. Patent 4,253,770 (Mar. 3, 1981)

[131] M.E. Delany: 'The Optic-Acoustic Effect in Gases", Sci. Progr. 47, 459(1959)

[132] R. Kaiser: "On the Theory of the Spectrophone", Canadian J. Phys. 37, 1499(1959)

[133] R.B. Somoano: 'Photoacoustic Spectroscopy of Condensed Matter", Angew. Chem. Int. Ed. Engl. 17, 238(1978)

[134] C.K.N. Patel: 'Laser Detection of Pollution", Science 202, 157(1978)

[135] Gorelik, D.O. and Sakharov, B.B. (1968): 'The Optoacoustic Effect in Physical-Chemical Measurements", Gosstandarta, Leningrad

[136] Pao, Y.-H., editor (1977): "Optoacoustic Spectroscopy and Detection", Academic Press, New York

[137] Rosencwaig, A. (1980): 'Photoacoustic and Photoacoustic Spectroscopy", Chemical Analysis Series, Vol. 57, John Wiley & Sons, New York

[138] Cottrell, T.L. and McCoubrey, J.C. (1961): "Molecular Energy Transfer in Gases", Butterworths, London

[139] Hill, D.W. and Powell, T. (1968): "Non-Dispersive Infra-Red Gas Analysis in Science, Medicine, and Industry", Plenum Press, New York

[140] Smith, R.A., Jones, F.E. and Chasmar, R.P. (1968): "The Detection and Measurement of Infra-Red Radiation", Clarendon Press, Oxford

[141] Mitra, S.S. and Bendow, B. (1975): "Optical Properties of Highly Transparent Solids", Plenum Press, New York, Section VI, pages 405 and 451

[142] Hinkley, E.D., editor (1976): "Laser Monitoring of the Atmosphere", Springer-Verlag, Berlin; see chapter 6, "Techniques for Detection of Molecular Pollutants by Absorption of Laser Radiation" by Hinkley, E.D., Ku, R.T. and Kelley, P.L.

[143] K. Narahari Rao, editor (1976): "Molecular Spectroscopy: Modern Research", Volume II, Academic Press, New York; see chapter 2.2, "New Methods in Submillimeter Microwave Spectroscopy" by A.F. Krupnov and A.V. Burenin

[144] Marton, L., editor (1978): "Advances in Electronics and Electron Physics", Volume 46, Academic Press, New York; see "Photoacoustic Spectroscopy" by Rosencwaig, A., page 207

[145] B. DiBartolo, editor (1980): "Radiationless Processes", Volume 62, (Plenum Press, New York), see A. Rosencwaig: "Photoacoustics and Deexcitation Processes in Condensed Media", p. 431

[146] M.L. Viengerov (1940): State Optical Institute, Leningrad

[147] G.C. Turrell (1954): "Determination of the Vibrational Lifetime of CO by the Spectrophone Method", Department of Chemistry, Oregon State College, Corvallis, Oregon

[148] W.D. Jones (1957): "Vibrational Relaxation Time Studies on CO by the Infrared Spectrophone Method", Oregon State College, Corvallis

[149] M.E. Delaney (1959): University of London

[150] W.E. Woodmansee (1961): "A Variable Frequency Spectrophone Study of Carbon Monoxide", Oregon State College

[151] J.C. Kent (1962): "Infrared Spectrophone Studies of Vibrational Relaxation in CO, CO-Argon, and CO-N_2 Mixtures", Purdue University, West Lafayette, Indiana

[152] A.D. Wood (1963): "A Spectrophone Investigation of the Collisional-Vibrational Relaxation Time of Carbon Monoxide Gas", Purdue University, West Lafayette, Indiana

[153] H.R. Long (1966): "Radiation-Driven Acoustic Disturbances in a Confined Gas", Engineer's Dissertation, Stanford University

[154] Powell (1966): University of London

[155] E. Hey (1967): University of Heidelberg

[156] D.L. Compton (August 1969): "Radiatively Driven Acoustic Waves in a Gas in a Cylindrical Tube - Theory and Experiment at Resonance", SUDAAR 385, Stanford University

[157] G.T. Chapman (August 1970): "Radiatively Driven Acoustic Waves in a Gas in a Cylindrical Tube - Theory and Experiment for the Untuned Condition", SUDAAR 407, Stanford University

[158] R.D. Kamm (1973): Master's Thesis, Massachusetts Institute of Technology

[159] K.T. Yano (1973): Stanford University

[160] E. Monahan (1974): Master's Thesis, University of Texas

[161] J.C. Peterson (1976): Master's Thesis, "A Differential Spectrophone of Unique Design", Ohio State University, Columbus

[162] J.C. Peterson (June 1978): "A Study of Water Vapor Absorption at CO_2 Laser Frequencies Using a Differential Spectrophone and White Cell", Electro Science Laboratory, Ohio State University, Columbus

[163] C.R. Webster (1978): "Molecular Spectroscopy with a cw Dye Laser", University of Bristol (UK)

2. CONVENTIONAL SPECTROPHONE THEORY

2.1 Signal Generation and Detection

2.1.1 Introduction

The novel spectrophone configurations and their advantages discussed later in this report can best be appreciated when compared to the operation of a conventional spectrophone. In this section we will treat the process of signal generation and detection in a typical conventional spectrophone in order to provide that background.

The signal is obtained by the following steps:

(1) Radiation is modulated and directed into the spectrophone;

(2) This radiation is partially absorbed by the gas sample and converted into excess translational energy;

(3) The temporal and spatial character of the excess translational energy produces a time-varying pressure in the cell;

(4) The pressure signal is converted into an electrical signal by a microphone.

As is usually the case, any attempt to model the true physical situation in a spectrophone in complete detail leads to intractable mathematical difficulties. For this reason, many simplifying idealizations and approximations are necessary in the development of a simple and mathematically tractable model. These assumptions and their influence on the validity and accuracy of the results will be stated as they are made in the model development that follows. Once an understanding of the physics of optoacoustic detection is obtained, it will be possible to explore the merits, limitations, and optimum parameters of the conventional spectrophone and also of the alternative spectrophone configurations reported here.

2.1.2 Illumination and Modulation

The first step in generating an optoacoustic signal is to provide the radiation which illuminates the absorbing sample inside the cell. While this radiation could be treated with complete generality, practical sources available at present limit researchers to only a few variations in the parameters which specify the radiation: intensity, spectrum, spatial coherence, modulation, and both longitudinal and transverse spatial profile.

Prior to the invention of the laser, investigators were limited to relatively low intensity, incoherent, and broadband sources of illumination. Infrared radiation was provided by thermal sources and could be filtered to yield a typical bandwidth of 30 GHz and a typical radiance of 4×10^{-3} $Wcm^{-2}sr^{-1}$ [1]. By contrast, single-mode visible continuous lasers may easily have linewidths of less than 1 MHz and radiances of $10^{6} - 10^{9}$ $Wcm^{-2}sr^{-1}$, infrared CO_2 lasers have exhibited linewidths less than 100 Hz and radiances of $10^{6} - 10^{9}$ $Wcm^{-2}sr^{-1}$ for laboratory type lasers, while pulsed lasers can easily achieve radiances greater than 10^{14} $Wcm^{-2}sr^{-1}$ [1,2]. The narrow linewidth attainable with a laser allows the assumption that only a single molecular transition is involved in the absorption of the radiation. The spatial coherence of laser radiation, and the small focused beam diameters that it makes possible, allow construction of minimum volume spectrophones and the investigation of spatial variations within the sample.

The spatial variation of the radiation is described by its amplitude dependence both along (z) and perpendicular (x,y) to its direction of propagation. It is common to assume no variation in intensity with z, a good approximation for low absorption. The actual variation along the z-axis is given by Beer's law [3]. If we let N(z) be the number density [cm^{-3}] of absorbing molecules at position z, $\sigma(\nu,z)$ be the absorption cross section [cm^{2}] per molecule at frequency ν and position z, $I(\nu, 0)$ be the incident

intensity [$Wm^{-2}Hz^{-1}$] at z=0, and $I(\nu,l)$ be the intensity at z=l, and we define

$$\alpha(\nu, z) = N(z)\sigma(\nu, z) \tag{2.1}$$

as the linear attenuation coefficient [cm^{-1}] of the gas at frequency ν and position z, then for collimated radiation,

$$I(\nu,l) = I(\nu, 0)\ \exp\left[-\int_0^l \alpha(\nu, z)\ dz\right] \quad . \tag{2.2}$$

This equation is valid when $\sigma(\nu, z)$ is independent of $I(\nu, 0)$ and N(z). If the source is not monochromatic, then the total intensity at z=l is obtained by integrating (2.2) over the frequency bandwidth. It is common practice to express $\alpha(\nu, z)$ as the product of the absorptivity, $\mu(\nu, z)$ [$atm^{-1}cm^{-1}$], and the pressure, p_s [atm], of the absorbing gas sample:

$$\alpha(\nu, z) = \mu(\nu, z)p_s \quad . \tag{2.3}$$

The simplest transverse intensity distribution would be a beam with uniform amplitude within the spectrophone boundaries and zero amplitude outside these boundaries. Although impossible to realize in practice, this case is often assumed. A realistic transverse distribution is given by the lowest order Gaussian mode of a laser:

$$E_{00}(x, y, z) \propto \sqrt{\frac{2}{\pi}}\ \frac{1}{w(z)} \exp\left[\frac{-i\pi(x^2 + y^2)}{\lambda q(z)}\right] \exp\left[-i\left[\frac{2\pi z}{\lambda} - \Psi(z)\right]\right] \quad , \tag{2.4}$$

where

$$w(z) = w_0 \left[1 + \left(\frac{\lambda z}{\pi w_0^2}\right)^2\right]^{\frac{1}{2}} \quad , \tag{2.5}$$

$$\frac{1}{q(z)} = \frac{1}{r(z)} - i\frac{\lambda}{\pi w^2(z)} = \frac{1}{z + \frac{i\pi w_0^2}{\lambda}} \quad , \tag{2.6}$$

$$r(z) = z + \frac{1}{z}\left(\frac{\pi w_0^2}{\lambda}\right)^2 \quad , \tag{2.7}$$

and

$$\Psi(z) = \tan^{-1}\left(\frac{\lambda z}{\pi w_0^2}\right) \quad . \tag{2.8}$$

The variable r(z) is the spherical radius of curvature, q(z) is the complex radius of curvature, w(z) is the beam's spot size, and w_0 is the minimum spot size where the beam's wavefront is planar. The transverse intensity variation is

$$I_{00}(x, y) \propto E_{00}E_{00}^* \propto \frac{2}{\pi}\frac{1}{[w(z)]^2}\exp\left[\frac{-2(x^2 + y^2)}{[w(z)]^2}\right] \quad . \tag{2.9}$$

The spot size, w(z), is the radius at which the amplitude is reduced by a factor of e^{-1} (= 0.37) and the intensity by a factor of e^{-2} (= 0.14) from the value on axis. Thus an aperture of diameter 2w(z) would pass 86% of the beam's power while a diameter of 3w(z) would pass 99%.

The temporal parameters of the illuminating radiation are very important both for the theoretical modeling and for the actual use of the spectrophone. The modulation can be periodic or nonperiodic. Very short duration pulses are often

useful for investigating extremely rapid molecular or electronic processes of the sample. However, the present study is concerned only with illumination having some periodic waveform, characterized by a modulation depth, and a fundamental frequency and harmonic content. Often, phase-synchronous signal detection is employed to select the signal component at the fundamental frequency or one of its harmonics. Typical idealized periodic waveforms used in spectrophone analysis include sinusoidal, trapezoidal, and square waveforms. These waveforms may also represent intensity modulation of the absorption within the spectrophone produced by frequency modulation of the illuminating radiation.

Let us consider these three forms of intensity modulation with a modulation depth of 100%, and period τ. For a sinusoidal intensity variation of period τ,

$$I(t) = \frac{1}{2} + \frac{1}{2} \cos\frac{2\pi t}{\tau} \quad . \tag{2.10}$$

The only nonzero Fourier coefficients are $a_0 = 1$ and $a_1 = 1/2$. The phase-synchronous signal at $f = \tau^{-1}$ is proportional to a_1.

Both the square wave and triangular wave are limiting cases of the trapezoidal waveform so they need not be derived separately. For a typical trapezoid with parameters shown in Figure 2.1, the Fourier coefficients are

$$a_0 = 1 \qquad a_1 = \frac{2}{\pi}\mathrm{sinc}\frac{t_r}{\tau} \qquad b_n = 0 \quad , \tag{2.11}$$

where

$$\mathrm{sinc}(x) \equiv \frac{\sin(\pi x)}{\pi x} \quad . \tag{2.12}$$

(There are harmonic coefficients a_2, a_3, $\cdots$, but we are not interested in them

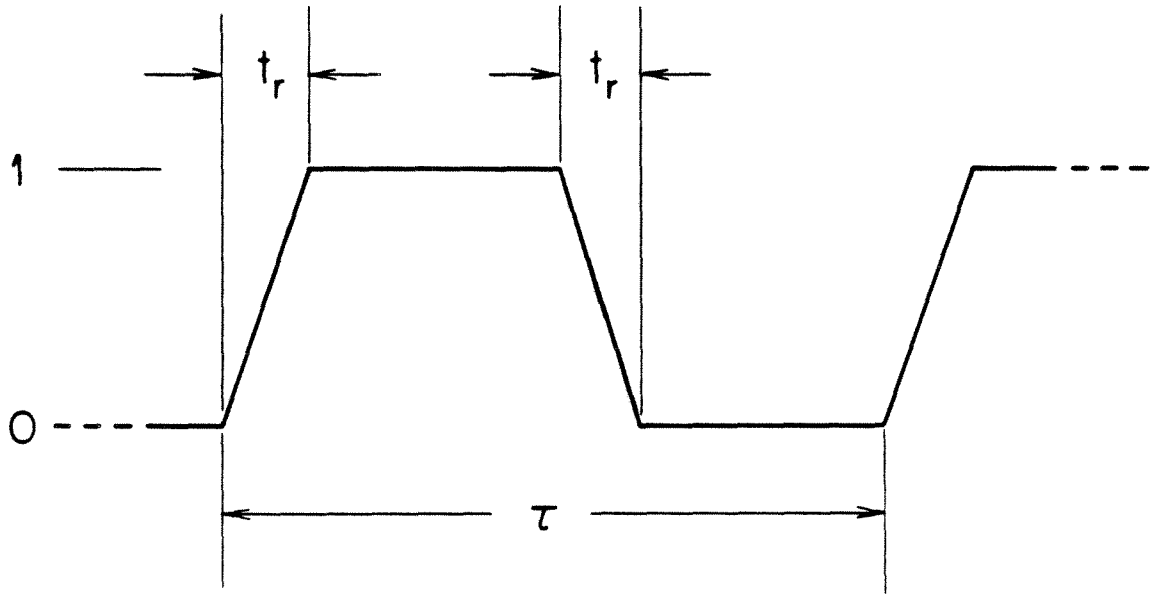

Figure 2.1. Example of a trapezoidal modulation waveform.

when we employ fundamental synchronous detection). The phase-synchronous signal at τ^{-1} is proportional to a_1, and varies from a maximum of $2/\pi = 0.64$ when $t_r = 0$ (square-wave) to a minimum of $4/\pi^2 = 0.41$ when $t_r = 0.50\tau$ (triangle). It is equal to the sinusoidal case ($a_1 = 1/2$) when $t_r = 0.38\tau$.

The most common experimental technique for modulating the intensity of a laser is to direct it through a mechanical chopper. While the trapezoidal waveform described above is often employed as an idealization for this situation, it is possible to derive the resulting time variation of a sharp edge cutting through a cylindrical Gaussian beam. Figure 2.2 shows the geometry of a chopper blade intersecting a Gaussian laser beam. The transmitted intensity waveform is

$$I(t) = \frac{1}{2}\left\{1 + \mathrm{erf}\left[\frac{\sqrt{2}\ r_0\cos\left(\omega t + \frac{\pi}{4}\right)}{w}\right]\mathrm{erf}\left[\frac{\sqrt{2}\ r_0\sin\left(\omega t + \frac{\pi}{4}\right)}{w}\right]\right\}, \qquad (2.13)$$

where r_0 is the separation between the optical axis and the chopper axis. Equation (2.13) represents an idealized infinitely large chopper with laser radiation passing through one quadrant only, and fails as an accurate model if the beam size approaches the dimensions of the chopper. The intensity waveform of Equation (2.13) is plotted in Figure 2.3 for various values of the parameter $\frac{r_0}{w}$. For $\frac{r_0}{w} > 5$, the waveform resembles a trapezoid, but with rounded corners. A Fourier series expansion yields:

$$a_0 = 1 \qquad a_1 \approx \frac{-2}{\pi}\cos\left[2\cos^{-1}\left(\frac{1.83\ w}{\sqrt{2}\ r_0}\right)\right] \qquad b_n = 0 \ . \qquad (2.14)$$

(Again, we are not interested in a_2, a_3, $\cdots$ here). The approximation is valid for $\frac{r_0}{w} > \frac{1.83}{\sqrt{2}} = 1.29$. The factor 1.83 arises since $\mathrm{erf}(1.83) \approx 0.99$, and this value was

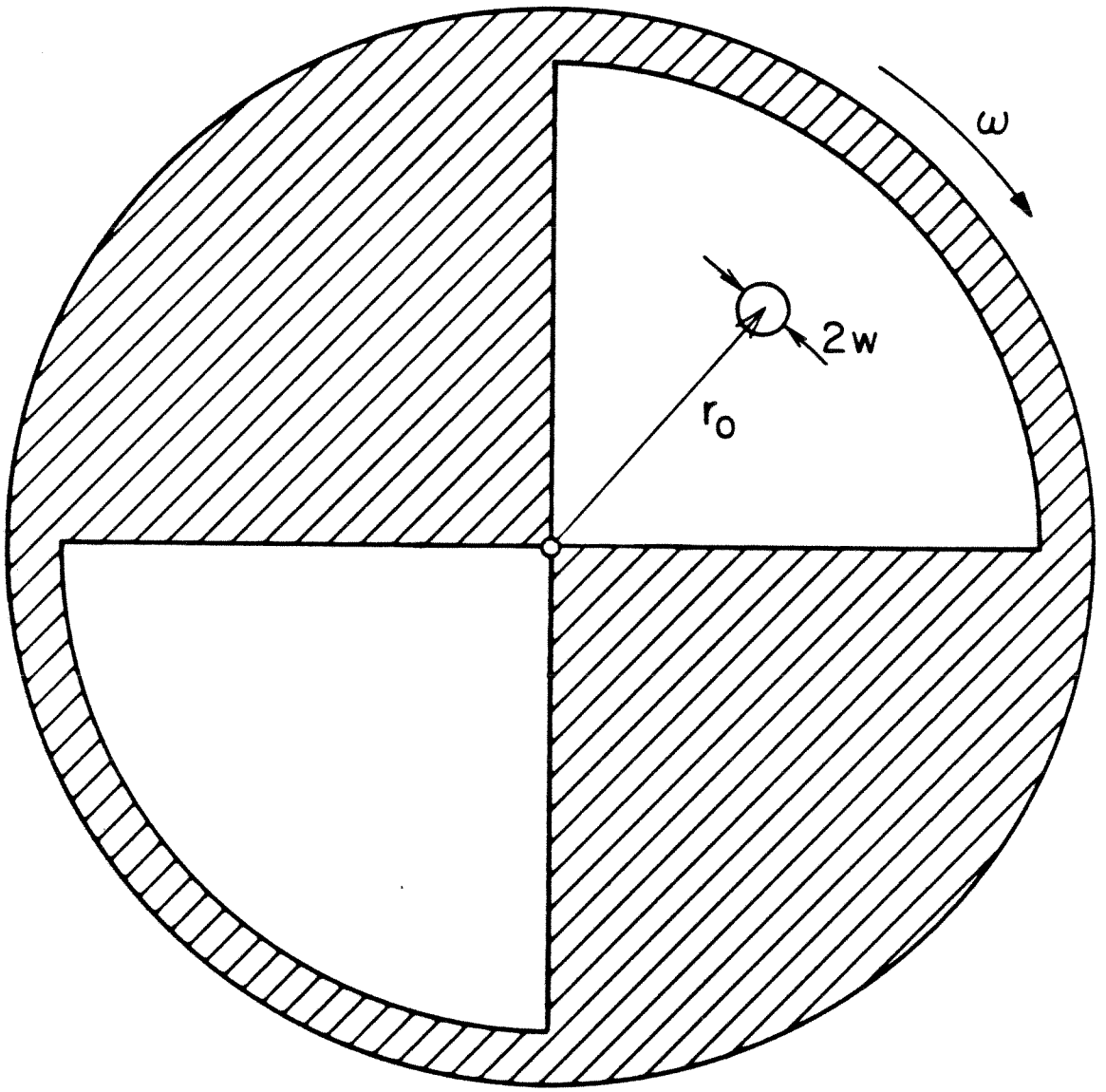

Figure 2.2. Pictorial drawing of a mechanical chopper perpendicular to a Gaussian laser beam.

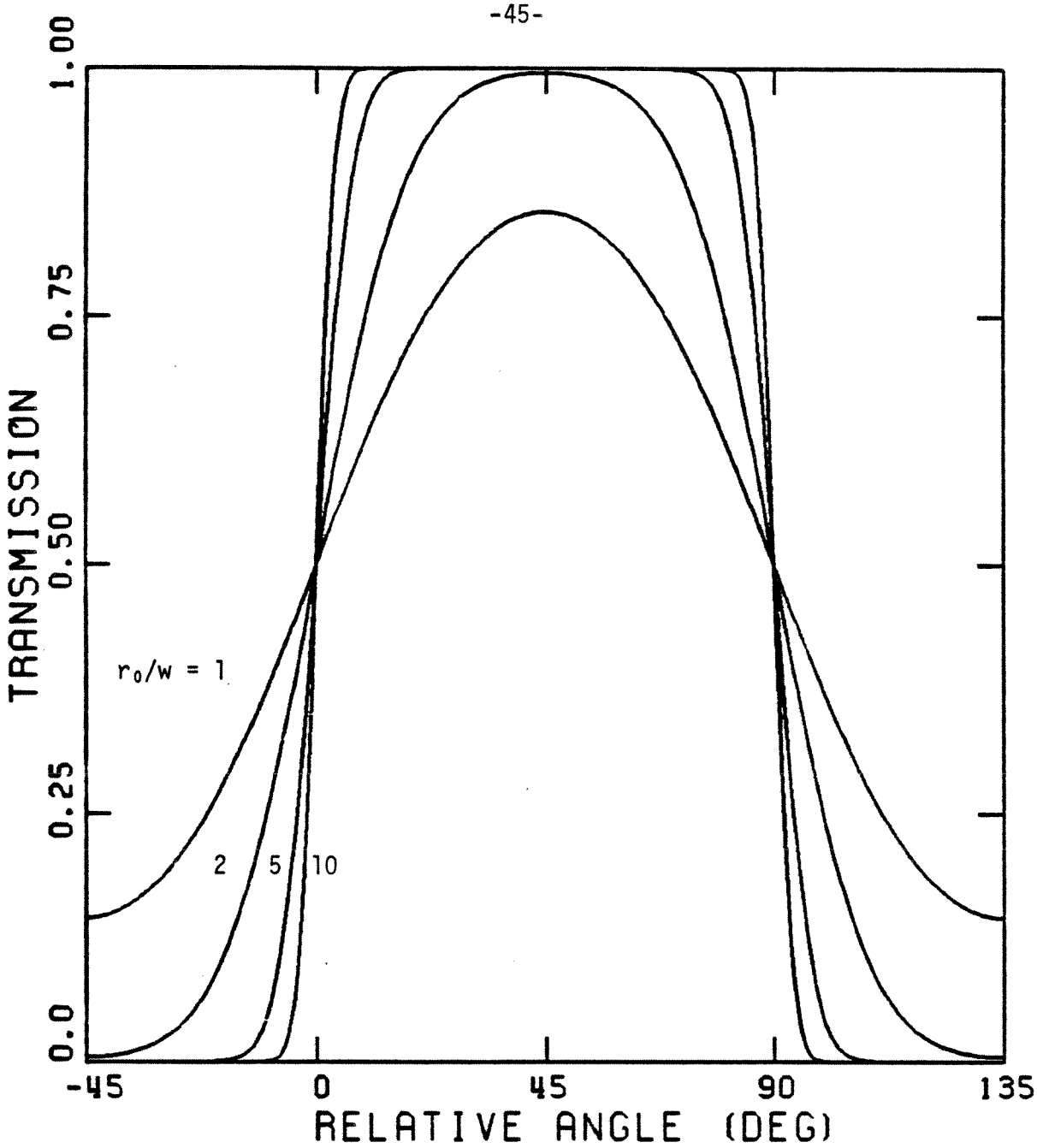

Figure 2.3. Graph showing the Gaussian beam intensity transmitted through a four-quadrant chopper vs. the relative angle between the blade and the beam for various values of the ratio of the beam-chopper separation, r_0, to the beam spot size w.

arbitrarily chosen as a limit of integration. For $\frac{r_0}{w} >> 1.29$, equation (2.14) becomes

$$a_1 \approx \frac{2}{\pi} \cos\left[\frac{1.83\sqrt{2}\, w}{r_0}\right] . \qquad (2.15)$$

As $\frac{r_0}{w} \rightarrow \infty$, $a_1 \rightarrow \frac{2}{\pi}$, and we again have the square-wave case. Equivalence to the sinusoidal case ($a_1 = 0.5$) is attained when $\frac{r_0}{w} = 3.95$.

2.1.3 Absorption of Radiation

The second step in the generation of the optoacoustic signal is the partial absorption of the illuminating radiation by the gas. When a gas molecule absorbs a photon of frequency ν, it undergoes a transition from the ground state energy U_0 to the excited state energy U_1, where $U_1 - U_0 = h\nu$. The molecule can then lose this energy and return to the ground state in one of four ways:

(1) Through radiation of a photon;

(2) Through a photochemical event;

(3) Through a collision which excites a similar molecule from U_0 to U_1;

(4) Through a collision which increases the kinetic (translational) energy of both molecules : (heating).

The optoacoustic signal is the result of the fourth process, which we will treat in this section. The increase in translational energy (heating) of the gas will be modulated at the same frequency as the illuminating radiation. Later, we will see that this heating produces a pressure signal which can be detected by a sensitive microphone.

Although a multiple energy-level examination of the absorption process has been outlined [4], we will consider a two-level system in this section [4,5]. We let

levels U_0 and U_1 contain N_0 and N_1 molecules per unit volume, respectively, where $N_0 + N_1 = N$ = constant. The radiative transition rates from level i to level j are given by

$$\frac{I(\nu)}{c} B_{ij} + A_{ij} \quad , \tag{2.16}$$

where $I(\nu)$ is the input light intensity per unit frequency, c is the speed of light, B_{ij} are the Einstein coefficients for stimulated emission, and A_{ij} are the Einstein coefficients for spontaneous emission, with $A_{01} = 0$ since $U_1 > U_0$. Apart from degeneracy factors, $B_{ij} = B_{ji}$. The nonradiative, collisionally-induced transition rates from level i to level j are given by b_{ij}. The rate of change of the population of both levels is given by

$$\frac{d}{dt} N_0(t) = -N_0(t)[B_{01} I(\nu, t) c^{-1} + b_{01}] + N_1(t)[B_{10} I(\nu, t) c^{-1} + A_{10} + b_{10}] \quad , \tag{2.17}$$

and

$$\frac{d}{dt} N_1(t) = -\frac{d}{dt} N_0(t) \quad , \tag{2.18}$$

since $N_0 + N_1 = N$. At room temperature, $b_{01} \approx 0$. If we define

$$\tau_r = \frac{1}{A_{10}} \quad , \quad \tau_c = \frac{1}{b_{10}} \quad , \tag{2.19}$$

as the relaxation times for radiative and collisional transitions from level 1, respectively, and

$$\frac{1}{\tau} = \frac{1}{\tau_r} + \frac{1}{\tau_c} \quad , \tag{2.20}$$

as the total relaxation time, then (2.17) and (2.18) become

$$\frac{d}{dt}N_0(t) = -\frac{I(\nu,t)}{c}B_{10}[N_0(t) - N_1(t)] + \tau^{-1}N_1(t) = -\frac{d}{dt}N_1(t) \quad . \tag{2.21}$$

Note that N, N_0, and N_1 all refer to the densities of the absorbing gas which may only represent a small fraction of the total gas pressure, p_A. The total relaxation time, τ, will be proportional to p_A^{-1} if the cell contains a single absorbing gas or if it contains a small fraction of absorbing gas in a buffer gas.

We now represent each time-varying quantity by a dc component and an ac component sinusoidally varying at frequency ω; for example,

$$I(\nu,t) = \bar{I}(\nu) + \mathrm{Re}\left[\tilde{I}(\nu)\, e^{-i\omega t}\right] \quad . \tag{2.22}$$

Of course, light intensities and populations can never be negative, so $\tilde{I} \leq \bar{I}$, etc. With this notation, we may separate the dc and ac terms in (2.21). Using the fact that

$$\frac{d}{dt}\overline{N_0} = \frac{d}{dt}\overline{N_1} = 0 \quad , \tag{2.23}$$

and

$$\tilde{N}_0 = -\tilde{N}_1 \quad , \tag{2.24}$$

we find that

$$\overline{N_1} = \frac{NB_{10}\bar{I}(\nu)c^{-1}}{2B_{10}\bar{I}(\nu)c^{-1} + \tau^{-1}} \quad , \tag{2.25}$$

and

$$\tilde{N}_1 = \frac{NB_{10}\left[1 - \dfrac{2B_{10}\bar{I}(\nu)c^{-1}}{2B_{10}\bar{I}(\nu)c^{-1} + \tau^{-1}}\right]c^{-1}\tilde{I}(\nu)}{2B_{10}c^{-1}\left[\bar{I}(\nu) + \tilde{I}(\nu)\right] + \tau^{-1} - i\omega} \quad . \tag{2.26}$$

We see from (2.25) that the mean value of the upper level population, $\overline{N_1}$, is proportional to the mean input illumination, $\bar{I}$, for small values of $\bar{I}$; and that $\overline{N_1} \to N/2$ for very large values of $\bar{I}$. From (2.26), we see that the ac component of the upper level population, $\tilde{N}_1$, is independent of the modulation frequency, ω, if ω is small, but is proportional to ω^{-1} for large ω. Furthermore, $\tilde{N}_1 \to 0$ for large values of $\bar{I}$. If $\bar{I}$ is small, then $\tilde{N}_1 \propto \tilde{I}$. These results are summarized in Table 2.1.

TABLE 2.1. SUMMARY OF UPPER LEVEL POPULATION BEHAVIOR.

$\bar{I}(\nu)$	$\tilde{I}(\nu)$	ω	$\overline{N_1}$	$\tilde{N}_1$
-	-	small	-	independent of ω
-	-	large	-	$\propto \omega^{-1}$
small	-	-	$\tau N B_{10} c^{-1} \bar{I}(\nu)$	$\dfrac{NB_{10}c^{-1}\tilde{I}(\nu)}{\tau^{-1} - i\omega}$
large	-	-	$\to N/2$	$\to 0$

Having calculated the ac densities of both levels, we now wish to derive the ac component of the molecular translational energy per unit volume, ζ. Ignoring rotational energy, the total internal energy of the gas per unit volume is

$$\frac{U}{V_c} = \sum_j N_j U_j + \zeta \quad . \tag{2.27}$$

In our case, $U_0 = 0$ and $U_1 = h\nu$ so that

$$\frac{1}{V_c}U(t) = N_1(t)U_1 + \zeta(t) \quad . \tag{2.28}$$

Differentiating,

$$\frac{1}{V_c}\frac{d}{dt}U(t) = U_1\frac{d}{dt}N_1(t) + \frac{d}{dt}\zeta(t) \quad . \tag{2.29}$$

By conservation of energy, the change in internal energy is equal to the radiated energy absorbed minus the radiated energy emitted, and thus

$$\frac{1}{V_c}\frac{d}{dt}U(t) = \left[\frac{I(\nu,t)}{c}B_{01}N_0(t) - \left(\frac{I(\nu,t)}{c}B_{10} + A_{10}\right)N_1(t)\right]U_1 \quad . \tag{2.30}$$

Combining (2.29) and (2.30) and using (2.18), we find that

$$\frac{d}{dt}\zeta(t) = b_{10}U_1N_1(t) \quad . \tag{2.31}$$

For sinusoidal modulation,

$$-i\omega\tilde{\zeta} = b_{10}U_1\tilde{N}_1 \quad . \tag{2.32}$$

Inserting (2.26) into (2.32), we get the desired equation relating the rate of change of the molecular energy density to the input intensity:

$$-i\omega\tilde{\zeta} = \frac{b_{10}U_1NB_{10}\left[1 - \dfrac{2B_{10}\bar{I}(\nu)c^{-1}}{2B_{10}\bar{I}(\nu)c^{-1} + \tau^{-1}}\right]c^{-1}\tilde{I}(\nu)}{2B_{10}c^{-1}\left[\bar{I}(\nu) + \tilde{I}(\nu)\right] + \tau^{-1} - i\omega} \quad . \tag{2.33}$$

2.1.4 Generation of Pressure Signal

2.1.4.1 Normal Mode Amplitudes

We have just considered the modulation and absorption of the illuminating radiation, and the resultant variation in the translational energy density of the gas.

We must now treat the generation of the pressure signal which, through a microphone, produces the "final" electrical signal of the spectrophone.

The modulation of the translational energy of the gas will result in an acoustic pressure disturbance, $p(\vec{r},t)$, which is the difference between the total pressure and the ambient pressure p_A. Associated with the pressure disturbance are an acoustic velocity, $u_a(\vec{r},t)$, and an acoustic temperature. The acoustic velocity is related to the pressure through the relationship [6]

$$\tilde{u}_a(\vec{r}) = \frac{1}{i\omega\rho_0}\nabla\tilde{p}(\vec{r}) \quad , \tag{2.34}$$

where ρ_0 is the average gas density. If losses due to viscosity and thermal conduction are temporarily neglected, then the pressure disturbance can be described by [7]

$$\left[\nabla^2 + \frac{\omega^2}{u_s^2}\right]\tilde{p}(\vec{r}) = \left[\frac{\gamma-1}{u_s^2}\right]i\omega\tilde{H}(\vec{r}) \quad , \tag{2.35}$$

where u_s is the velocity of sound, $\gamma = \frac{C_p}{C_v}$, and $\tilde{H}$ is the rate of heat input to the gas given by

$$\tilde{H}(\vec{r}) = -i\omega\tilde{\zeta}(\vec{r}) \quad . \tag{2.36}$$

(The effect of losses will be introduced later in the model development). This inhomogeneous wave equation may be solved by expressing the solution, $\tilde{p}$, as an infinite series expansion of the normal mode solutions, p_j, of the homogeneous wave equation:

$$(\nabla^2 + k_j^2)p_j(\vec{r}) = 0 \quad , \tag{2.37}$$

where

$$k_j = \frac{\omega_j}{u_s} \quad . \tag{2.38}$$

Each normal mode p_j has a resonant frequency ω_j. The normal modes will be orthogonal and may be normalized so that

$$\frac{1}{V_c}\int p_i^* \, p_j \, dV = \delta_{ij} \quad , \tag{2.39}$$

where V_c is the volume of the gas cell. At this point we must become more specific about the geometry of the spectrophone cell. The cases of cylindrical and rectangular cell geometry will now be covered.

Cylindrical Spectrophone Geometry

If the spectrophone is a simple cylinder of radius r_c and length l_c, as shown in Figure 2.4a, then (2.37) can be written in cylindrical coordinates (r,ϑ,z) as

$$\frac{\partial^2}{\partial r^2}p_j + \frac{1}{r}\frac{\partial}{\partial r}p_j + \frac{1}{r^2}\frac{\partial^2}{\partial \vartheta^2}p_j + \frac{\partial^2}{\partial z^2}p_j + k_j^2 p_j = 0 \quad . \tag{2.40}$$

The solution [8] to this equation is

$$p_j(r,\vartheta,z) = \begin{bmatrix}\cos\\ \sin\end{bmatrix}(m\vartheta)\Big][AJ_m(k_r r) + BN_m(k_r r)][C\sin(k_z z) + D\cos(k_z z)] \quad , \tag{2.41}$$

where J_m and N_m are Bessel functions of the first and second kind, respectively, and

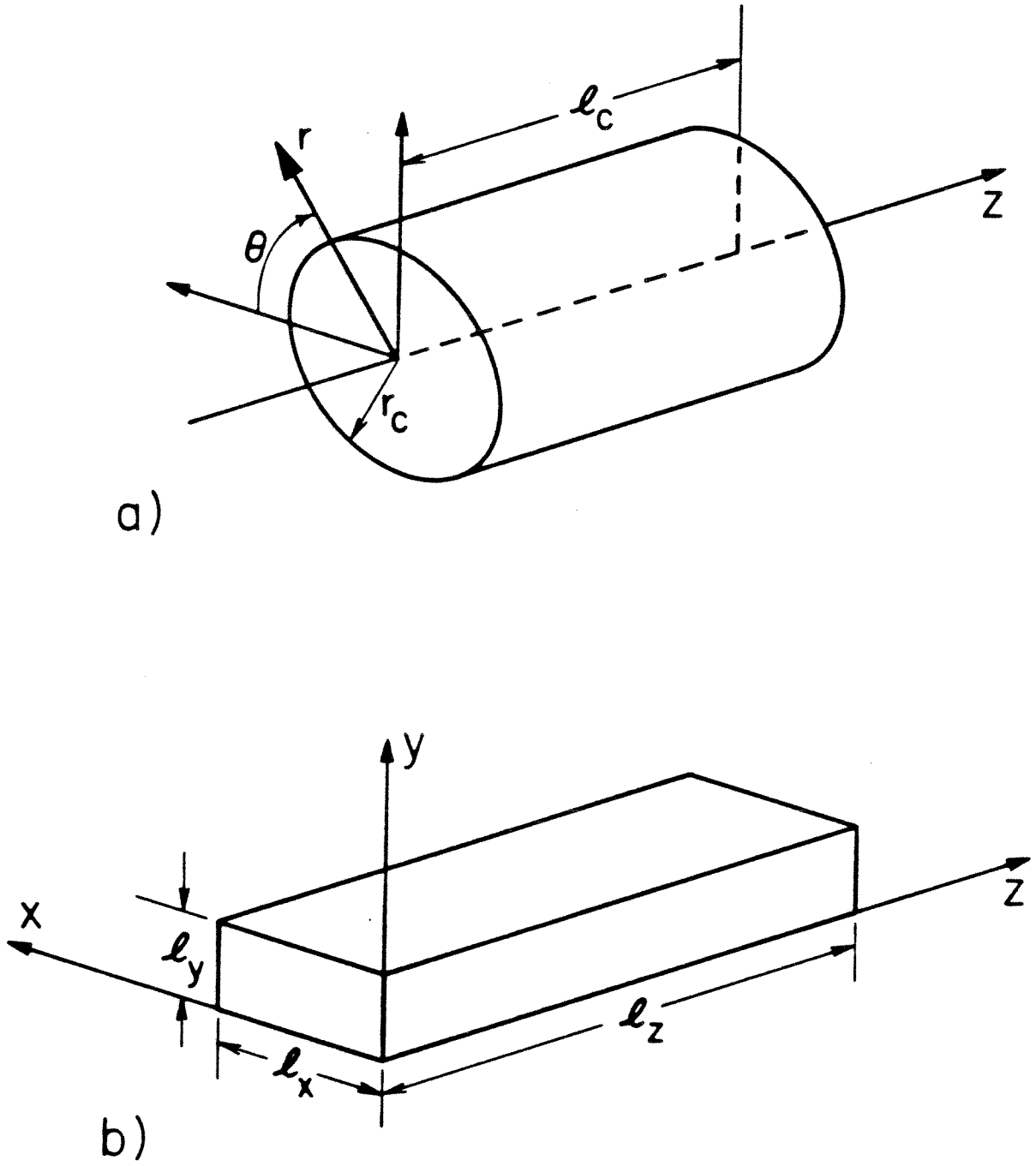

Figure 2.4. Examples of spectrophone cell geometry.
(a) cylindrical (b) rectangular.

$$k_j^2 = k_r^2 + k_z^2 \quad . \tag{2.42}$$

In order to satisfy the boundary conditions of a single-valued and finite pressure, we let m be an integer and B = 0, respectively. For rigid cell walls, the acoustic velocity normal to the walls must equal zero at both the end and side walls and thus, using (2.34), we find that C = 0,

$$k_z = \left(\frac{\pi}{l_c}\right) n_z \qquad n_z = 0, 1, 2, 3, \cdots \quad , \tag{2.43}$$

and

$$k_r = \left(\frac{\pi}{r_c}\right) \alpha_{mn} \quad , \tag{2.44}$$

where α_{mn} is the n^{th} root of the equation

$$J_{m+1}(\pi\alpha_{mn}) = \frac{m}{\pi\alpha_{mn}} J_m(\pi\alpha_{mn}) \quad . \tag{2.45}$$

Some values of α_{mn} [9] are given in Table 2.2.

TABLE 2.2. PARTIAL LIST OF ROOTS OF BESSEL FUNCTION EQUATION.

	α_{mn}			
	n = 0	n = 1	n = 2	n = 3
m = 0	0	1.2197	2.2331	3.2383
m = 1	0.5861	1.6970	2.7172	3.7261

Thus the normal mode solutions are given by

$$p_j(r,\vartheta,z) = \frac{2}{J_m(k_r r_c)\left[1-\left(\frac{m}{k_r r_c}\right)^2\right]^{\frac{1}{2}}} \begin{bmatrix}\cos\\ \sin\end{bmatrix}(m\vartheta) J_m(k_r r)\cos(k_z z) \quad . \tag{2.46}$$

Putting this expression into (2.40), we obtain for the resonant frequency ω_j

$$\omega_j = u_s\left(k_z^2+k_r^2\right)^{\frac{1}{2}} \quad . \tag{2.47}$$

As an example, consider a typical spectrophone [10] with l_c = 20 cm, r_c = 7.5 cm, and let u_s = 331 m/s. Table 2.3 lists the calculated resonant frequencies f_j for various values of m, n, and n_z.

TABLE 2.3. PARTIAL LIST OF CALCULATED RESONANT FREQUENCIES.

	f_j				
α_{mn}	n_z=0	n_z=1	n_z=2	n_z=3	n_z=4
α_{00}	0	827.5	1655	2483	3310
α_{10}	1293	1535	2100	2799	3554
α_{01}	2692	2816	3160	3662	4266

The lowest order pure longitudinal mode (m=0, n=0, n_z=1) has a resonant frequency of 828 Hz, while the lowest order pure radial mode (m=0, n=1, n_z=0) has a resonant frequency of 2692 Hz. The authors of Ref. [10] reported operating at a resonance frequency near 2750 Hz, which is very near the first order radial resonance. Some variance is expected since the speed of sound varies as $\sqrt{T}$ among other uncertainties.

Rectangular Spectrophone Geometry

A second possible spectrophone geometry is that of a rectangular parallelepiped, shown in Figure 2.4b, which is the geometry of the Stark spectrophone used in the experiments of this thesis. If l_x, l_y, and l_z are the lengths of the sides, then the normal mode solutions are given by

$$p_j(x, y, z) = 2\sqrt{2}\cos(k_x x)\cos(k_y y)\cos(k_z z) \quad , \tag{2.48}$$

where

$$k_x = \frac{\pi n_x}{l_x} \quad k_y = \frac{\pi n_y}{l_y} \quad k_z = \frac{\pi n_z}{l_z} \quad n_x, n_y, n_z = 0, 1, 2, \cdots \quad , \tag{2.49}$$

$$\omega_j = u_s(k_x^2 + k_y^2 + k_z^2)^{\frac{1}{2}} \quad , \tag{2.50}$$

and the coefficient in (2.48) is divided by $\sqrt{2}$ for each index that equals 0. The dimensions of our Stark spectrophone, which is described in a later chapter, were $l_x = 2 \times 10^{-3}$ m, $l_y = 1.07 \times 10^{-3}$ m, and $l_z = 2 \times 10^{-2}$ m; where z is the direction of light propagation through the spectrophone. We find that the lowest nonzero resonance frequency is 8275 Hz ($n_x = 0$, $n_y = 0$, $n_z = 1$).

An arbitrary acoustic pressure distribution can be expressed as a sum of the normal modes p_j:

$$\tilde{p}(\vec{r}, \omega) = \sum_j \tilde{A}_j(\omega) p_j(\vec{r}) \quad , \tag{2.51}$$

where $\tilde{A}_j$ is the amplitude of the j^{th} mode. Substituting this expression into (2.35), and using (2.37)-(2.39), yields for the mode amplitudes $\tilde{A}_j$,

$$\tilde{A}_j(\omega) = \frac{-i\omega}{\omega_j^2} \frac{(\gamma-1)\frac{1}{V_c}\int p_j^*(\vec{r})\,\tilde{H}(\vec{r})\,dV}{1 - \left(\frac{\omega}{\omega_j}\right)^2} \quad . \tag{2.52}$$

The numerator gives the coupling between the heat source and the normal mode p_j, while the denominator exhibits a resonance response which yields an infinite

amplitude as ω approaches ω_j. This physically unreasonable result is due to the neglect of losses in (2.35). We may include losses at this point by modifying (2.52) through the introduction of the normal mode quality factor, Q_j, to obtain

$$\tilde{A}_j(\omega) = \frac{-i\omega}{\omega_j^2} \frac{(\gamma-1)\frac{1}{V_c}\int p_j^*(\vec{r})\,\tilde{H}(\vec{r})\,dV}{1-\left(\frac{\omega}{\omega_j}\right)^2 - i\left(\frac{\omega}{\omega_j Q_j}\right)} \quad . \tag{2.53}$$

The physical origin of these losses will be described in section 2.1.4.2. The amplitude at resonance is now proportional to $\frac{Q_j}{\omega_j}$ and it decays as $\exp\left\{\frac{-\omega_j t}{2Q_j}\right\}$ if the excitation is removed. Also, $Q_j \approx \frac{\omega_j}{\Delta\omega_j}$, where $\Delta\omega_j$ is the FWHM of the resonance peak. In our example [10], the authors reported a Q of 200. For large values of Q, the tolerances on the modulation frequency become very strict.

The integral in (2.53) restricts the allowed normal pressure modes, depending on the spatial profile of $\tilde{H}(\vec{r})$. Inserting (2.46) into the volume integral of (2.53), we obtain for cylindrical geometry:

$$\tilde{A}_j(\omega) \propto \frac{1}{V_c}\int_0^{l_c}\int_0^{2\pi}\int_0^{r_c}\begin{bmatrix}\cos\\ \sin\end{bmatrix}(m\vartheta)\Big]J_m(k_r r)\cos(k_z z)\tilde{H}(r,\vartheta,z)\,r\,dr\,d\vartheta\,dz \quad . \tag{2.54}$$

If $\tilde{H}$ is independent of z, for example, for low losses in a gas, then $\tilde{A}_j = 0$ unless n_z, the number of planes of zero pressure occurring along the z-axis, is zero (if $n_z = 0$, then the coefficient in (2.46) is divided by 2). If $\tilde{H}$ is independent of ϑ, for example, a Gaussian laser beam centered on the z-axis, then $\tilde{A}_j = 0$ unless $m = 0$. If both of these conditions are true, and $\tilde{H}$ is a function of r only, then only radial modes (and resonances) can exist. For an on-axis laser beam with a Gaussian transverse dependence, (2.54) will increase as the beam diameter is decreased.

Similarly, for rectangular geometry, we see that a nonzero mode amplitude requires that $n_x = 0$, $n_y = 0$, or $n_z = 0$ if $\tilde{H}(x,y,z)$ is independent of x, y, or z, respectively. If there is very little absorption by the gas, the incident beam will be independent of z, and thus $n_z = 0$. In this case, the lowest order resonance of our Stark spectrophone will be the first horizontal resonance at 82.75 kHz ($n_x = 1$, $n_y = 0$, $n_z = 0$). Since the mode amplitude at ω_j is proportional to ω_j^{-1}, it is best to operate this spectrophone in a nonresonant configuration.

The simplest case occurs if $\tilde{H}$ is a constant, $\tilde{H}_0$ (i.e. uniform excitation throughout the cell), then $\tilde{A}_j = 0$ unless n_z, m, and n (or n_x, n_y, and n_z) all equal 0. The resultant mode p_0 is spatially uniform, has a resonant frequency $\omega_0 = 0$, and has an amplitude given by

$$\tilde{A}_0(\omega) = \frac{i(\gamma-1)\tilde{H}_0}{\omega\left[1+\frac{i}{\omega t_c}\right]} \quad , \tag{2.55}$$

where t_c is the damping time of p_0 due to heat conduction from the gas to the walls of the cell. If the absorption of the radiation is small enough so that the absorbing transition is not saturated, and if its time modulation is slow compared to the molecular processes, then we may combine (2.33) and (2.36) to write

$$\tilde{H}_0 = \tau b_{10} U_1 N B_{10} c^{-1} \tilde{I}(\nu) = \alpha \tilde{I} = \frac{\alpha l_c \tilde{W}}{V_c} \quad , \tag{2.56}$$

where $\tilde{I}$ and $\tilde{W}$ are the laser's intensity and power, respectively, and where uniform illumination is still assumed. Inserting (2.56) into (2.55), we obtain

$$\tilde{A}_0(\omega) = \frac{i(\gamma-1)\alpha l_c \tilde{W}}{\omega\left[1+\frac{i}{\omega t_c}\right]V_c} \quad . \tag{2.57}$$

The amplitude of the lowest-order mode is proportional to the power absorbed by the gas, $\alpha l_c \tilde{W}$, and is inversely proportional to the cell volume V_c. If the illumination does not uniformly fill the entire cell, other acoustic modes will also be excited, but equation (2.57) is still valid since the uniform pressure mode amplitude is derived from the average of the excitation over the cell volume. If we arrange the incident light to excite only some other mode j, then the amplitude of that mode is given by

$$\tilde{A}_j(\omega) = \frac{-i\omega}{\omega_j^2} \frac{(\gamma-1)\alpha l_c \tilde{W}}{\left\{1-\left[\frac{\omega}{\omega_j}\right]^2 - i\left[\frac{\omega}{\omega_j Q_j}\right]\right\}V_c} \quad . \tag{2.58}$$

This may not always be experimentally possible and so (2.58) represents an upper limit for the mode amplitude. At low frequencies ($\omega << \omega_j$ and $\omega << \omega_j^2 t_c$), it is clear that $\tilde{A}_0(\omega) > \tilde{A}_j(\omega)$, while at higher frequencies, $\tilde{A}_0(\omega) \propto \frac{1}{\omega}$ and $\tilde{A}_j(\omega)$ peaks at $\omega = \omega_j$. The ratio of the zero and j^{th} resonance amplitudes is

$$\tilde{A}_j(\omega_j) \,/\, \tilde{A}_0(0) = \frac{Q_j}{\omega_j t_c} \quad . \tag{2.59}$$

Resonance operation at frequency ω_j is more attractive than low-frequency operation only for large values of this ratio. (Of course, there are other considerations such as the background signal, noise, and experimental complexity). Since $\tilde{A}_j(\omega_j) \propto \omega_j^{-1}$, and since the resonant frequencies are proportional to the inverse of the cell's dimensions, we see that small cells will have high resonant frequencies and should probably be operated in a nonresonant configuration. If the cell's dimen-

sions are increased in order to reduce ω_j, then a penalty in sensitivity is paid due to the increased cell volume. This may be desirable [10] if a large volume-to-surface area ratio is desired. Also, the Q of a cavity will be decreased by geometrical perturbations such as the microphone, gas fill ports, or acoustic baffles designed to reduce the background signal.

2.1.4.2 The Quality Factor Q

In (2.53), we introduced a finite quality factor Q for each mode in order to correct the physically unreasonable condition of no acoustic losses. This finite Q is the result of loss caused by heat conduction, viscosity, and other effects. We will consider here the separable surface and volume losses due to heat conduction and viscosity in a homogeneous fluid at rest. The surface losses occur in two regions which extend out from the cell walls. Viscosity effects take place in a region of thickness l_v and heat conduction effects take place in a region of thickness l_h. These depths are given by [6,7]

$$l_v = \left(\frac{2\eta}{\omega\rho_0}\right)^{\frac{1}{2}} \quad , \quad \text{and} \quad l_h = \left(\frac{2k}{\omega\rho_0 C_p}\right)^{\frac{1}{2}} \quad , \tag{2.60}$$

where η is the dynamic viscosity, k the thermal conductivity, and C_p the specific heat at constant pressure of the gas. For air at STP, l_h is slightly larger than l_v.

The thermal damping time t_c can be estimated by equating it to the reciprocal of the frequency at which l_h in (2.60) is equal to the cell radius r_c:

$$t_c \approx \frac{\pi\rho_0 C_p r_c^2}{k} \quad . \tag{2.61}$$

For our example cylindrical spectrophone [10] at STP, $t_c \approx$ 859 seconds. The thermal damping time for the rectangular Stark spectrophone can be approximated by

substituting $l_y/2$ (the smallest dimension) for r_c in (2.61). The result is $t_c \approx 4.45 \times 10^{-2}$ seconds which corresponds to 22.5 Hz. Note that the thermal time constant is proportional to the ambient pressure.

The two surface losses are due to the boundary effects imposed by the cell walls. While the acoustic expansion and contraction of the gas far from the walls is nearly adiabatic, it is isothermal near the walls due to their large thermal conductivity compared to the gas. Surface losses due to heat conduction occur in the region of transition between these two behaviors. Similarly, at the wall, the tangential acoustic velocity, u_{atj}, is zero due to viscosity, while far from the walls, it is given by (2.34). Again, surface loss due to viscosity occurs in the transition region.

The total surface loss is given by [7]

$$L_{sj} = |\tilde{A}_j(\omega)|^2 \int \left(\frac{1}{2} R_v |u_{atj}|^2 + \frac{1}{2} R_h |p_j|^2 \right) dS \quad , \tag{2.62}$$

where

$$R_v = \frac{\rho_0 \omega}{2} l_v = \left(\frac{\eta \omega \rho_0}{2} \right)^{\frac{1}{2}} \quad , \tag{2.63}$$

and

$$R_h = \frac{(\gamma - 1)\omega}{2\rho_0 u_s^2} l_h = \frac{\gamma - 1}{\rho_0 u_s^2} \left(\frac{k\omega}{2\rho_0 C_p} \right)^{\frac{1}{2}} \quad , \tag{2.64}$$

are the viscous surface resistance and heat conduction surface resistance, respectively. In (2.62), u_{atj} is the acoustic velocity for the j^{th} mode tangential to the walls that would be present with no viscosity or heat conduction, and the integration is over the surfaces of the cell which should have large radii of curvature compared to

l_v and l_h. The volume loss is due to energy transferred from the acoustic wave to thermal energy through heat conduction and viscosity, which acts as a frictional force. It is given by [6]

$$L_{vj} = |\tilde{A}_j(\omega)|^2 V_c \left[\frac{\omega_j}{\rho_0 u_s^2}\right]^2 \left[(\gamma - 1)\frac{k}{2C_p} + \frac{2\eta}{3}\right] \quad . \tag{2.65}$$

The acoustic energy stored in mode j is given by [11,12]

$$U_j = \frac{V_c |\tilde{A}_j(\omega)|^2}{\rho_0 u_s^2} \quad . \tag{2.66}$$

We may use (2.62), (2.65), and (2.66) to express Q_j as

$$Q_j = \omega_j \frac{\text{energy stored in mode j}}{\text{rate of energy loss of mode j}} = \omega_j \frac{U_j}{L_{sj} + L_{vj}} \quad . \tag{2.67}$$

2.1.4.3 Thermal Fluctuation Noise

The thermal fluctuations (Brownian motion) of the gas within the spectrophone will also excite each acoustic pressure mode. Each mode has an average energy of k_BT ($\hbar\omega_j << k_BT$) and, hence, a noise amplitude given by [13]

$$|A_{nj}(\omega)|^2 = \frac{4\rho_0 u_s^2 k_B T}{V_c \omega_j Q_j \left[\left(1 - \frac{\omega^2}{\omega_j^2}\right)^2 + \left(\frac{\omega}{\omega_j Q_j}\right)^2\right]} \quad [Pa^2\text{–}Hz^{-1}] \quad . \tag{2.68}$$

As Q_j is increased, the noise energy will be concentrated closer to the resonant frequencies ω_j. The zero-order mode has no fluctuation noise ($A_{n0} = 0$), as can be seen from (2.68) by taking the limit $\omega_j \to 0$. However, noise from other modes will interfere with the measurement of the zero-order mode amplitude. Since $\rho_0 u_s^2 = \gamma p_A$, the noise amplitude is proportional to $p_A^{\frac{1}{2}}$. For operation at low frequencies ($\omega << \omega_j$),

(2.68) becomes

$$|A_{nj}(\omega)|^2 = \frac{4\rho_0 u_s^2 k_B T}{V_c \omega_j Q_j} \quad . \tag{2.69}$$

Thus the noise contributed by mode j may be reduced by increasing Q_j.

As an example of the noise equivalent power (NEP) of a spectrophone, consider zero-order signal detection with $\omega t_c >> 1$ such that (2.57) becomes

$$\tilde{A}_0(\omega) = \frac{i(\gamma - 1)\alpha\, l_c \tilde{W}}{\omega V_c} \quad . \tag{2.70}$$

The absorbed power is given by $\alpha\, l_c \tilde{W}$. If the interfering noise is primarily from the first mode, then (2.69) applies with j = 1. Equating the right-hand side of (2.69) with the squared magnitude of (2.70), we find

$$\frac{(NEP)^2}{\Delta f} = \frac{\left[\alpha\, l_c |\tilde{W}|\right]^2}{\Delta f} = \frac{8\pi\rho_0 u_s^2 k_B T V_c \omega^2}{\omega_1 Q_1 (\gamma - 1)^2} \quad \left[\frac{W^2}{Hz}\right] \quad . \tag{2.71}$$

This theoretical value of NEP gives an estimation of the minimum detectable absorbed power. An actual spectrophone will have an NEP greater than that given by (2.71). Kreuzer [14] has calculated an NEP $\times (\Delta f)^{-\frac{1}{2}}$ of 3.6×10^{-11} W $Hz^{-\frac{1}{2}}$ for an optimized spectrophone limited by thermal fluctuations in the gas.

As an example, consider the case of our Stark spectrophone: $V_c = 1.36 \times 10^{-7}$ m^3 and $\omega_1 = 2\pi \times 8275$, and let f = 13 Hz, p_A = 50 torr, and T = 300 K. Inserting these values into (2.71), we obtain

$$NEP \times (\Delta f)^{-\frac{1}{2}} = \frac{1}{\sqrt{Q_1}} \times 10^{-11} \text{ W Hz}^{-\frac{1}{2}} \quad . \tag{2.72}$$

2.1.5 Signal Detection: The Microphone

The fourth step in the generation of the optoacoustic signal is the conversion of the acoustic pressure signal into an electrical signal with a sensitive microphone. (Other proposed methods of detection include direct detection of gas temperature fluctuation [15] and detection of gas density (index of refraction) fluctuation [16].) Microphones are either pressure operated, pressure-gradient operated, phase-shift operated, or a combination of these [17]. Pressure microphones consist principally of electromagnetic, electrostatic, and piezoelectric types [12]. The predominant type of microphone used for optoacoustic detection has been the capacitive, or condenser, microphone which is an electrostatic pressure-operated microphone. Condenser microphones feature high sensitivity and stability, a flat, wide frequency response, low noise, and a minimum effect on the surrounding sound field.

There are three basic techniques of biasing a condenser microphone:

(1) A constant charge is applied to the diaphragm and a voltage signal is detected by a high impedance amplifier;

(2) A constant voltage is applied and a current signal detected by a low impedance current amplifier;

(3) An alternating current is applied such that diaphragm motion either frequency-modulates a carrier or unbalances a bridge circuit.

Another type of microphone, the electret microphone [18], has recently become popular for optoacoustic detection [19] because of its small size and because biasing is not needed.

All the spectrophone work reported in this thesis employed condenser microphones and the constant-charge biasing technique. Therefore, only this method will be examined further.

A condenser microphone is basically an air dielectric capacitor formed by a rigid backplate and a thin metal diaphragm mounted under a large radial tension as shown in Figure 2.5. Acoustic pressure acting on one side of the diaphragm causes it to move, which alters the electrical capacitance between the diaphragm and backplate. Motion of the diaphragm may be described by the modes of vibration of a thin plate supported at its perimeter [8,14,20]. These modes may be described by the number of diametrical and circular nodal lines on the diaphragm. Only the lowest order mode (no nodal lines) will cause a significant change in capacitance, so it is only necessary to consider this mode. The lowest order mode causes the diaphragm to bend into a spherical shape which may be described by a single degree of freedom. If the diaphragm lies in the yz plane centered at the origin, then each point of the diaphragm is displaced in the x direction by

$$x(r) = x(0)\left[1 - \frac{r^2}{r_d^2}\right] \quad , \tag{2.73}$$

where r is the radial coordinate, x(0) is the displacement at the center, and r_d is the diaphragm radius. The average displacement of the diaphragm is given by

$$x = \langle x(r) \rangle = \frac{1}{\pi r_d^2} \int_0^{2\pi} \int_0^{r_d} x(r) r dr d\vartheta = \frac{x(0)}{2} \quad . \tag{2.74}$$

The average motion is one-half the motion at the center. The equation of motion in the average coordinate x for the lowest-order mode is [8]

$$\frac{4M}{3} \frac{d^2x}{dt^2} + \delta \frac{dx}{dt} + \left[8\pi Y + \frac{(\pi r_d^2)^2 \gamma p_A}{V_e}\right] x = F \quad , \tag{2.75}$$

where M is the mass of the diaphragm, δ the damping coefficient, Y the mechanical

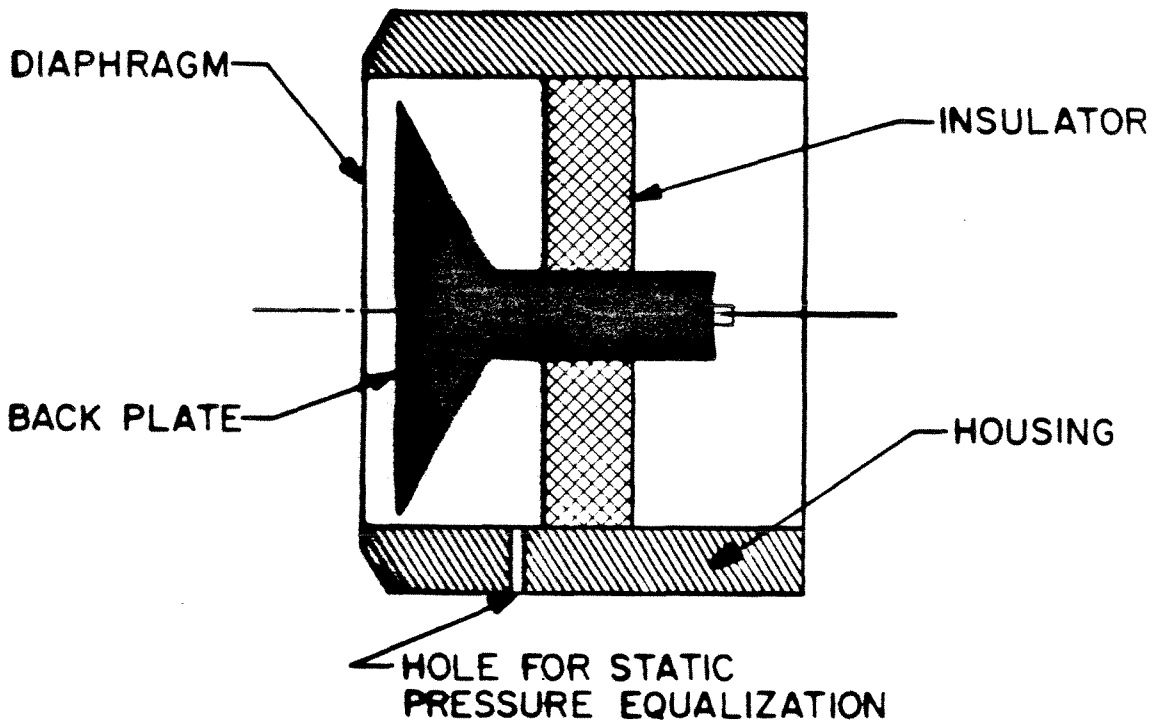

Figure 2.5. Schematic construction of a condenser microphone.

tension, and F the externally applied force. The factors 4/3 and 8π result from the nonuniform membrane motion and the averaging process. The second term in the brackets results from considering the compression of the gas in the spectrophone volume , V_c, and in the volume enclosed behind the diaphragm of the microphone, V_m. The equivalent volume, V_e, is defined as

$$\frac{1}{V_e} = \frac{1}{V_c} + \frac{1}{V_m} \quad . \tag{2.76}$$

The volumes are measured with the diaphragm in its biased equilibrium position. We have assumed that the acoustic pressure varies fast enough for adiabatic conditions to hold and that the ambient pressure varies slowly so that the pressure on both sides of the diaphragm is equal. The tension, Y, must be sufficient to prevent the diaphragm from contacting the backplate. The external force F' consists of two parts:

(1) The force resulting from the applied bias voltage, v_b; a dc force which shifts the equilibrium position of the diaphragm;

(2) The force due to the acoustic pressure, $< p > \pi r_d^2$, where $< p >$ is the average of the pressure over the diaphragm; an ac force.

The constant-charge biasing method is achieved by connecting the microphone to a bias voltage v_b through a large resistor R_b, which is sufficiently large that $(R_b C_b)^{-1}$ is much less than the signal frequencies of interest. C_b is the biased microphone capacitance given by

$$C_b = \frac{\varepsilon_0 A_{eff}}{x_b} \quad , \tag{2.77}$$

where x_b is the biased diaphragm to backplate spacing and A_{eff} is the effective capa-

citor area given the different diaphragm and backplate geometries. Assuming small perturbations from equilibrium and a high input-impedance amplifier, we may use (2.75) to write for the microphone output voltage

$$\tilde{v}_m = -\frac{v_b}{x_b}\tilde{x} = -\frac{v_b}{x_b}\frac{\tilde{F}}{8\pi Y_e - i\omega\delta - \omega^2\frac{4M}{3}}$$

$$= -\frac{v_b r_d^2}{x_b 8Y_e}\frac{1}{1 - \frac{\omega^2}{\omega_m^2} - i\frac{\omega}{\omega_m Q_m}}\tilde{p} \quad , \tag{2.78}$$

with

$$Y_e = Y + \frac{(\pi r_d^2)^2 \gamma p_A}{8\pi V_e} \quad , \tag{2.79}$$

where $\tilde{F} = \pi r_d^2 \tilde{p}$ is the only ac force acting on the diaphragm, and where ω_m and Q_m are the microphone resonant frequency and quality factor, respectively, given by

$$\omega_m = \left(\frac{6\pi Y_e}{M}\right)^{\frac{1}{2}} \quad \text{and} \quad Q_m = \frac{4}{\delta}\left(\frac{2\pi Y_e M}{3}\right)^{\frac{1}{2}} \quad . \tag{2.80}$$

The enclosed volumes, V_c and V_m, reduce the microphone voltage and increase the resonant frequency and quality factor. The open-circuit voltage sensitivity S_{oc} is defined as the low-frequency ratio of the output voltage to the acoustic pressure:

$$S_{oc} = \frac{-v_b r_d^2}{x_b 8Y_e} \quad . \tag{2.81}$$

The presence of the microphone inside the spectrophone will affect the acoustic modes p_j by changing the boundary conditions of the acoustic velocity [14]. However, if the spectrophone cell is small enough and if the modulation frequency is less

than both the cell's first resonant frequency and the microphone resonance, then the pressure within the cell will be independent of position and the microphone will behave like an additional volume V_m added to the cell. Combining (2.57) and (2.81), we obtain

$$\tilde{v}_m = S_{oc}\tilde{p} = \frac{-v_b r_d^2}{8x_b\left[Y + \frac{(\pi r_d^2)^2 \gamma p_A (V_c + V_m)}{8\pi V_c V_m}\right]} \frac{i(\gamma-1)(\alpha l_c \tilde{W})}{\omega\left(1 + \frac{i}{\omega t_c}\right)V_c} \quad . \tag{2.82}$$

This equation shows the influence of the microphone's volume and other parameters on the output voltage. The presence of the microphone reduces the pressure. The maximum signal is attained by reducing both V_c and V_m and when $V_c << V_m$. If the mechanical tension Y is neglected in (2.82), then the voltage dependence on V_c and V_m becomes $V_m (V_c + V_m)^{-1}$. This dependence is equivalent to the result of other authors [5,14] who neglect the microphone volume entirely in deriving S_{oc}: $V_m \to 0$ in (2.81), but instead add V_m to V_c in the expression for $\tilde{p}$: $V_c \to V_c + V_m$ in (2.57). Later, we will show that our experimental results exhibited a pressure and frequency dependence that required all the terms of (2.82) for explanation; thus the earlier theory was inadequate.

If the losses come only from the microphone damping, then the low frequency noise voltage $|v_n(\omega)|^2$ due to the Brownian motion of the gas is calculated by using (2.69) to obtain

$$|v_n(\omega)|^2 = |A_{nj}(\omega)|^2 S_{oc}{}^2 = \frac{4k_B T \rho_0 u_s^2}{\omega_m Q_m (V_c + V_m)} S_{oc}{}^2 \quad [V^2\text{–Hz}^{-1}] \quad . \tag{2.83}$$

This noise voltage represents the ultimate limit to the sensitivity of optoacoustic detection.

The power signal-to-noise ratio is given by

$$\left(\frac{S}{n}\right)^2 = \frac{|\tilde{v}_m(\omega)|^2}{|v_n(\omega)|^2 \Delta f} = \frac{(\gamma-1)^2}{\gamma}\left(\frac{l_c}{V_c}\right)^2 \frac{(V_c+V_m)}{V_c^2} \frac{2\pi Y_e \alpha^2 |\tilde{W}|^2}{\omega^2\left(1+\frac{1}{\omega^2 t_c^2}\right)\delta k_B T p_A \Delta f} \quad . \quad (2.84)$$

The factor $(\gamma-1)^2\gamma^{-1}$ may be increased by using a monatomic buffer gas such as helium or argon. For nonresonant cells, the factor $l_c^2 V_c^{-2}$ suggests that the cell cross-sectional area should be as small as possible and only slightly larger than the cross-section of the laser beam. Also, the factor $(V_c + V_m)V_c^{-2}$ indicates that the cell volume V_c should be as small as possible. The factor $k_B T p_A$ suggests operating at a low gas temperature and pressure. A narrow detection bandwidth, Δf, is desirable. For large modulation frequencies ($\omega t_c >> 1$), $\left(\frac{S}{n}\right) \propto \omega^{-1}$, and increases as the frequency is lowered. When $\omega t_c << 1$, (e.g. small modulation frequency, ambient pressure, and cell dimensions), $\left(\frac{S}{n}\right)$ is independent of the modulation frequency. Of course, we have assumed that $\omega R_b C_b >> 1$, and have ignored the fact that the electronics will typically exhibit f^{-1} noise. Other sources of noise include amplifier noise and the Johnson noise of the bias resistor R_b [14], but these are independent of frequency. The pressure dependence of $\left(\frac{S}{n}\right)$, in addition to the dependence of $\alpha(\nu)$, enters through the p_A^{-1} term and through the parameters t_c and Y_e as can be seen from (2.61) and (2.79). The pressure dependence of $\left(\frac{S}{n}\right)$ can vary from $p_A^{-\frac{1}{2}}$ to p_A^{1} depending on the relative size of these parameters.

2.2 The Background Signal

2.2.1 Introduction

The background signal in optoacoustic detection is the synchronous signal observed when the absorbing gas mixture in the cell is replaced with a similar nonabsorbing gas. In principle, the optoacoustic signal arises only from the absorption of the illuminating radiation by the gas sample. Therefore, a nonabsorbing gas should produce no signal. However, in practice, all optoacoustic detector configurations exhibit a background signal. As stated earlier, much work has been done, including the present study, in an attempt to reduce the background signal of spectrophones in order to improve their detectability and accuracy. The background signal limits the detectability and accuracy in the following ways:

(1) It must be subtracted from the signal+background data, introducing the inherent inaccuracy associated with the subtraction of two almost equal numbers;

(2) It is difficult to maintain the exact experimental conditions, minus the absorbing gas, in order to measure the background signal;

(3) It may contribute to saturation of the signal processing electronics and, therefore, force an unwanted reduction in the laser power.

The sources of the background signal in a conventional spectrophone include:

(1) Window bulk absorption;

(2) Window surface absorption: molecules adsorbed on the window surface may absorb the illuminating radiation;

(3) Off-axis radiation within the cell: light scattered by the windows, the optics, or the edge of the chopper blade may strike the inside walls of the spectrophone and be absorbed;

(4) Light scattering or absorption due to microaerosols in the gas;

(5) Acoustic or vibrational pickup from the mechanical light chopper;

(6) Small amounts of absorbing contamination which may outgas from the cell materials, seals, etc.

Just as noise is added to the desired signal at each stage in the signal generation process (see Figure 1.3), sources of background signal may also be added at each stage. The absorption of radiation by the windows and walls would be classified in the second or "absorption of radiation" stage. Acoustic pickup from the chopper is considered in the third or "excitation of sound" stage. Often, wavelength modulation of the laser is used instead of the chopper. However, if the laser power also exhibits a slight modulation, or if the window absorption depends on the wavelength, these effects would result in a background signal contribution in the first or second stage, respectively. Finally, the modulated electric field used in the Stark spectrophone can result in pickup by the microphone or preamplifier and thus cause a background signal associated with the fourth or fifth stage of signal generation. We will now develop some simple theoretical expressions to explain these effects.

2.2.2 Theory

Although very little theoretical work has been done on the components of the background signal in a spectrophone, it is possible to gain physical insight into this important phenomenon through an adaptation of the one-dimensional photoacoustic theory. This theory of the signal generation for a solid (condensed) absorbing sample has been primarily developed by Rosencwaig and Gersho [21-26]. The development of the RG theory will first be outlined and then three special cases will be discussed which correspond to the bulk and surface absorption components of the window signal, and to the component due to scattered light.

The RG theory for optoacoustic detection of absorption in solids proceeds as follows. It assumes a one-dimensional cell containing a nonabsorbing gas of length l_g, an absorbing solid sample of length l_s, and a nonabsorbing backing material of length l_b as shown in Figure 2.6. Intensity modulated radiation enters the cell and is absorbed by the sample. This deposition of energy causes thermal waves in the backing, sample, and gas. The thermal diffusion equation is solved with appropriate boundary conditions in the three regions. In particular, the ac temperature in the gas is derived and is found to decrease very rapidly with distance from the solid-gas interface (x=0). It is assumed that only the gas in a small region near the solid-gas interface is affected directly by the oscillatory temperature, and that this gas column expands and contracts like a piston, driving the remainder of the gas column, and causing a pressure signal. A microphone (not shown) detects the pressure in the gas.

We define the parameters

(1) ρ: density

(2) C_p: specific heat at constant pressure

(3) k: thermal conductivity

(4) $\beta = \frac{k}{\rho C_p}$: thermal diffusivity

(5) $a = \left(\frac{\omega}{2\beta}\right)^{\frac{1}{2}}$: thermal diffusion coefficient

where each parameter may have the subscript s, g, or b for the solid, gas, or backing material, respectively, and where ω is the modulation frequency of the incident monochromatic light source whose intensity is given by

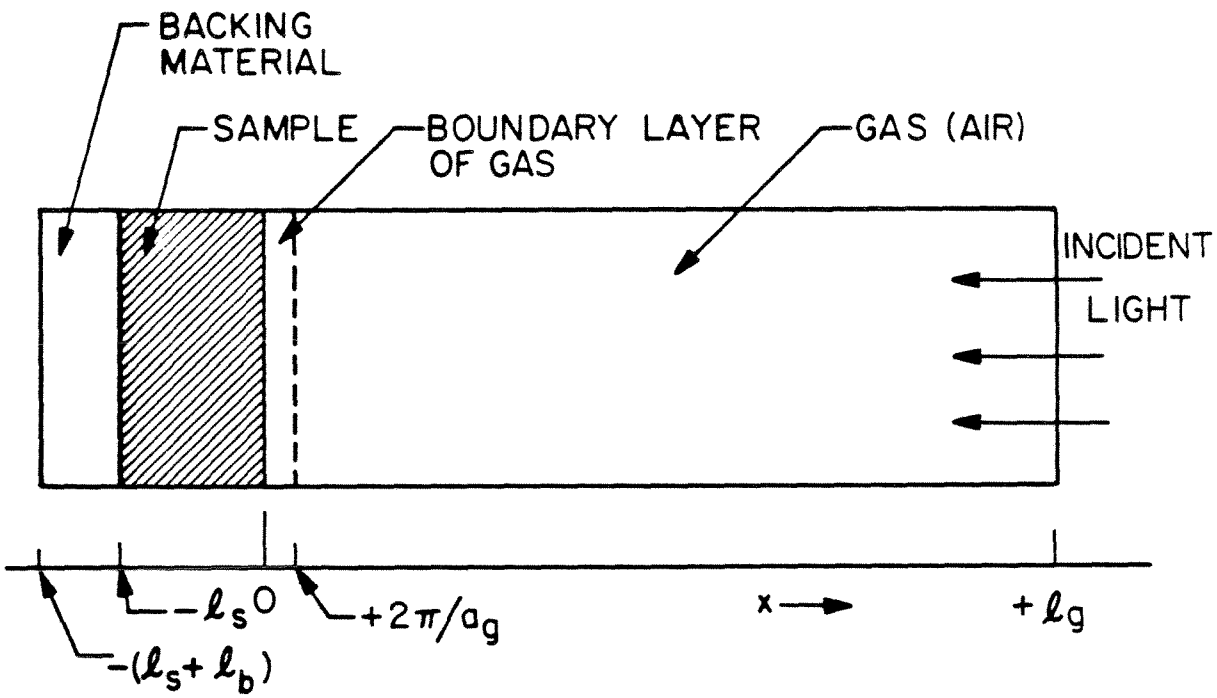

Figure 2.6. One-dimensional photoacoustic geometry showing the nonabsorbing gas, the absorbing sample material and the nonabsorbing backing material.

$$I(t) = \frac{I}{2}(1 + \cos\omega t) \quad . \tag{2.84}$$

Table 2.4 lists the above photoacoustic parameters for some commonly encountered substances. If α is the linear attenuation coefficient of the sample at wavelength λ, then the rate of heat input to the sample is

$$H(x, t) = \kappa\alpha e^{\alpha x} \frac{I}{2}(1 + \cos\omega t) \quad \left[\frac{W}{m^3}\right] \quad , \tag{2.85}$$

where κ is the efficiency by which absorbed light in the solid is converted into heat by nonradiative deexcitation processes. Letting T(x,t) be the temperature relative to the ambient temperature T_0, the three thermal diffusion equations are

$$\frac{\partial^2}{\partial x^2} T_b(x, t) = \frac{1}{\beta_b} \frac{\partial}{\partial t} T_b(x, t) \quad -l_s - l_b \leq x \leq -l_s \quad , \tag{2.86}$$

$$\frac{\partial^2}{\partial x^2} T_s(x, t) = \frac{1}{\beta_s} \frac{\partial}{\partial t} T_s(x, t) - \frac{\kappa\alpha e^{\alpha x} I}{2k_s}(1 + \cos\omega t) \quad -l_s \leq x \leq 0 \quad , \tag{2.87}$$

and

$$\frac{\partial^2}{\partial x^2} T_g(x, t) = \frac{1}{\beta_g} \frac{\partial}{\partial t} T_g(x, t) \quad 0 \leq x \leq l_g \quad . \tag{2.88}$$

If the relative temperature T is expressed as a sum of dc and time-varying components,

$$T(x, t) = \bar{T}(x) + Re[\tilde{T}(x)\ e^{-i\omega t}] \quad , \tag{2.89}$$

then equations (2.86)-(2.88) yield

TABLE 2.4. PARAMETER VALUES OF SOME COMMON SUBSTANCES.

Substance	Density	Specific Heat	Thermal Conductivity	Thermal Diffusivity	Thermal Diffusion Coefficient At 100 Hz
	ρ	C_p	k	$\beta = \frac{k}{\rho C_p}$	$a = \left(\frac{\omega}{2\beta}\right)^{\frac{1}{2}}$
	$\frac{kg}{m^3}$	$\frac{J}{kg-K}$	$\frac{J}{s-m-K}$	$\frac{m^2}{s}$	$\frac{1}{m}$
Air (STP)	1.23	1.00×10^3	2.53×10^{-2}	2.07×10^{-5}	3.90×10^3
Aluminum	2.70×10^3	9.04×10^2	2.01×10^2	8.24×10^{-5}	1.95×10^3
Germanium	5.35×10^3	3.14×10^2	5.9×10^1	3.51×10^{-5}	2.99×10^3
Stainless Steel	7.50×10^3	5.02×10^2	1.38×10^1	3.67×10^{-6}	9.26×10^3
Zinc Selenide	5.27×10^3	3.55×10^2	1.8×10^1	9.62×10^{-6}	5.71×10^3

	Thermal Diffusion Length At 100 Hz		Linear Attenuation Coefficient At 10.6 μm	Index of Refraction At 10.6 μm
	$\frac{1}{a}$	ka	α	n
	m	$\frac{J}{s-m^2-K}$	$\frac{1}{m}$	
Air (STP)	2.56×10^{-4}	9.87×10^1		
Aluminum	5.12×10^{-4}	3.93×10^5	7.2×10^7	17.4
Germanium	3.34×10^{-4}	1.76×10^5	3.2	4.0
Stainless Steel	1.08×10^{-4}	1.28×10^5		
Zinc Selenide	1.75×10^{-4}	1.03×10^5	0.2	2.40

$$\frac{\partial^2}{\partial x^2}\overline{T_b}(x) = 0 \quad , \quad \frac{\partial^2}{\partial x^2}\overline{T_s}(x) = \frac{-\kappa\alpha e^{\alpha x} I}{2k_s} \quad , \quad \frac{\partial^2}{\partial x^2}\overline{T_g}(x) = 0 \quad , \tag{2.90}$$

$$\frac{\partial^2}{\partial x^2}\tilde{T}_b(x) = \frac{-i\omega}{\beta_b}\tilde{T}_b(x) \quad , \tag{2.91}$$

$$\frac{\partial^2}{\partial x^2}\tilde{T}_s(x) = \frac{-i\omega}{\beta_s}\tilde{T}_s(x) - \frac{\kappa\alpha e^{\alpha x}\tilde{I}}{2k_s} \quad , \tag{2.92}$$

and

$$\frac{\partial^2}{\partial x^2}\tilde{T}_g(x) = \frac{-i\omega}{\beta_g}\tilde{T}_g(x) \quad . \tag{2.93}$$

Requiring that T = 0 at the end faces of the cell, $x = l_g$ and $x = -l_s - l_b$, the general solution for T can be written

$$\overline{T_b}(x) = \frac{\overline{T_b}}{l_b}(x + l_s + l_b) \quad , \quad \tilde{T}_b(x) = \tilde{T}_b e^{\xi_b(x + l_s)} \quad , \quad -l_s - l_b \le x \le -l_s \quad ; \tag{2.94}$$

$$\overline{T_s}(x) = \overline{T_{s1}} + \overline{T_{s2}}\, x + \overline{T_{s3}}\, e^{\alpha x} \quad ,$$

$$\tilde{T}_s(x) = \tilde{T}_{s1}\, e^{\xi_s x} + \tilde{T}_{s2}\, e^{-\xi_s x} - \tilde{T}_{s3}\, e^{\alpha x} \quad , \quad -l_s \le x \le 0 \quad ; \tag{2.95}$$

and

$$\overline{T_g}(x) = \overline{T_g}\left(1 - \frac{x}{l_g}\right) \quad , \quad \tilde{T}_g(x) = \tilde{T}_g e^{-\xi_g x} \quad , \quad 0 \le x \le l_g \quad ; \tag{2.96}$$

where

$$\overline{T_{s3}} = \frac{-\kappa I}{2\alpha k_s} \quad , \tag{2.97}$$

$$\tilde{T}_{s3} = \frac{\alpha\kappa \tilde{I}}{2k_s(\alpha^2 - \xi_s^2)} \quad , \tag{2.98}$$

and

$$\xi_j = (1 - i)a_j \quad . \tag{2.99}$$

Note that the sample has thermal waves traveling in both directions, while the backing and gas only have waves traveling away from the sample. The inward traveling waves in the gas and backing regions were eliminated, because the outward traveling waves (with damped exponentials in x) were assumed zero at the end faces by letting the thermal diffusion length be much smaller than the physical length of each region: $a_b^{-1} << l_b$ and $a_g^{-1} << l_g$. This is reasonable since $a_g^{-1} \approx 0.03$ cm in air at 100 Hz and 0.07 cm at 13 Hz.

The remaining unknown complex constants: $\tilde{T}_b$, $\tilde{T}_{s1}$, $\tilde{T}_{s2}$, and $\tilde{T}_g$, and real constants: $\overline{T_b}$, $\overline{T_{s1}}$, $\overline{T_{s2}}$, and $\overline{T_g}$, may be found by using the temperature continuity boundary conditions

$$\overline{T_b}(-l_s) = \overline{T_s}(-l_s) \quad , \quad \tilde{T}_b(-l_s) = \tilde{T}_s(-l_s) \quad , \tag{2.100}$$

$$\overline{T_s}(0) = \overline{T_g}(0) \quad , \quad \tilde{T}_s(0) = \tilde{T}_g(0) \quad ; \tag{2.101}$$

and the flux continuity boundary conditions

$$k_b \frac{\partial}{\partial x}\overline{T_b}(-l_s) = k_s \frac{\partial}{\partial x}\overline{T_s}(-l_s) \quad , \quad k_b \frac{\partial}{\partial x}\tilde{T}_g(-l_s) = k_s \frac{\partial}{\partial x}\tilde{T}_s(-l_s) \quad , \tag{2.102}$$

$$k_s \frac{\partial}{\partial x}\overline{T_s}(0) = k_g \frac{\partial}{\partial x}\overline{T_g}(0) \quad , \quad k_s \frac{\partial}{\partial x}\tilde{T}_s(0) = k_g \frac{\partial}{\partial x}\tilde{T}_g(0) \quad . \tag{2.103}$$

Our main interest is in $\tilde{T}_g$, the complex amplitude of the periodic temperature at the solid-gas interface. Rosencwaig [23-24] expresses $\tilde{T}_g$ as

$$\tilde{T}_g = \frac{\alpha\kappa\tilde{I}}{2k_s(\alpha^2 - \xi_s^2)}\left[\frac{(s-1)(b+1)e^{\xi_s l_s}-(s+1)(b-1)e^{-\xi_s l_s}+2(b-s)e^{-\alpha l_s}}{(g+1)(b+1)e^{\xi_s l_s}-(g-1)(b-1)e^{-\xi_s l_s}}\right] , \quad (2.104)$$

where

$$b = \frac{k_b a_b}{k_s a_s} , \quad (2.105)$$

$$g = \frac{k_g a_g}{k_s a_s} , \quad (2.106)$$

and

$$s = \frac{(1+i)\alpha}{2a_s} = \frac{\alpha}{\xi_s} . \quad (2.107)$$

The actual temperature field within the gas is

$$T(x,t) = T_0 + \overline{T_g}\left(1 - \frac{x}{l_g}\right) + \mathrm{Re}\left[\tilde{T}_g\, e^{-\xi_g x}\, e^{-i\omega t}\right] . \quad (2.108)$$

The oscillatory temperature signal decreases rapidly as the distance from the solid-gas interface increases. In the typically short distance of $2\pi a_g^{-1}$ (0.16 cm in air at 100 Hz), the exponential falls to the value $e^{-2\pi} = 0.0019$. Thus we may consider the gas in this interval as the only gas which responds to the temperature variation, with its response being that it behaves as an acoustic piston, driving the remainder of the gas column. This acoustic piston will expand and contract sinusoidally and thus cause an acoustic pressure signal in the entire gas column. We first find the spatial average of the oscillatory temperature in this small interval:

$$<\tilde{T}_g> = \frac{a_g}{2\pi}\int_0^{2\pi a_g^{-1}} \tilde{T}_g(x)\,dx = \frac{a_g}{2\pi}\int_0^{2\pi a_g^{-1}} \tilde{T}_g\, e^{-i_g x}\,dx$$

$$= \frac{(1 - e^{-2\pi})}{2\pi(1 - i)}\tilde{T}_g \approx \frac{(1 + i)}{4\pi}\tilde{T}_g \quad . \tag{2.109}$$

Note that we have used $e^{-2\pi} << 1$, and note that the phase angle between $<\tilde{T}_g>$ and $\tilde{T}_g$ is 45 degrees. The displacement of the acoustic piston is estimated by using the ideal gas law,

$$\tilde{x} = \frac{2\pi a_g^{-1}}{T_0 + \overline{T_g}}<\tilde{T}_g> = \frac{a_g^{-1}(1 + i)}{2(T_0 + \overline{T_g})}\tilde{T}_g \quad , \tag{2.110}$$

where we used

$$T_0 + \overline{T_g}\left[1 - \frac{\pi}{l_g a_g}\right] \approx T_0 + \overline{T_g} \tag{2.111}$$

for the average dc temperature in the layer. We now assume adiabatic expansion (pV^γ = constant) for the rest of the gas to obtain

$$\tilde{p} = \frac{-\gamma p_A}{l_g}\tilde{x} = \frac{-\gamma p_A(1 + i)}{2l_g a_g(T_0 + \overline{T_g})}\tilde{T}_g \quad . \tag{2.112}$$

Under ordinary conditions, we may neglect the average gas temperature increase $\overline{T_g}$ with respect to the ambient temperature T_0, so that equations (2.104) and (2.112) can be combined to obtain

$$\tilde{p} = \frac{-\alpha\kappa\gamma p_A(1+i)\tilde{I}}{4k_s l_g a_g T_0(\alpha^2 - \xi_s^2)}$$

$$\times \left[\frac{(s-1)(b+1)e^{\xi_s l_s} - (r+1)(b-1)e^{-\xi_s l_s} + 2(b-s)e^{-\alpha l_s}}{(g+1)(b+1)e^{\xi_s l_s} - (g-1)(b-1)e^{-\xi_s l_s}} \right] . \qquad (2.113)$$

The complexity of equation (2.113) makes it difficult to gain physical insight into the pressure signal generation process. Rosencwaig has examined six special cases in which the expression for $\tilde{p}$ simplifies considerably. We are primarily interested in three of these cases which help in understanding the background signal due to window bulk absorption, window film absorption, and scattered light absorption by the walls.

2.2.3 Window Bulk Absorption

The RG theory assumes that absorption of light occurs only in the sample material (Figure 2.6). Therefore, in order to study the result of window bulk absorption, we will assume that the sample material represents the window of a spectrophone. It is assumed that the thermal properties of the backing material are the same as those of the sample (window) material (i.e., $b \sim 1$). Later, we will discover that this is not a restrictive condition. Also, we assume that the sample (window) is optically transparent ($e^{-\alpha l_s} \approx 1-\alpha l_s$, $\alpha << a_s$, and $|s| << 1$) and that $k_g a_g << k_s a_s$ (i.e., $g << b$). Finally, we assume that the window is thermally thick, $l_s > a_s^{-1}$, which is reasonable except for very low modulation frequencies. Using these assumptions, (2.113) reduces to

$$\tilde{p} = \frac{\gamma p_A \kappa}{l_g T_0} \left[\frac{(1-i)\alpha_w}{8 a_g a_w} \right] \left[\frac{1}{k_w a_w} \right] \tilde{I} , \qquad (2.114)$$

where we have used the subscript w to denote properties of the window. The pressure signal is proportional to $\alpha_w a_w^{-1}$, which indicates that only the light absorbed

within one thermal diffusion length of the inner surface of the window material contributes to the background signal. The signal is independent of the window thickness and the properties of the backing material. However, the signal does depend on the thermal properties of the window and gas. Since $a_g \propto p_A^{\frac{1}{2}} T_0^{-\frac{1}{2}}$, the overall dependence on the ambient pressure and temperature is $p_A^{\frac{1}{2}}$ and $T_0^{-\frac{1}{2}}$, respectively. The overall frequency dependence is also found from the definition of a to be $\omega^{-1.5}$. For uniform illumination, $\tilde{I} = l_g V_c^{-1} \tilde{W}$, and we see that the window bulk absorption background signal is inversely proportional to the cell volume. The results of this section were verified by starting with the geometry of Figure 2.6, but without the backing material. Similar boundary conditions and assumptions were used, with the only major difference being a small left traveling thermal wave within the gas. The resulting pressure signal was identical to (2.114).

As a numerical example of the background signal expected from window bulk absorption, we will assume the geometry of our Stark spectrophone (OAD-2), a modulation frequency of 13 Hz, a gas sample of air at 50 torr total pressure, and ZnSe windows. Table 2.5 lists the parameter values that are not in table 2.4.

TABLE 2.5. SUMMARY OF EXAMPLE PARAMETER VALUES.

$f = 13$ Hz
$\gamma = 1.4$
$p_A = 6.67 \times 10^3$ Pa
$\kappa = 1$
$l_g = 2 \times 10^{-2}$ m
$T_0 = 300$ K
$\lvert\tilde{W}\rvert = 0.5$ W
$V_c = 1.36 \times 10^{-7}$ m^3

Inserting these values into (2.114), we obtain

$$|\tilde{p}| = 1.47 \times 10^{-4} \text{ Pa} \quad , \tag{2.115}$$

or, using the coupled microphone-preamplifier sensitivity of 39.9 mV/Pa,

$$|\tilde{v}| = 5.86 \times 10^{-6} \text{ V} \quad . \tag{2.116}$$

Note that these results are for a single window-gas interface, whereas a typical spectrophone (as well as our Stark spectrophone) has two windows.

2.2.4 Window Surface Absorption

We now wish to examine the case of absorption by a thin film on the inside surface of a spectrophone window. Referring to Figure 2.6, we let the sample material represent the film (f), and the backing material represent the nonabsorbing window (w). Starting again with equation (2.113), we let $l_s \to 0$, $k_g a_g << k_b a_b$ ($g << b$), and $e^{-\alpha l_s} \approx 1 - \alpha l_s$. No assumption is made about the thermal properties of the film (e.g. their relative size compared to the thermal properties of the window and gas). With these assumptions, (2.113) reduces to

$$\tilde{p} = \frac{\gamma p_A \kappa}{l_g T_0} \left[\frac{-i \alpha_f l_f}{4 a_g} \right] \left[\frac{1}{k_w a_w} \right] \tilde{I} \quad , \tag{2.117}$$

where the subscript f indicates properties of the film. This component of the background signal is directly proportional to the energy deposited in the film, $\alpha_f l_f \tilde{I}$, but remains dependent only on the thermal properties of the window and gas. The frequency dependence is now ω^{-1}, while the dependence on the remaining parameters is unchanged from the bulk absorption case.

Inserting the parameter values of Table 2.5, we obtain for the expected background signal due to window surface absorption:

$$|\tilde{p}| = 2.17 \times 10^{-3}\, \alpha_f l_f \text{ Pa} \quad , \tag{2.118}$$

and

$$|\tilde{v}| = 8.65 \times 10^{-5}\, \alpha_f l_f \text{ V} \quad . \tag{2.119}$$

The window surface contribution equals the window bulk contribution when $\alpha_f l_f = 0.068$.

2.2.5 Scattered Light

A third source of background signal in optoacoustic detection is scattered light which strikes the walls of the cell, is absorbed, and thus causes a synchronous heating of the gas. The light may be scattered by the cell windows, the alignment optics, the chopper blade, or possibly by aerosols in the gas.

Referring to Figure 2.6, we let the sample material represent the wall of the cell, which is usually a metal. The intensity of the scattered light striking the walls of a cylindrical spectrophone is given by

$$\tilde{I}_s = \frac{\kappa_s r_c}{2 l_c} \tilde{I} \quad , \tag{2.120}$$

where κ_s is the fraction of the incident power which is scattered onto the walls. Uniform scattering is assumed. We again start from (2.113) and assume that $g << b \approx 1$. Metal walls are optically opaque ($e^{-\alpha l_s} \approx 0$, $\alpha >> a_s$) and thermally thick ($e^{-\xi_s l_s} \approx 0$). With these assumptions, (2.113) becomes

$$\tilde{p} = \frac{\gamma p_A \kappa}{l_g T_0} \left[\frac{-i}{4 a_g}\right] \left[\frac{1}{k_m a_m}\right] \left[\frac{\kappa_s r_c}{2 l_g}\right] \tilde{I} \quad , \tag{2.121}$$

where the subscript m indicates properties of the metal cell walls. This component of the background signal is independent of the absorption coefficient of the wall. It does depend on the thermal properties of the wall and gas and it varies as ω^{-1}. The dependence on l_g is not clear, since κ_s may be a function of l_g. The dependence on pressure and temperature is the same as in the previous special cases.

Again inserting the example values of Table 2.5, we obtain for the expected background signal due to scattered light:

$$|\tilde{p}| = 2.3 \times 10^{-2}\, \kappa_s \text{ Pa} \quad , \tag{2.122}$$

and

$$|\tilde{v}| = 9.18 \times 10^{-4}\, \kappa_s \text{ V} \quad . \tag{2.123}$$

The scattered light contribution equals the window bulk contribution when $\kappa_s = 6.4 \times 10^{-3}$, which is more than four orders of magnitude greater than typical atmospheric aerosol scattering at 10 μm [27]. As was stated, however, light may also be scattered onto the cell walls by the optical elements, the chopper blade, etc.

2.2.6 Other Sources

Other sources of background signal include acoustic or vibrational pickup from the mechanical light chopper, absorption by microaerosols, and absorption by contaminants in the cell. We will see later that Stark modulation of the gas absorption eliminates all of the above sources of background signal. However, the oscillating Stark voltage can cause a synchronous background signal. We will also see later that the Stark voltage may be fixed and the absorption modulated by rotating the direction of the laser polarization. In this case, a background signal is observed which is probably due to polarization dependent window absorption or geometrical

reflections.

2.2.7 Summary

The background signal in optoacoustic detection limits the detectability and accuracy of the method. Sources of background signal include window bulk absorption, window surface absorption, and scattering of light into the cell walls. The background signal due to window bulk absorption depends on the thermal properties of the window and gas and is proportional to $p_A^{\frac{1}{2}} T_0^{-\frac{1}{2}} V_c^{-1} \omega^{-1.5} \alpha_w a_w^{-1} W$. (The microphone conversion stage is not included here since it is the same for all sources of a pressure disturbance). The signal due to window surface absorption also depends on the thermal properties of the window and gas and is proportional to $p_A^{\frac{1}{2}} T_0^{-\frac{1}{2}} V_c^{-1} \omega^{-1} \alpha_f l_f W$. The signal due to scattered light striking the walls depends on the thermal properties of the cell wall and gas and is proportional to $p_A^{\frac{1}{2}} T_0^{-\frac{1}{2}} V_c^{-1} \omega^{-1} W$. Thus bulk window absorption should be distinguishable by its frequency dependence.

2.3 Electrical Noise Sources

Figure 1.3 showed that noise enters each stage of the optoacoustic signal generation process. The two main sources of thermal noise which limit the ultimate sensitivity of optoacoustic detection are the thermal fluctuations of the gas and the electronic noise of the preamplifier. The brownian motion of the gas has already been discussed in section 2.1.4.3. The four main sources of noise in a typical FET preamplifier are Johnson noise from the resistor in the gate circuit, shot noise from the gate current, noise from the FET channel, and "1/f" noise from the transistor [28]. The noise power spectrum of a typical condenser microphone and preamplifier is given by [28]:

$$|v_n(\omega)|^2 = \frac{4k_BT}{R_bC_b^2\omega^2} + \frac{2qJ_g}{C_b^2\omega^2} + \frac{0.65}{g_m}4k_BT + \frac{B^2}{\omega} \left[V^2\text{-Hz}^{-1}\right] , \qquad (2.124)$$

where R_b is the microphone bias resistor, C_b is the biased microphone capacitance, J_g is the FET gate leakage current, g_m is the conductance of the transistor, and B is a constant of the "1/f" noise. It is clearly important to have a large gate (bias) resistor and a small gate current. Our Stark spectrophone employed a Bruel & Kjaer model 4144 capacitive microphone. Both Kreuzer [14] and Tarnow [28] have calculated the noise density for this microphone coupled to a typical FET preamplifier. Near 13 Hz, which was our primary modulation frequency, they calculated a density of approximately 4×10^{-7} V Hz$^{-\frac{1}{2}}$. Combining this value with our synchronous detection bandwidth of 0.125 Hz (1 sec. integration time), we find an expected noise voltage of about 0.1 μV.

Often, non-fundamental sources of noise can be much larger than the fundamental noise. These include noise spikes from the dc to dc converter in the preamplifier, which provides the microphone bias voltage, ambient room noise, which couples to the microphone, and 60 Hz line frequency pickup.

2.4 Chapter 2 References

[1] L.B. Kreuzer: J. Appl. Phys. 42(7), 2934-2943(1971)

[2] E.D. Hinkley, R.T. Ku, and P.L. Kelley: In "Laser Monitoring of the Atmosphere", ed. by E.D. Hinkley (Springer-Verlag, Berlin 1976), Ch. 6

[3] F.H. Lohman: J. Chem. Educ. 32, 155(1955) (This is also known as the Beer-Lambert equation or Bouger's law.)

[4] J.D. Stettler and N.M. Witriol: In "Optoacoustic Spectroscopy and Detection" ed. by Y.-H. Pao (Academic Press, New York 1977), Ch. 2

[5] A. Rosencwaig: "Photoacoustics and Photoacoustic Spectroscopy", (John Wiley & Sons, New York 1980)

[6] P.M. Morse and K.U. Ingard: In "Encyclopedia of Physics", ed. by S. Flugge, Volume XI/1 (Springer-Verlag, Berlin 1961)

[7] K.U. Ingard: In "Handbook of Physics", ed. by E.U. Condon and H. Odishaw (McGraw-Hill, New York 1958) Chapter 8

[8] P.M. Morse: "Vibration and Sound" (McGraw-Hill, New York 1948)

[9] M. Abramowitz and I.A. Stegun, (ed.): "Handbook of Mathematical Functions with Formulas, Graphs, and Mathematical Tables", (National Bureau of Standards, Washington, D.C., 1972)

[10] M.S. Shumate, R.T. Menzies, J.S. Margolis, and L.-G. Rosengren: Applied Optics 15(10), 2480-2488 (1976)

[11] L.L. Beranek: "Acoustic Measurements", (John Wiley & Sons, New York 1949)

[12] L.L. Beranek: "Acoustics", (McGraw-Hill, New York 1954)

[13] C. Kittel: "Elementary Statistical Physics", (John Wiley & Sons, New York 1958) Part 2

[14] L.B. Kreuzer: In "Optoacoustic Spectroscopy and Detection", ed. by Y.-H. Pao, (Academic Press, New York 1977) Chapter 1

[15] L.-G. Rosengren: Infrared Physics 13, 173-182(1973)

[16] C.C. Davis: Applied Physics Letters 36(7), 515-518(1980)

[17] W.W. Seto: "Acoustics", (McGraw-Hill, New York, 1971), Schaum's Outline Series

[18] F.W. Fraim, P.V. Murphy and R.J. Ferran, J. Acoustical Soc. Am. 53(6), 1601-1608(1973)

[19] C.K.N. Patel, Science 202, 157-173(1978)

[20] P.M. Morse and K.U. Ingard: 'Theoretical Acoustics", (McGraw-Hill, New York 1968)

[21] A. Rosencwaig and A. Gersho: Science 190, 556-557(1975)

[22] A. Rosencwaig and A. Gersho: J. Appl. Phys. 47(1), 64-69(1976)

[23] A. Rosencwaig: In "Optoacoustic Spectroscopy and Detection", ed. by Y.-H. Pao (Academic Press, New York 1977) Chapter 8

[24] A. Rosencwaig: In "Advances in Electronics and Electron Physics", Vol. 46, ed. by L. Marton (Academic Press, New York 1978) p. 207

[25] A. Rosencwaig: J. Appl. Phys. 49(5), 2905-2910(1978)

[26] A. Rosencwaig: "Photoacoustic and Photoacoustic Spectroscopy" (John Wiley & Sons, New York 1980) Volume 57 in "Chemical Analysis: A Series of Monographs on Analytical Chemistry and Its Applications", ed. by P.J. Elving and J.D. Winefordner

[27] W.L Wolfe and G.J. Zissis (ed.): "The Infrared Handbook" (Office of Naval Research, Washington, D.C., 1978)

[28] V. Tarnow: Bruel & Kjaer Technical Review 3, 3(1972)

3. EXPERIMENTAL APPARATUS

3.1 General Arrangement

A block diagram of the experimental apparatus is given in Figure 3.1. Note that some of the components were used only in the conventional chopped laser radiation mode, while others were used only in the Stark voltage modulation mode. The optical elements were securely mounted on an optical table. The results of an accelerometer test on the table were available and showed that the vertical rms acceleration at 13 Hz was about 10^{-5}g, 35 dB below the value near dc. Figure 3.1 does not show the half-wave plate used to rotate the direction of polarization of the illuminating radiation, the ancillary equipment needed to operate the CO_2 laser (power, cooling, gases), or the gas handling station built for filling and evacuating the optoacoustic detector. We will now briefly describe each component.

3.2 The Stark Spectrophone

The Stark spectrophone cell is depicted in Figure 3.2. The top and bottom consist of two semicylindrical pieces of 304 stainless steel. Both flat surfaces are highly polished and face each other with a separation of approximately 1 mm. They serve both as cell walls and as the electrodes for application of the Stark field to the gas sample. The electrode separation is established at the edges of the electrodes by spacers (not shown) of glass strips cut from a microscope slide. These strips also form the side walls of the cell. The optical end windows were cut from a single 1.560" x 0.6" x 0.080" uncoated ZnSe window purchased from II-VI Inc. These windows had a maximum wedge angle of 1.5 minutes, and were mounted so as to cancel any net wedge angle. The windows, spacers, and top and bottom of the cell were glued together with Armstrong A12 epoxy. The interior length of the cell was 20 mm, and the width of the gas volume was 1 1.8 mm in the original spectrophone (OAD-1) and 2 mm in a second spectrophone (OAD-2). The electrode spacing was chosen large

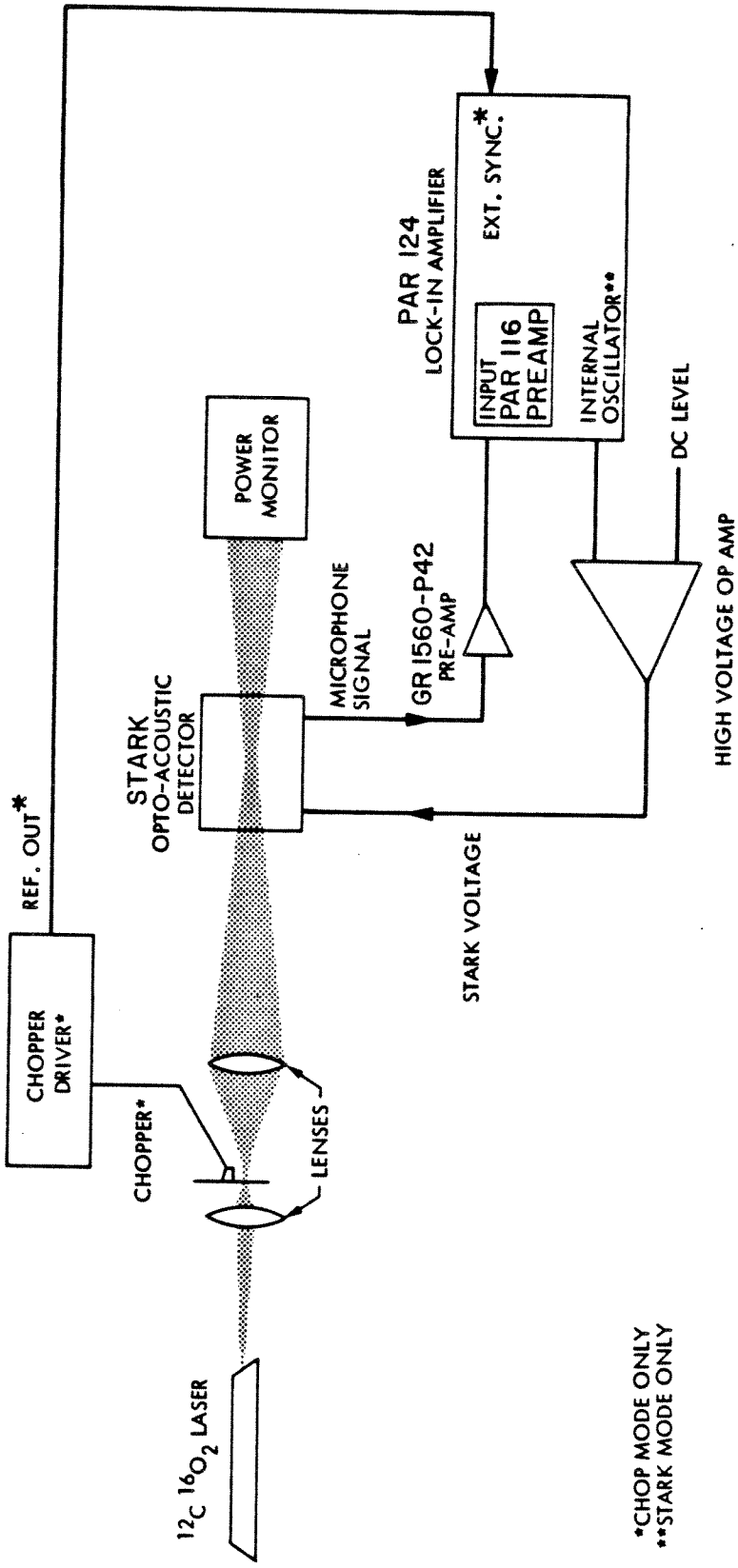

Figure 3.1. Block diagram of the experimental apparatus.

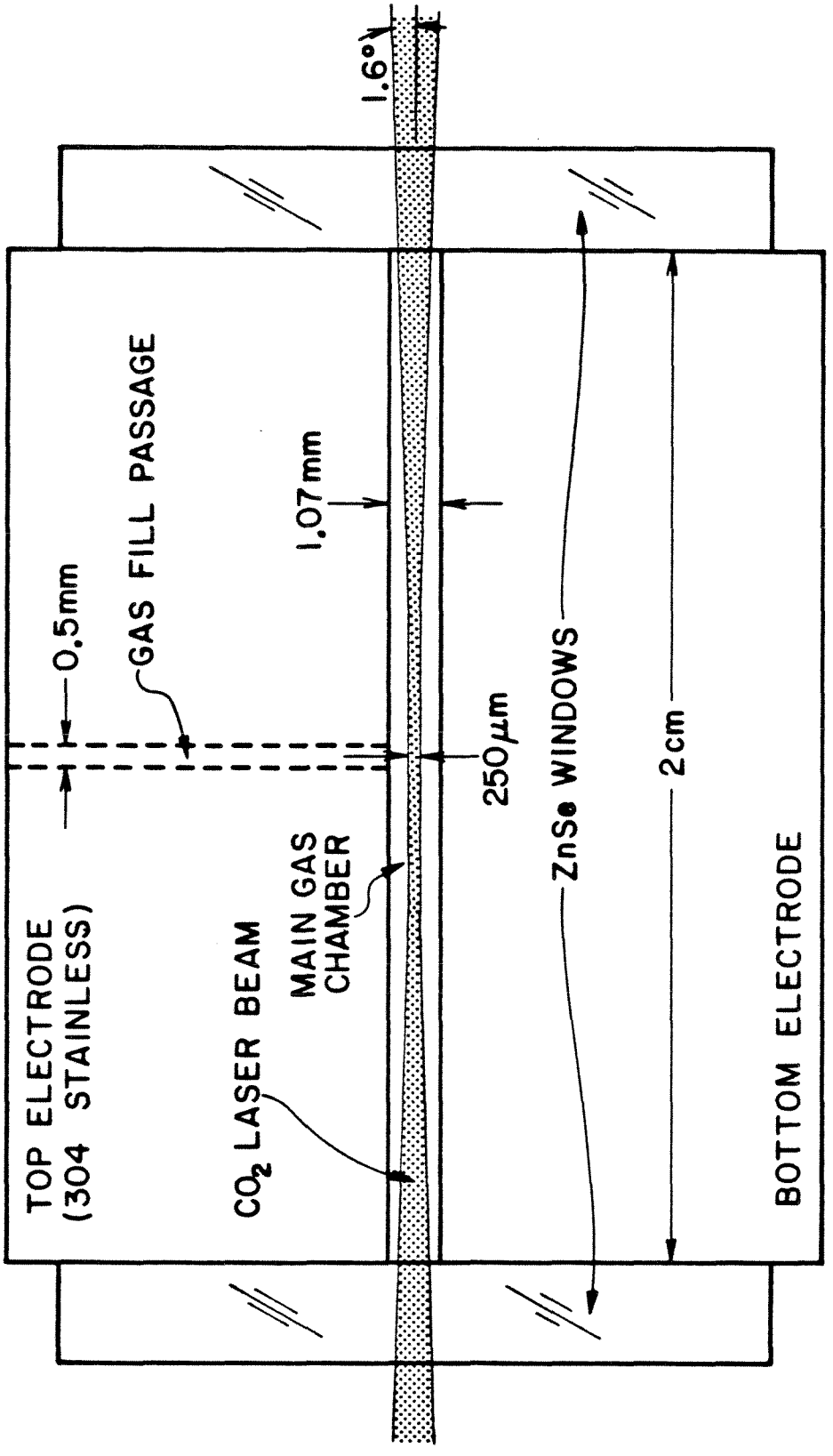

Figure 3.2. Scale drawing of the Stark spectrophone cell (OAD-2).

enough to avoid vignetting of the focused laser beam while still allowing the largest possible range of electric field values within the 0 to 1000 volt limits of our high voltage operational amplifier. The stainless steel electrodes were polished in order to minimize their absorption of scattered radiation and the resultant background signal. The windows were mounted perpendicular to the beam so that surface reflections would remain on-axis and not strike the inside walls of the spectrophone. (Brewster-angle windows would have required a steep angle of approximately 67° and would have also precluded operation in the rotating polarization mode described in Chapter 6). The glass spacers permitted parallel electrodes, a small spectrophone volume, and a uniform electric field over the laser-gas interaction volume.

A stainless steel mount, which is depicted in Figure 3.3, was fabricated to securely hold the delicate spectrophone cell for optical alignment; this mount also encased the microphone and allowed acoustic communication between the spectrophone and microphone. The mount was provided with a gas fitting and valve for filling and evacuating the spectrophone, and the gas path was designed to minimize the enclosed volume when the valve was closed. The clearance between the microphone diaphragm and mount was approximately 0.005 inches. This small volume was connected to the spectrophone cell through two small passages which were each angled at 30°, joining to form a dogleg, in order to minimize any interaction between the Stark electric field and the microphone. The diameters of the upper and lower passages were 1.5 mm and 0.5 mm, respectively, and each passage was 12.7 mm long. An o-ring seal was used at the spectrophone/mount interface.

It was necessary to measure the maximum Stark voltage that could be applied to the electrodes without causing an arc, which could conceivably damage the preamplifier or lock-in amplifier. A Lansing 80.310 high voltage power supply was connected to the smaller volume spectrophone (OAD-2) through a 10 MΩ resistance. A Fluke 8020A digital multimeter with high voltage probe was used to monitor the

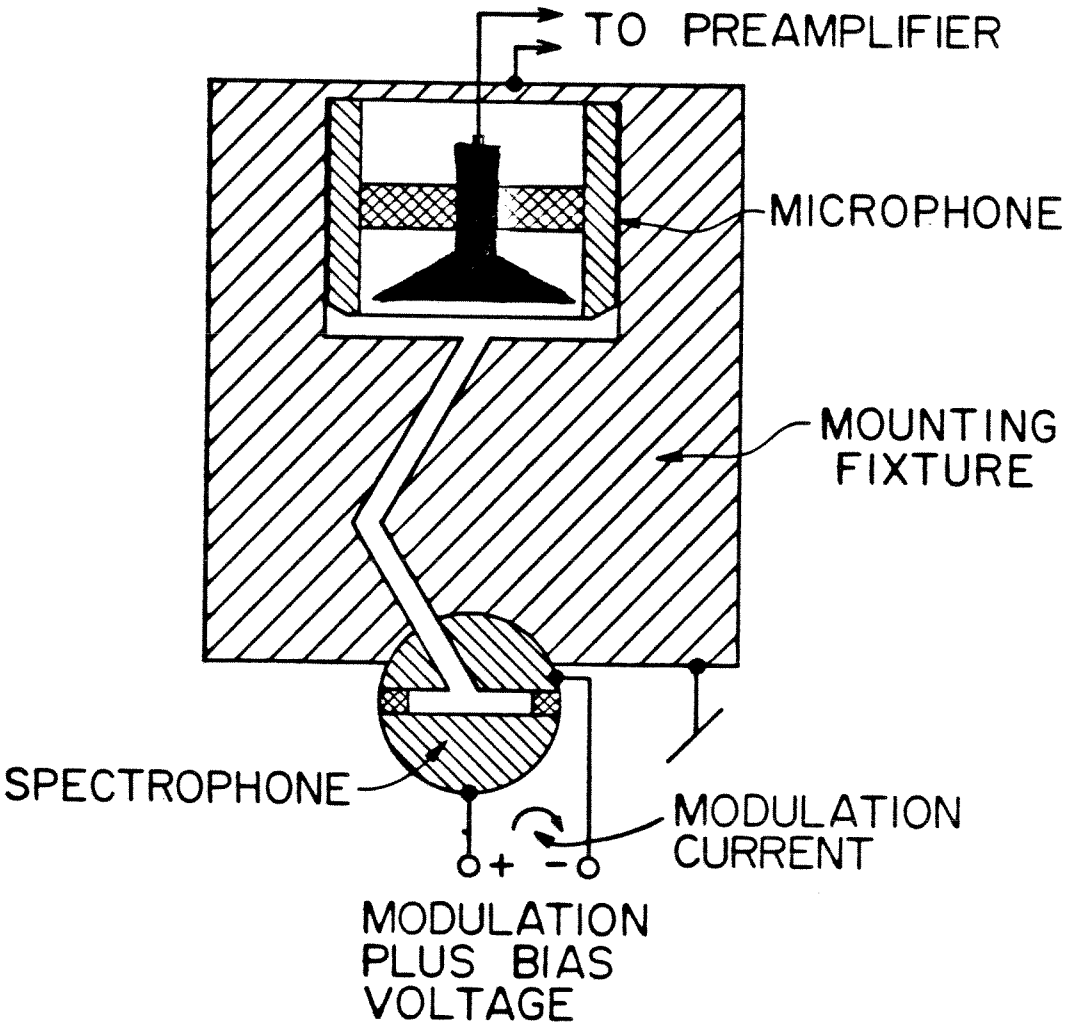

Figure 3.3. Pictorial drawing of the Stark spectrophone cell and microphone in the mounting fixture.

Lansing output voltage. For various pressures of pure N_2 in the spectrophone, the voltage was increased until an arc started, and then was decreased until it extinguished. The extinguish voltage, plotted in Figure 3.4, was lower than the arcing voltage and was not exceeded during our measurements.

3.3 The Microphone

The microphone used in these experiments was a Bruel & Kjaer model 4144 condenser microphone. The theory of operation of this type of microphone was discussed in Chapter 2. The diameters of the nickel diaphragm and of the monel backplate are 17.4 mm and 13.2 mm, respectively, and the diaphragm-to-backplate separation is approximately 20 μm. With a polarizing voltage of 200 volts, the specified sensitivity and resonant frequency are 44.2 mV/Pa and 8 kHz, respectively (serial number 655524). The influence of ambient pressure is -0.3 dB per 100 mm Hg and the capacitance when polarized is nominally 55.2 pF. The pressure equalization arrangement provided by B&K to prevent diaphragm damage limits the lowest frequency of operation to between 1 Hz and 2 Hz. Care was taken to change the pressure inside the spectrophone at rates no greater than 10 torr/sec.

3.4 The Preamplifier

As shown in Figure 3.1, the microphone output signal connects directly to a General Radio model 1560-P42 preamplifier. The preamp functions both as an impedance transforming amplifier with a voltage gain of 1 or 10, and as a power supply providing the 200 volt polarizing voltage to the microphone. This voltage is generated with a built-in dc-to-dc converter operating at approximately 50 kHz and is supplied to the center conductor through a 1.2 GΩ dc source resistance. The input impedance is approximately 2 GΩ in parallel with < 6 pF. The output impedance is approximately 15 Ω in series with 3.3 μF. The main sources of preamplifier noise are the FET input stage and two input protection diodes. A gain of 1 was used in all

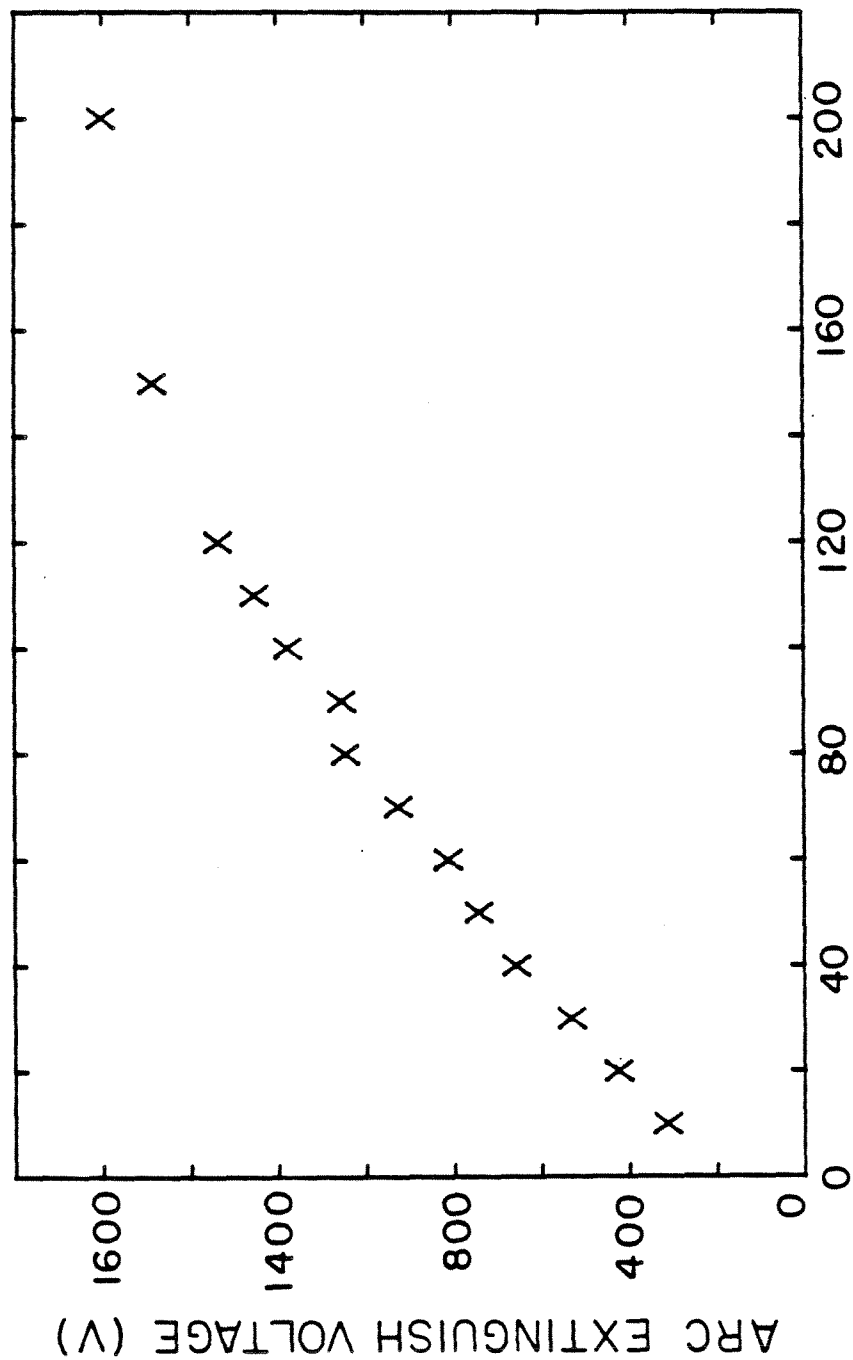

Figure 3.4. Experimental plot of the arc extinguish voltage vs. the total N_2 pressure in the Stark spectrophone cell (OAD-2).

the experiments of this report. The preamplifier was powered with 25 V dc at approximately 5 mA.

The coupled microphone and preamplifier sensitivity at low frequencies is given by [1]

$$S_{mp} = S_{oc}\, g\, \frac{C_b}{C_b + C_i} \quad , \tag{3.1}$$

where S_{oc} is the open circuit sensitivity of the microphone (2.81), g is the preamplifier voltage gain, C_b is the biased microphone capacitance, and C_i is the preamplifier input capacitance. Using the values [2,3] of our microphone and preamplifier,

$$S_{oc} = 44.2\ \frac{mV}{Pa} \quad , \quad g = 1 \quad , \quad C_b = 55.2\ pF \quad , \quad C_i \approx 6\ pF \quad , \tag{3.2}$$

we find that

$$S_{mp} = 39.9\ \ \frac{mV}{Pa} \quad . \tag{3.3}$$

3.5 Other Electronics

The output of the Genrad preamplifier was connected to the input of a Princeton Applied Research (PAR) model 116 plug-in differential preamplifier installed in a model 124 lock-in amplifier. The PAR preamp was used in the single-ended direct mode where its input impedance was 100 MΩ in parallel with 20 pF. Many of the experiments were conducted with a modulation frequency of 13 Hz and with an equivalent lock-in amplifier input bandpass filter Q of 15.7. Under these conditions, the 15 Ω source resistance contributes 0.45 nV of thermal noise, and the 116 preamp has a 30 dB noise figure (obtained from a contour plot) at 15 Ω and 13 Hz,

resulting in a total equivalent rms input noise of 14.1 nV. The integration time constant τ of the PAR 124 output low-pass filter was adjusted to 1 second and the filter's roll-off was 12 dB/octave resulting in an equivalent noise bandwidth (ENBW) of $1/8\tau$ = 0.125 Hz.

In the conventional chopped laser radiation mode, the reference waveform for the synchronous detector was supplied by the mechanical light chopper, a PAR model 191 variable-speed chopper. Chopping frequencies from 5 to 200 Hz (2.5-100 rev./sec.) were obtained with a two-aperature chopping wheel. The frequency stability of the 191 was 0.5%/hour and the phase jitter was < 0.5° rms.

In the Stark voltage modulation mode, the chopper was not used and the internal oscillator of the lock-in amplifier was amplified by a Burleigh PZ-70 high voltage operational amplifier and applied to the spectrophone's electrodes. The dc operating point of the Burleigh output voltage was adjustable from 0 to 1000 V and the ac output voltage was variable from 0 to 1000 V peak-to-peak (with dc plus ac not exceeding 1000 V). The Burleigh's frequency response was dc to 5 kHz. The laser power was monitored as it exited the spectrophone with a Scientech model 36-0001 1" surface absorbing disc calorimeter and model 36-1002 readout. The Scientech had a flat spectral response from 0.25 to 35 μm, an accuracy of ± 3%, and a 4 sec. time constant.

3.6 The Laser

The CO_2 laser used to illuminate the gas sample within the spectrophone was a low-pressure, passively stabilized laser previously built at JPL. The 1 m optical resonator consisted of a Littrow mounted grating blazed for peak efficiency at 10 μm (vertical polarization) and a 1 inch diameter 80% reflecting multilayer-coated ZnSe exit mirror with a 4 m spherical radius. The grating angle could be adjusted with a micrometer head to select one of more than 50 possible CO_2 rovibrational transi-

tions. The grating was also mounted on a cylindrical PZT stack for fine frequency tuning within each rovibrational line. An iris near the exit mirror was used to eliminate transverse modes. A slightly-tilted ZnSe window beyond the exit mirror provided the gas-tight seal at the front of the laser and also reflected a HeNe laser beam into a collinear path with the infrared beam for optical alignment purposes. The gas seal at the rear of the laser was made with a ZnSe window mounted at Brewster's angle for vertical polarization. The laser was typically operated with a 16 torr static mixture of He, N_2, CO_2, Xe, and H_2 in a 91:26:26:11:1 ratio. Each gas fill lasted several days and provided an output power of 3-5 W on the stronger lines.

3.7 Optical Components

Two BaF_2 lenses, with focal lengths of 10.2 cm and 23.8 cm at 10 μm, were used to focus the CO_2 laser beam to small waists at both the light chopper and the spectrophone. A narrow beam was necessary at the spectrophone due to the 1 mm spacing of the electrodes. Placing the chopper at a narrow beam waist minimized the background signal due to light scattered from the chopper blades striking the inside walls of the cell. The minimum beam waists at the chopper and spectrophone were approximately 90 μm and 120 μm, respectively. A CdS half-wave plate purchased from II-VI, inc. was placed in the beam path just in front of the cell entrance window in order to rotate the direction of the linear polarization of the laser beam. The resulting direction of polarization was determined by temporarily reflecting the output beam from a ZnSe flat at Brewster's angle and into a power monitor. The direction of polarization could be aligned either parallel or perpendicular to the electric field in the cell. The transmission of the 0.8" diameter half-wave plate was greater than 97%, it was flat to better than $\frac{\lambda}{40}$, its retardation was $\pm 2°$, and it was parallel to at least 2 arcseconds.

3.8 The Gases

3.8.1 Nitrogen

The spectrophone cell was filled with 99.9995% pure N_2 for background signal data, since its absorption at 10 μm is commonly taken to be unmeasurably small.

3.8.2 Ethylene

Ethylene (C_2H_4) was used for calibrating the responsivity of the Stark spectrophone because of its relatively large absorptivity, μ, at 760 torr, at the P(14) line of the 10.6 μm ($00^01 - 10^00$) band of the CO_2 laser. A commercial mix of 161 ppm C_2H_4 in N_2 was purchased from Linde. However, the value of μ as a function of pressure was not available, so it was measured at various total pressures, using homemade mixes of C_2H_4 in N_2 and a 36.5 cm long absorption cell. The results are shown as circles in Figure 3.5. Assuming that the absorption is due solely to a single pressure-broadened Lorentzian line, a least-squares fit to the data was generated, and is shown as the solid line. In addition, three published values of μ near 760 torr [4,5] are plotted as points A, B, and C. These values are slightly greater than an extrapolation of our data indicates. We believe this difference is due to one or more absorption wings of nearby C_2H_4 lines being pressure-broadened into a greater overlap with the CO_2 laser line. The remaining points plotted in Figure 3.5 will be discussed in the next chapter.

3.8.3 Monodeuterated Ammonia

For operation of the spectrophone in the Stark voltage modulation and Stark polarization modulation modes, monodeuterated ammonia (NH_2D) was studied as the absorbing gas and the P(20) line of the 10.6 μm band of the CO_2 laser was used as the radiation source. This molecule and laser wavelength were chosen because of their known Stark-shifted coincidence [6-9]. The highly asymmetric top NH_2D is closer to the prolate limit than to the oblate limit [10]. Its rotational energy levels

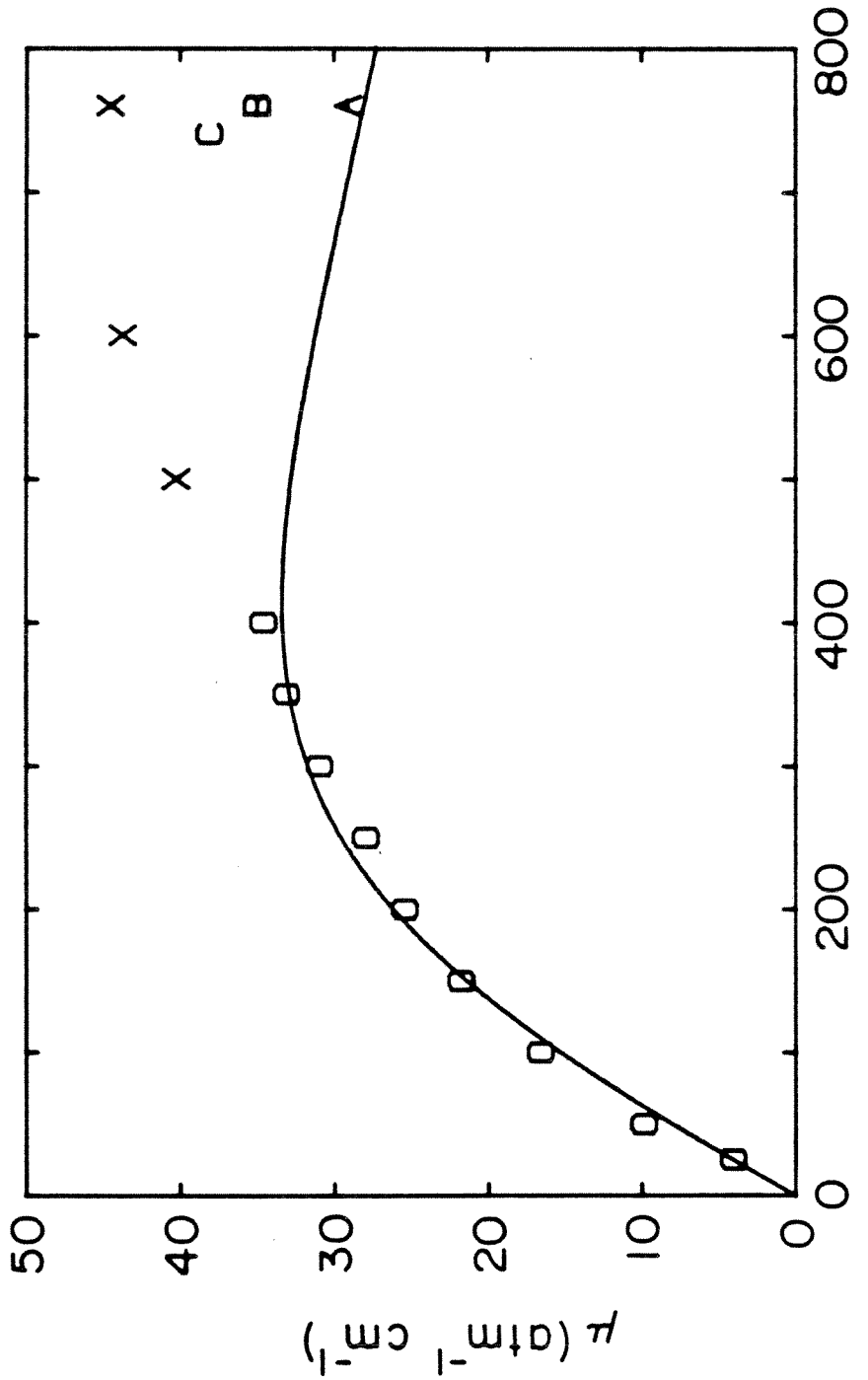

Figure 3.5. Absorptivity of C_2H_4 vs. total pressure at the P(14) CO_2 laser line: O - experimental data; solid curve - least-squares fit to a single Lorentzian line; A,B,C, - published values; X - calculated values using the spectrophone data and the extrapolated responsivity curve.

can only be described by including inversion doubling to the asymmetric top levels $J_{K_{-1}K_1}$, where J is the total angular momentum quantum number, K_{-1} is the prolate symmetric top quantum number for the projection of J on the principal axis of least moment of inertia, and K_1 is the oblate symmetric rotor quantum number for the projection of J on the principal axis of greatest moment of inertia. The inversion doubling is due to the pyramidal structure of ammonia which permits two equivalent positions of equilibrium for the nitrogen atom, one on each side of the plane of the hydrogen atoms. The inversion (umbrella) vibration is the ν_2 vibration and is specified by the quantum number v_2.

Figure 3.6 is a diagram of the energy levels of NH_2D relevent to this work. The rotational transition which can be Stark-tuned into coincidence with the CO_2 laser line is the $(\nu_2, J_{K_{-1}K_1}) = (0_a, 4_{04}) \rightarrow (1_a, 5_{05})$ transition. The letters s and a designate symmetric and antisymmetric wavefunctions with respect to a coordinate system inversion. The laser frequency (944.191 cm^{-1}) is shown coupled to the upper level of the transition; with zero Stark field it exceeds the transition frequency by 1720 MHz. Although the Stark effect in asymmetric rotors is usually second-order (proportional to E^2), two closely spaced "interacting" levels can give rise to a linear Stark effect (proportional to E) [11]. In this molecule, the ground state level $(0_a, 4_{04})$ of the transition of interest and the level $(0_s, 4_{14})$ are accidentally very close (644 MHz) [7], and are mixed by the applied electric field, thus repelling each other and splitting into M_J structure, where M_J is the component of the angular momentum in the direction of the field ($|M_J| = 0, 1, \cdots, J$). The selection rules for M_J are:

(1) $\Delta M_J = 0$: Laser polarization parallel to the Stark field;

(2) $\Delta M_J = \pm 1$: Laser polarization perpendicular to the Stark field.

The upper $(1_a, 5_{05})$ level is well away from other levels, and exhibits a second-order Stark effect. For the fields used in this study, the upper level shifts are negligible

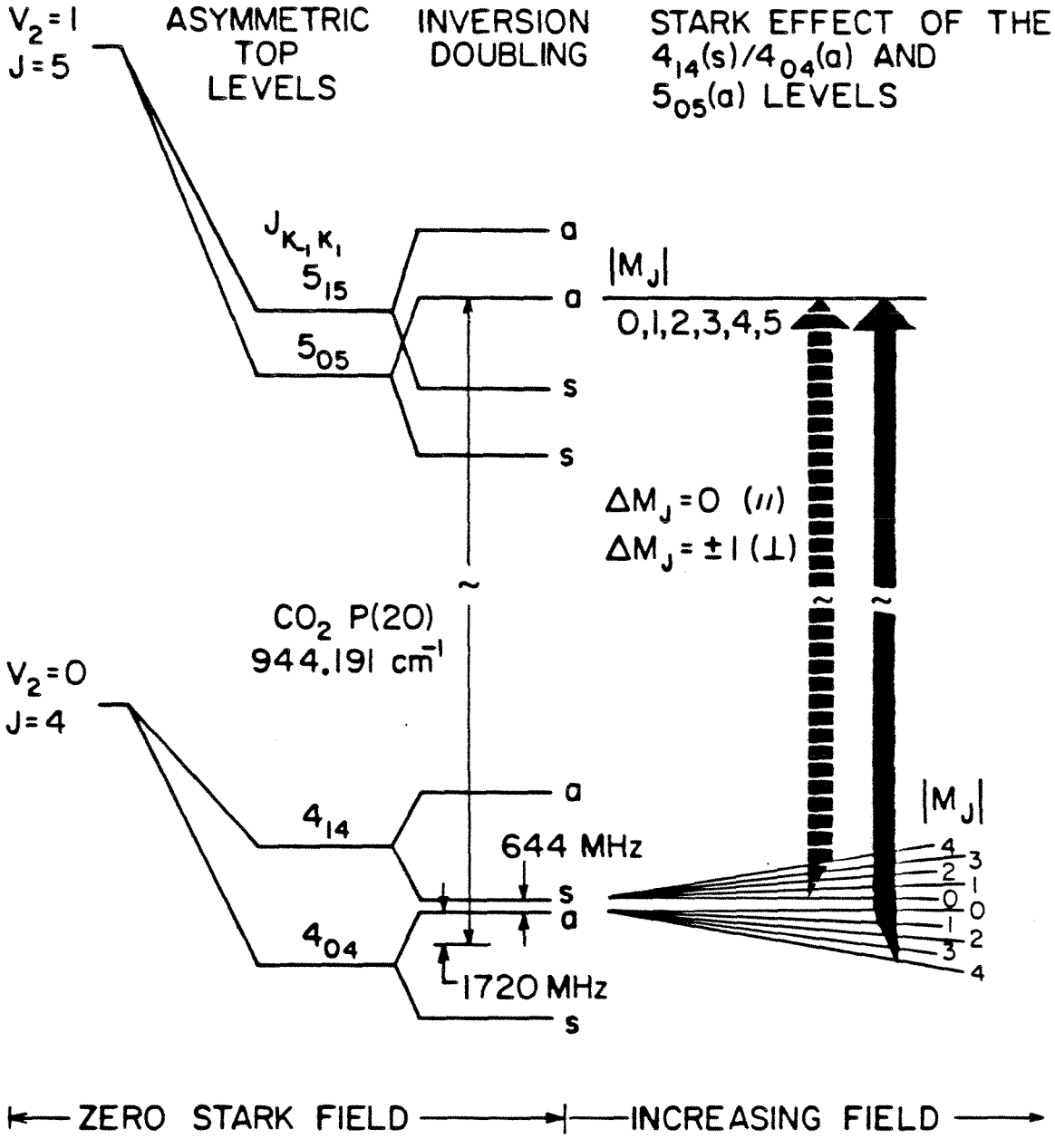

Figure 3.6. Stark effect energy level diagram of NH_2D showing levels relevant to the P(20) CO_2 laser line.

[8], and we therefore approximate that all the M_J components are degenerate with no Stark shift. Because of this degeneracy, the transition frequency for a given value of M_J in the lower level is independent of the direction of laser polarization. However, different relative intensities are expected for the two ΔM_J selection rules.

When a Stark field is applied, the energy of the coupled lower levels is given by

$$U = \frac{U_1 + U_2}{2} \pm \left[\left(\frac{U_1 - U_2}{2}\right)^2 + \Upsilon_{12}^2 E^2\right]^{\frac{1}{2}} , \tag{3.4}$$

where

$$\Upsilon_{12} = \frac{\Upsilon M_J K}{J(J+1)} , \tag{3.5}$$

and where Υ is the electric dipole moment, K is the quantum number for the appropriate limiting symmetric top, and U_1 and U_2 are the zero-field energies of the coupled levels [11]. Following Brewer et al [6], we approximate Υ with the value for NH_3 in its ground state (Υ = 1.468 Debye = 4.897×10^{-3} A-s-m [11]). Inserting this value in (3.5) and also the values J = 4 and K = 4 (in this case the coupled levels are equivalent to near degenerate levels of an oblate top), we find that in the high field limit, the laser frequency will exceed the NH_2D transition frequency by

$$\Delta f = 2042 - 1.48 \times 10^{-3} \, |M_J| E , \tag{3.6}$$

where Δf is in MHz and E is the applied field in Vm^{-1}. Nussmeier and Abrams [8] have more accurately determined the Stark shift slope as

$$\Delta f = 2042 - 1.43 \times 10^{-3} \, |M_J| E , \tag{3.7}$$

and this equation will be used in the following calculations. Since the laser frequency exceeds the transition frequency at zero field, as the field is increased, the highest $|M_J|$ lines will tune into coincidence at the lowest values of applied field (see Figure 3.6). Using (3.7) and the electrode spacing of the Stark spectrophone (1.07 mm), the various values of electric field (and Stark voltage v_s) may be calculated which yield $\Delta f = 0$. These values are given in Table 3.1.

TABLE 3.1. VALUES OF ELECTRIC FIELD AND STARK VOLTAGE REQUIRED FOR COINCIDENCE OF THE P(20) LASER LINE AND THE NH_2D TRANSITION.

$\|M_J\|$	E [Vm^{-1}]	v_s
4	3.57×10^5	381
3	4.76×10^5	508
2	7.14×10^5	762
1	1.43×10^6	1520

As the electric field increases, the symmetry of the $(0_s, 4_{14})$ and $(0_a, 4_{04})$ levels is no longer well-defined, and the zero-field wavefunctions are mixed. Lines correlating to the zero-field forbidden $(0_s, 4_{14}) \rightarrow (1_a, 5_{05})$ transition therefore grow in strength with increasing field and this causes the $(0_a, 4_{04}) \rightarrow (1_a, 5_{05})$ transition strength to diminish somewhat. Thus these lower frequency transitions, which are not directly observed with the P(20) laser line, take intensity away from the observed transitions. At very high fields, the "allowed" and "forbidden" transition groups will have equal intensities.

The theoretical Doppler width of NH_2D at room temperature is 82 MHz FWHM. Plant and Abrams [9] have measured a pressure-broadening coefficient of 40.2 ± 0.4 MHz/torr and a high-pressure limit of the $|M_J| = 4$ transition line center attenuation coefficient of 0.028 cm^{-1}. From (3.7), we see that at coincidence of the $|M_J| = 4$ transition, a 1% nonuniformity of the Stark electric field will produce an additional broadening of 20 MHz.

A mixture of Linde 99.995% pure NH_3 and Merck 99% pure ND_3 was prepared for the Stark modulation experiments, since the mixing results in a percentage of NH_2D. The resulting fraction of NH_2D as a function of the mixing fraction of NH_3 is shown in Figure 3.7. The maximum NH_2D fraction (4/9) is achieved with a 2:1 ratio of NH_3:ND_3.

3.9 Other Apparatus

The gas-handling station used to fill and evacuate the spectrophone was constructed from stainless steel in order to minimize the possibility of contamination. Pressure readings were made with a Hastings SP-1 0-20 torr thermocouple gauge, Wallace & Tiernan FA160 0.1-20 and 0-800 torr gauges, and MKS 221A 0-10 and 0-1000 torr capacitance manometers. Overnight pumping of the entire gas system with a Sargent-Welch oil-sealed rotary vane vacuum pump consistently reduced the pressure to 0.02 torr.

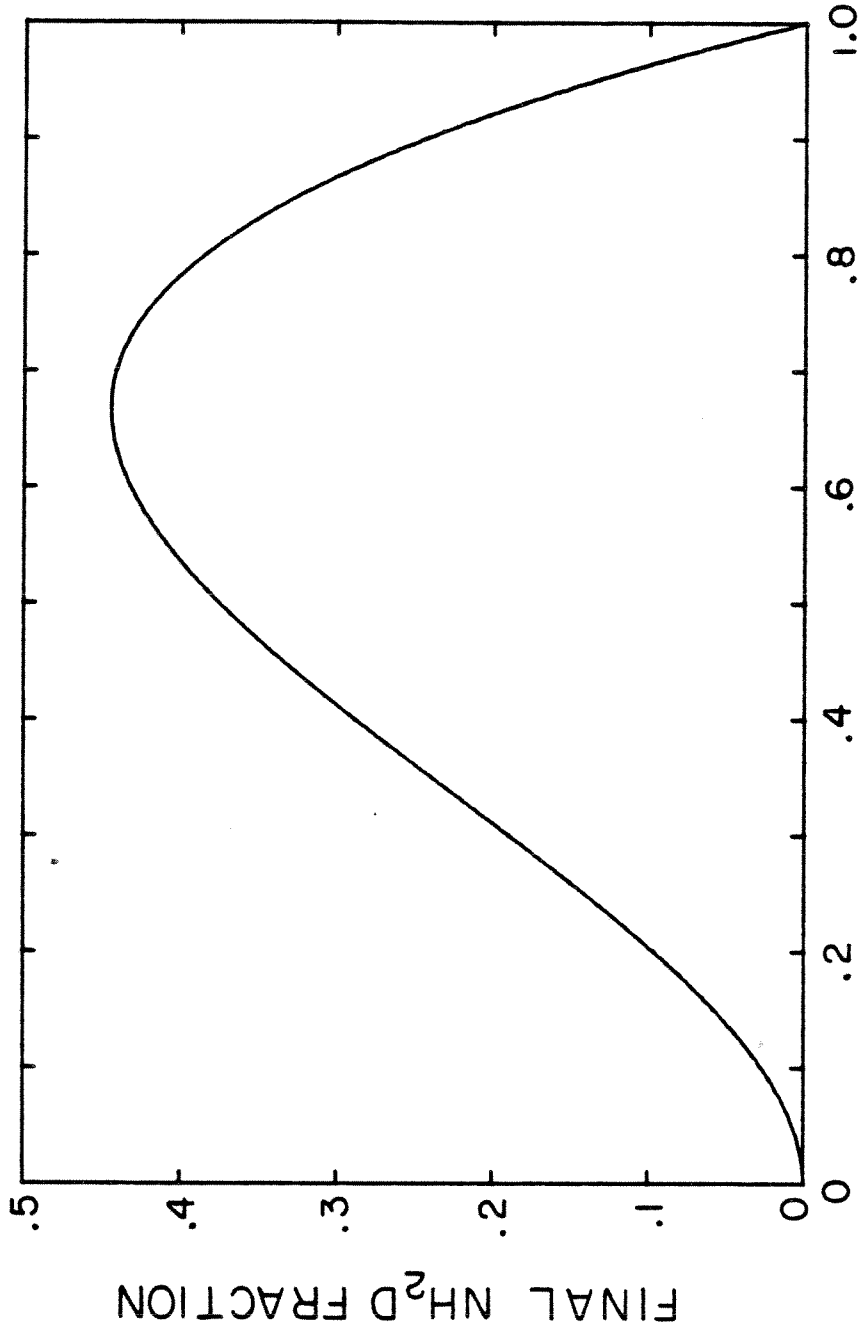

Figure 3.7. Theoretical graph of the final NH_2D fraction vs. the initial fraction of NH_3 in a mixture of NH_3 and ND_3.

3.10 Chapter 3 References

[1] "Condenser Microphones and Microphone Preamplifiers", (May 1977), Bruel & Kjaer DK-2850 Naerum, Denmark

[2] Bruel & Kjaer Calibration Chart for Condenser Microphone Cartridge Type 4144, Serial Number 655524 (May 26, 1977)

[3] Genrad Instruction Manual F, 1560-P42 Preamplifier (September 1976)

[4] R.R. Patty, G.M. Russworm, W.A. McClenny, and D.R. Morgan: Appl. Opt. 13(12), 2850-2854(Dec. 1974)

[5] R.A. Crane: RCA Report FXC 93 (Nov. 1976)

[6] R.G. Brewer, M.J. Kelly, and A. Javan: Phys. Rev. Lett. 23(11), 559-563 (Sept. 1969)

[7] M.J. Kelly, R.E. Francke, and M.S. Feld: J. Chem. Phys. 53, 2979-2980(1970)

[8] T.A. Nussmeier and R.L. Abrams: Appl. Phys. Lett. 25(10), 615-617(Nov. 1974)

[9] T.K. Plant and R.L. Abrams: J. Appl. Phys. 47(9), 4006-4008(Sept. 1976)

[10] M.T. Weiss and M.W.P. Strandberg: Phys. Rev. 83(3), 567-575(Aug. 1951)

[11] C.H. Townes and A.L. Schawlow: "Microwave Spectroscopy", (McGraw-Hill, New York, 1955), Ch. 10

4. CONVENTIONAL SPECTROPHONE OPERATION

4.1 Introduction

The spectrophone was first operated in the conventional chopped laser radiation mode for calibration and for comparison of its characteristics with theory and with the Stark voltage and Stark polarization modulation modes. The order of presentation of the chopped-mode data is not strictly chronological, since the experiments were initially performed with the first Stark spectrophone cell (OAD-1), and later, a more extensive set of chopped-mode experiments was performed with a second, lower volume Stark spectrophone cell (OAD-2). The smaller volume spectrophone cell was designed as an improved version of the original cell. This improvement consisted not only in the reduced volume, but also in the location of the Stark voltage electrical connections. The former improvement will be discussed in connection with the chopped-mode C_2H_4 data in the next section, and the latter improvement will be discussed in connection with the Stark voltage modulation mode in the next chapter. Although a number of improvements in equipment and experimental technique were implemented for the OAD-2 measurements, the initial OAD-1 data are included to allow comparison of the two spectrophone cells.

Operation in the conventional chopped laser radiation mode was accomplished as shown in Figure 3.1. No ac voltage was applied to the Stark electrodes, and the lock-in amplifier was synchronized to the reference waveform from the mechanical chopper. Both the chopper and the spectrophone cell were positioned at waists of the laser beam. The spectrophone cell was positioned for minimum background signal and maximum transmitted laser power, both of which occurred at the same position. The measured transmission of the evacuated cell was 60%, which agreed well with the expected value of 55% for four ZnSe-air interfaces. By translating the position of the chopper blade along the axis of the beam, it was observed that the

minimum background signal occurred at the minimum waist position. Both the in-phase and quadrature components of the lock-in signal were recorded at all times and each was normalized to the laser power as indicated by the Scientech power meter. The normalization power was equal to one-half of the peak power exiting the spectrophone when the chopper was used. Since the windows of the spectrophone each reflect a fraction of the beam, the Scientech provided only a relative measure of the actual laser power inside the spectrophone.

4.2 Ethylene

The minimum detectable absorption of a spectrophone is determined from its responsivity, background signal, and noise. It was desired to measure the responsivity, G, of the Stark spectrophone vs. the total pressure of the enclosed gas and vs. the modulation (chopping) frequency. The responsivity is defined as the output voltage of the preamplifier divided by the laser power incident on the gas and by the linear attenuation coefficient, α, of the gas mixture, and has units of $V/(W\text{-}cm^{-1})$.

The responsivity of the spectrophone was measured as follows. The CO_2 laser was adjusted to the P(14) line of the 10.6 μm band and the spectrophone cell was filled with the commercial mix of 161 ppm C_2H_4 in N_2. (The low concentration of C_2H_4 was necessary so that the thermodynamic properties of the gas mixture would closely match those of pure N_2, which was used to measure the background signal). As the total pressure and modulation frequency were stepped through various values, the in-phase and quadrature readings of the lock-in amplifier were recorded as well as the laser power corresponding to each reading. Each voltage reading was divided by the corresponding laser power, yielding data in V/W. The entire process was repeated with pure N_2 in the spectrophone. The N_2 data are referred to as the background signal. The true C_2H_4 signal was found by vectorially subtracting the N_2 data from the C_2H_4-N_2 mixture data. From the resulting 0° and 90° components, the

magnitude and phase of the C_2H_4 data were determined. The linear attenuation coefficient, α, is given by

$$\alpha = p_s \mu = 161 \times 10^{-6}\, p_A \mu \quad , \tag{4.1}$$

where p_s is the partial pressure of the absorbing gas, C_2H_4, in units of atmospheres. Dividing the magnitude of the C_2H_4 data by α yielded the experimentally measured responsivity G.

The experimental values for G were then fit to the theoretical expression for responsivity obtained from equation (2.82):

$$\tilde{G} = \frac{-v_b r_d^2}{8x_b\left[\gamma + \dfrac{(\pi r_d^2)^2 \gamma p_A (V_c + V_m)}{8\pi V_c V_m}\right]} \frac{i(\gamma-1)l_c}{\omega\left[1 + \dfrac{i}{\omega t_c}\right]V_c} \quad , \tag{4.2}$$

where it is assumed that the phase of $\tilde{W}$ is zero. Solving for the magnitude and phase angle of $\tilde{G}$, we find

$$G = |\tilde{G}| = \frac{v_b r_d^2 (\gamma-1) l_c}{8x_b V_c\left[\gamma + \dfrac{(\pi r_d^2)^2 \gamma p_A (V_c + V_m)}{8\pi V_c V_m}\right]\left[\omega^2 + \left[\dfrac{1}{t_c}\right]^2\right]^{\frac{1}{2}}} \quad , \tag{4.3}$$

and

$$\varphi_G = \tan^{-1}(\omega t_c) \quad . \tag{4.4}$$

Recalling from chapter 2 that the spectrophone's thermal time constant, t_c, is proportional to the total pressure, p_A, we can write the expected dependence of G on ω and p_A as:

$$G = \frac{1}{\left[D_1 + D_2 p_A\right]\left[\omega^2 + \left(\frac{D_3}{p_A}\right)^2\right]^{\frac{1}{2}}} \tag{4.5}$$

where

$$D_1 = \frac{8 x_b V_c Y}{v_b r_d^2 (\gamma - 1) l_c} \tag{4.6}$$

$$D_2 = \frac{x_b \pi r_d^2 \gamma (V_c + V_m)}{v_b (\gamma - 1) l_c V_m} \tag{4.7}$$

and

$$D_3 = \frac{p_A}{t_c} \tag{4.8}$$

The Responsivity

The experimental data for G and φ_G as functions of total pressure are shown in Figures 4.1 and 4.2. Measurements were made with both spectrophones at a modulation (chopping) frequency of approximately 13 Hz, and over a pressure range of 25-760 torr. Since the absorptivity, μ, was not accurately known above 400 torr (see Figure 3.5), the magnitude of the responsivity could not be accurately computed for the higher pressures. Figure 4.3 is a plot of the responsivity as a function of modulation frequency using the OAD-2 cell at total pressures of 300 and 760 torr. Again, only the 300 torr data could be converted to responsivity values using our measured values of μ, since the value of μ at 760 torr was not well known. The OAD-2 pressure data at 13 Hz in Figure 4.1 and the frequency data at 300 torr in Figure 4.3 were used to generate a least-squares estimate of the three coefficients in (4.5). With p_A

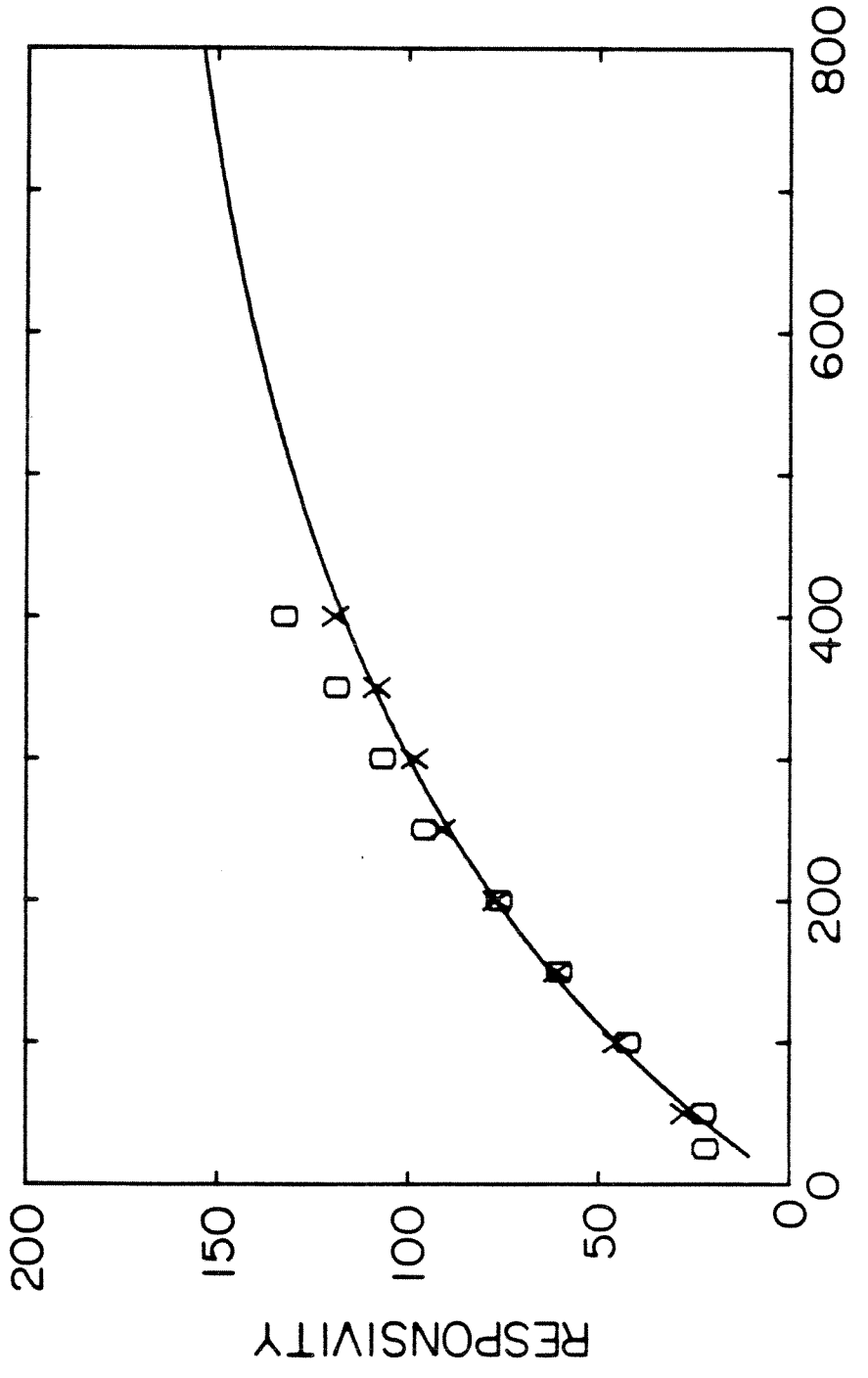

Figure 4.1. Magnitude of the spectrophone responsivity in $V\ W^{-1}(cm^{-1})^{-1}$ vs. total pressure at 13 Hz: 0 - OAD-1; X - OAD -2; solid line - least-squares fit to OAD-2 pressure data (shown here) and OAD-2 300 torr frequency data.

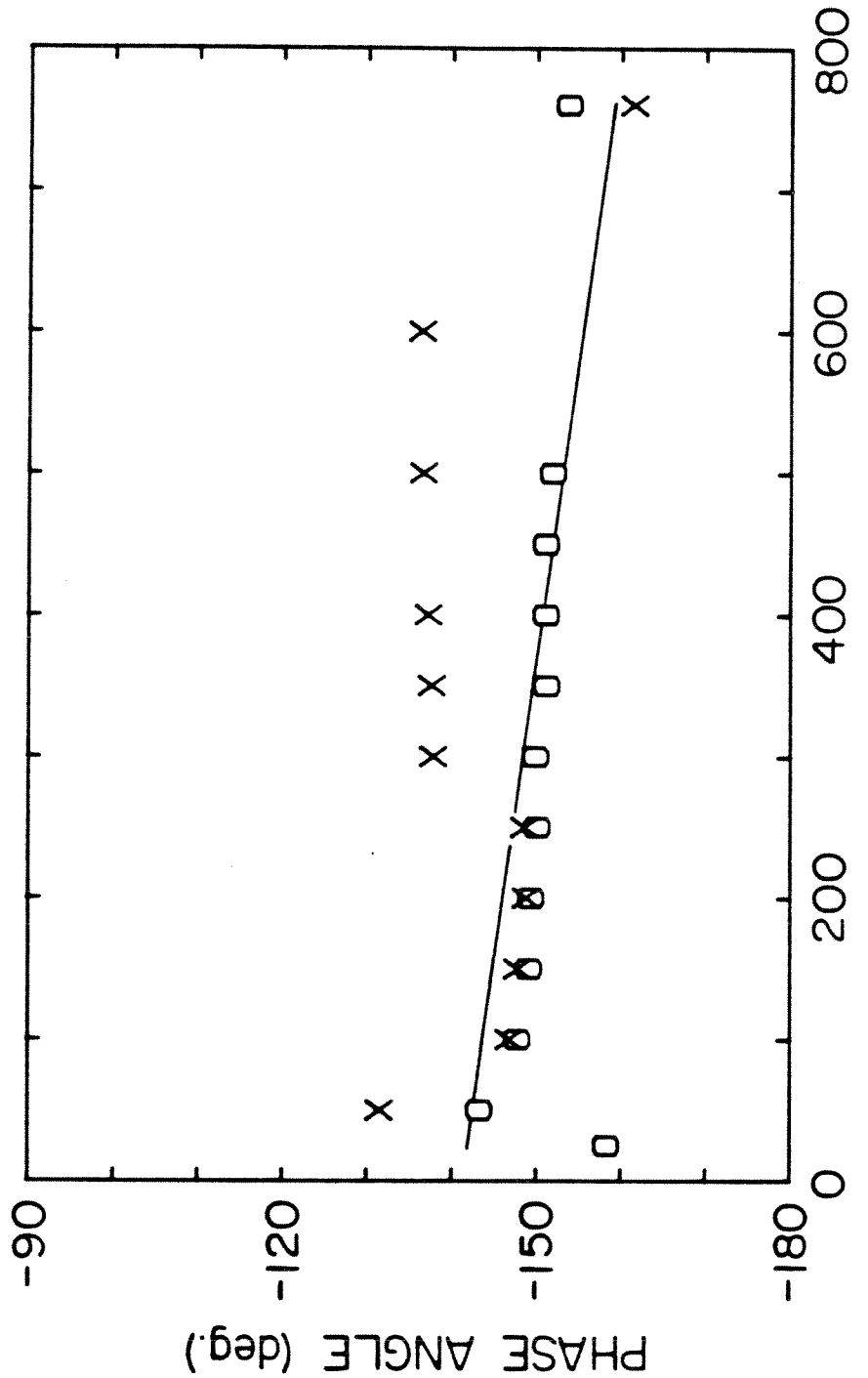

Figure 4.2. Phase angle of the spectrophone responsivity vs. total pressure at 13 Hz: O - OAD-1; X - OAD-2; solid line - theoretical slope of phase angle.

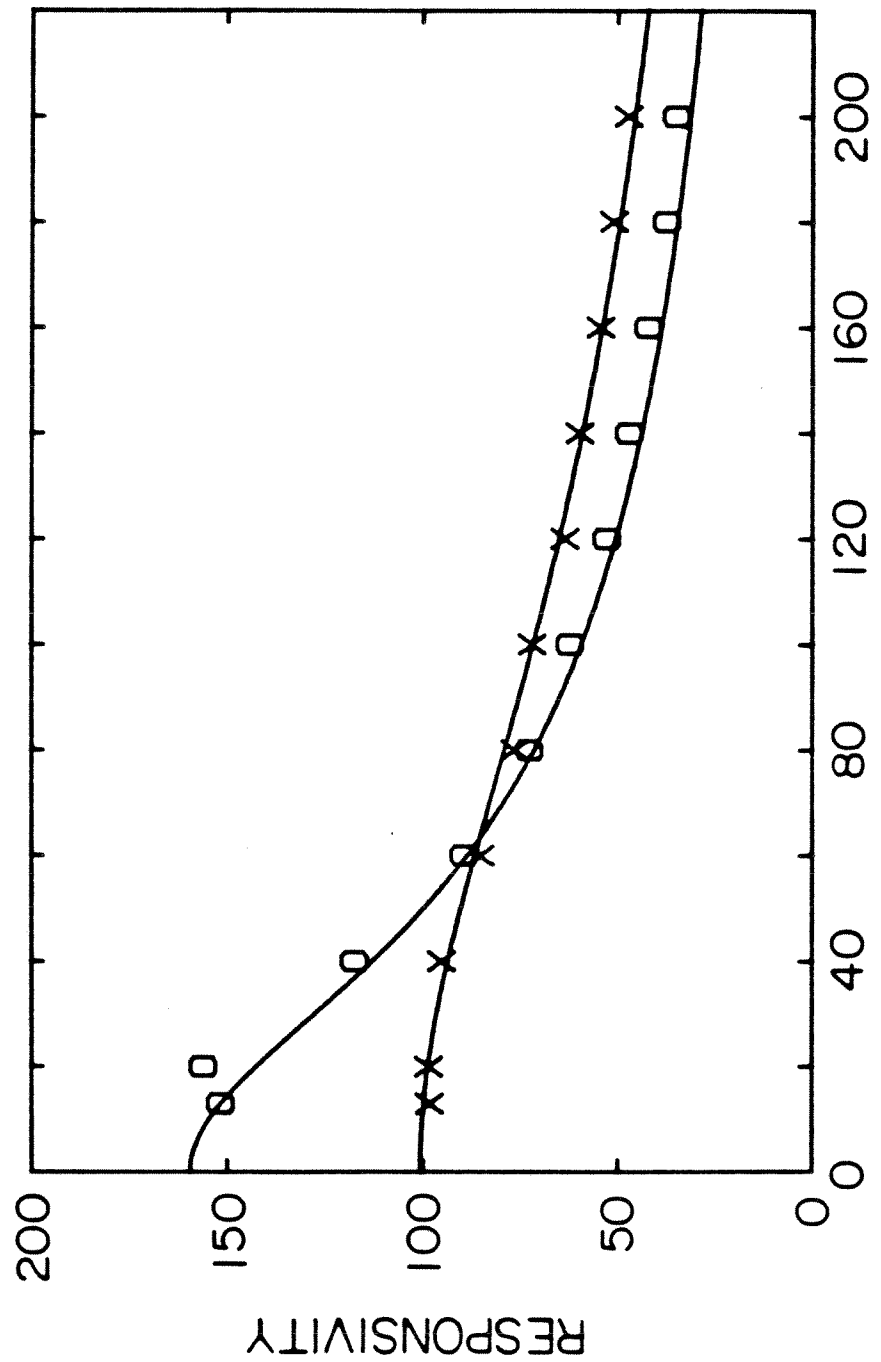

Figure 4.3. Magnitude of the OAD-2 responsivity in V $W^{-1}(cm^{-1})^{-1}$ vs. modulation frequency: O - 760 torr; X - 300 torr; solid curves - least-squares fit to 300 torr frequency data (shown here) and OAD-2 pressure data.

expressed in Pascals, the coefficients were determined to be:

$$D_1 = 9.49 \times 10^{-6}\ ,\ D_2 = 1.52 \times 10^{-10}\ ,\ \text{and}\ D_3 = 2.55 \times 10^{7}\ . \tag{4.9}$$

These coefficients were used in (4.5) to produce the solid curves in Figures 4.1 and 4.3. It is seen that the source data (X's) fit (4.5) very well. The responsivity curve in Figure 4.1 is shown extended to 800 torr. Using this extrapolated curve, the definition of responsivity, and the OAD-2 data at 500, 600, and 760 torr, an estimate of the absorptivity, μ, at these pressures was possible. These estimated values are plotted as X's in Figure 3.5. The calculated value of μ at 760 torr, 44.54 $atm^{-1}cm^{-1}$, was used to generate the points representing 760 torr in Figure 4.3. Considering the steps necessary to generate these points, their fit to (4.5) is very good.

A greater dependence of the responsivity on spectrophone volume was expected than is indicated in Figure 4.1. The main parallepiped volume and the total volume, V_c, of the OAD-2 were reduced by factors of approximately 5.7 and 2.5, respectively, from the original OAD-1. This is summarized in Table 4.1.

TABLE 4.1. STARK SPECTROPHONE CELL PARAMETER VALUES.

	OAD-1	OAD-2
l_x	1.18×10^{-2} m	2×10^{-3} m
l_y	1.04×10^{-3} m	1.07×10^{-3} m
l_z	2×10^{-2} m	2×10^{-2} m
$l_x l_y l_z$	2.45×10^{-7} m^3	4.27×10^{-8} m^3
Ancillary Volume	9.31×10^{-8} m^3	9.31×10^{-8} m^3
Total Volume V_c	3.39×10^{-7} m^3	1.36×10^{-7} m^3

From (4.3), we see that the responsitivy G can be independent of V_c if Y, the mechanical tension of the microphone diaphragm, is negligible compared to the other term in the brackets, if $V_m >> V_c$, and if t_c, the thermal heat conduction time of the cell, is independent of V_c. However, from the values of D_1 and D_2 in (4.9), it is clear that Y is not negligible and is equal to the other term when $p_A = 6.24 \times 10^4$ Pa = 468 torr.

Also, from (2.61), we expect that t_c will increase with increasing V_c. Differentiating (4.3) with respect to V_c, we obtain

$$\frac{\Delta G}{G} = -\frac{\Delta V_c}{V_c}\left[\frac{Y + \frac{(\pi r_d^2)^2 \gamma p_A}{8\pi V_m}}{Y + \frac{(\pi r_d^2)^2 \gamma p_A (V_c+V_m)}{8\pi V_c V_m}}\right] + \frac{\Delta t_c}{\left[\omega^2 + \frac{1}{t_c^2}\right] t_c^3} \quad . \tag{4.10}$$

If we let p_A = 468 torr, (4.10) becomes

$$\frac{\Delta G}{G} = -\frac{\Delta V_c}{2V_c}\left[\frac{2V_c + V_m}{V_c + V_m}\right] + \frac{\Delta t_c}{\left[\omega^2 + \frac{1}{t_c^2}\right] t_c^3} \quad , \tag{4.11}$$

and (4.8) and (4.9) yield

$$t_c = \frac{p_A}{D_3} = 2.45 \times 10^{-3}\ \text{s} \quad . \tag{4.12}$$

An approximate calculation from the Bruel & Kjaer 4144 drawings [1] yields

$$V_m \approx 9.2 \times 10^{-7}\ \text{m}^3 \quad . \tag{4.13}$$

Combining (4.11), (4.12) and (4.13), and the values in Table 4.1, the theoretical value of $\Delta G/G$ at 468 torr and 13 Hz when changing from the OAD-1 cell to the OAD-2 cell is -10% if we let $\frac{\Delta t_c}{t_c}$ = -50%. (The first term in (4.11) is +38% and the second term is -48%). These values were chosen since the measured change in G was approximately -10% at 400 torr (see Figure 4.1). The theoretical value of -50% for $\frac{\Delta t_c}{t_c}$ is reasonable since $\frac{\Delta V_c}{V_c}$ was -60%.

The experimental phase angle φ_G of Figure 4.2 was also compared to theory. Combining (4.4), (4.8), and (4.9), we obtain

$$\varphi_G = \tan^{-1}\left[\frac{2\pi f p_A}{2.55 \times 10^7}\right] . \qquad (4.14)$$

Of course, φ_G represents only the phase contributed by the physical processes included in (4.2), and the measured phase angle is a sum of φ_G and other phase angles. Specifically, it is assumed in (4.2) that only the zero-order pressure mode of the cell is excited, that ω is much less than the first microphone resonance and the molecular transition processes, and that the absorbing transition is not saturated. At f = 13 Hz, and with p_A ranging from 3.33×10^3 to 1.01×10^5 Pa (25-760 torr), we see from (4.14) that φ_G ranges from 0.6° to 18°. This dependence on p_A is shown in Figure 4.2 as a solid line which was translated vertically for the best fit to the OAD-1 data. The data in Figure 4.2 show the expected small variation in phase angle with pressure over most of the range. It is felt (in retrospect) that the level shifts in the OAD-2 phase angle data at 760 torr and 300 torr are due to resetting errors in the lock-in amplifier; the runs vs. frequency (Figure 4.3) were taken prior to these data points. Although the frequency settings of the lock-in amplifier and chopper were returned to 13 Hz before resuming the pressure reduction, small differences in the exact settings probably occurred, which caused the errors in the phase shifts. No level shifts occurred in the OAD-1 data of Figure 4.2 since no modulation frequency changes were made. Poor signal-to-background ratios at the lowest pressures probably caused the erratic phases there.

The Nitrogen Background Signal

The N_2 background signal vs. total pressure at 13 Hz is shown in Figure 4.4 for both spectrophones. The background signal vs. modulation frequency is given in

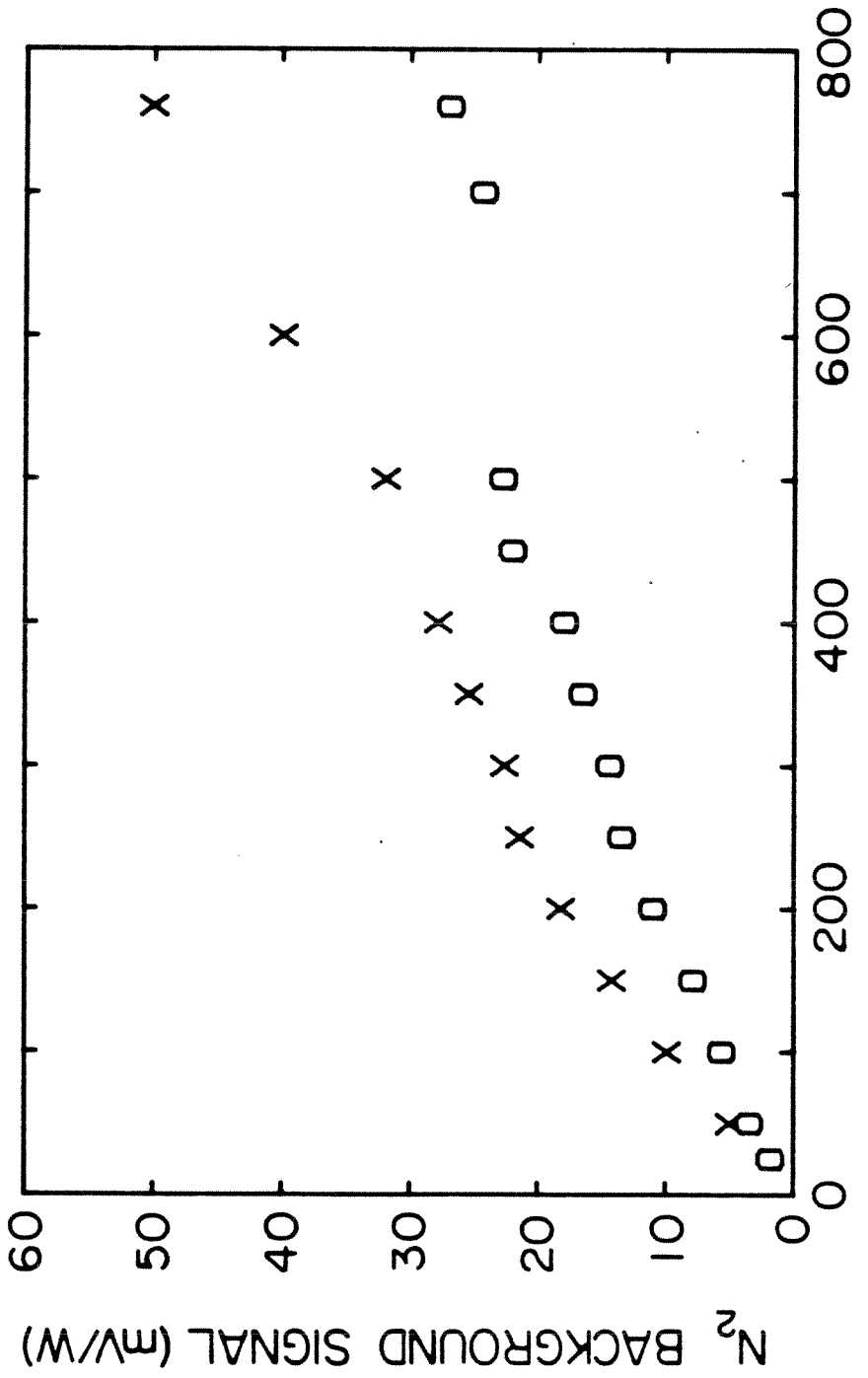

Figure 4.4. Background signal vs. total pressure at 13 Hz: O - OAD-1; X - OAD-2.

logarithmic coordinates in Figure 4.5 for the OAD-2 at 300 and 760 torr. In chapter 2, we saw that a simple one-dimensional theory for the background signal predicted a $V_c^{-1}p_A^{0.5}\omega^{-1.5}$ dependence from window bulk absorption and a $V_c^{-1}p_A^{0.5}\omega^{-1}$ dependence from window surface absorption or scattered light. It was assumed in that theory that

$$a_g^{-1} << l_g \quad , \tag{4.15}$$

where l_g was the length of the gas column, and where

$$a_g^{-1} = \left[\frac{2k_g}{\omega\rho_g C_p}\right]^{\frac{1}{2}} \quad , \tag{4.16}$$

is the thermal diffusion length in the gas. However, the smallest gas dimension in the Stark spectrophone is $l_y = 1.07 \times 10^{-3}$ m. At one atmosphere, (4.15) becomes an equality ($a_g^{-1} = l_y$) at f = 5.72 Hz and a 10:1 inequality only at f = 572 Hz. At 1/2 atmosphere, the required frequencies are doubled. Thus a three-dimensional theory which avoids the assumption in (4.15) would be required to predict the exact behavior of the background signal at our operating points. Of course, the microphone response term should also be included. Figure 4.4 reveals that the smaller volume OAD-2 does have a larger background signal, as expected. In Figure 4.5, the data above 40 Hz closely follow the predicted $p_A^{0.5}$ dependence, and the 300 torr data above 120 Hz exhibit an ω^{-1} dependence. The signal-to-background ratio of the OAD-2 data is listed in Table 4.2. This ratio increases with increasing pressure and and it appears that 760 torr and 140 Hz is the most attractive operating point among those listed. However, it is more meaningful to consider the minimum detectable absorption of the spectrophone. This is defined as the attenuation coefficient of the sample gas, α_{min}, which results in a unity signal-to-background

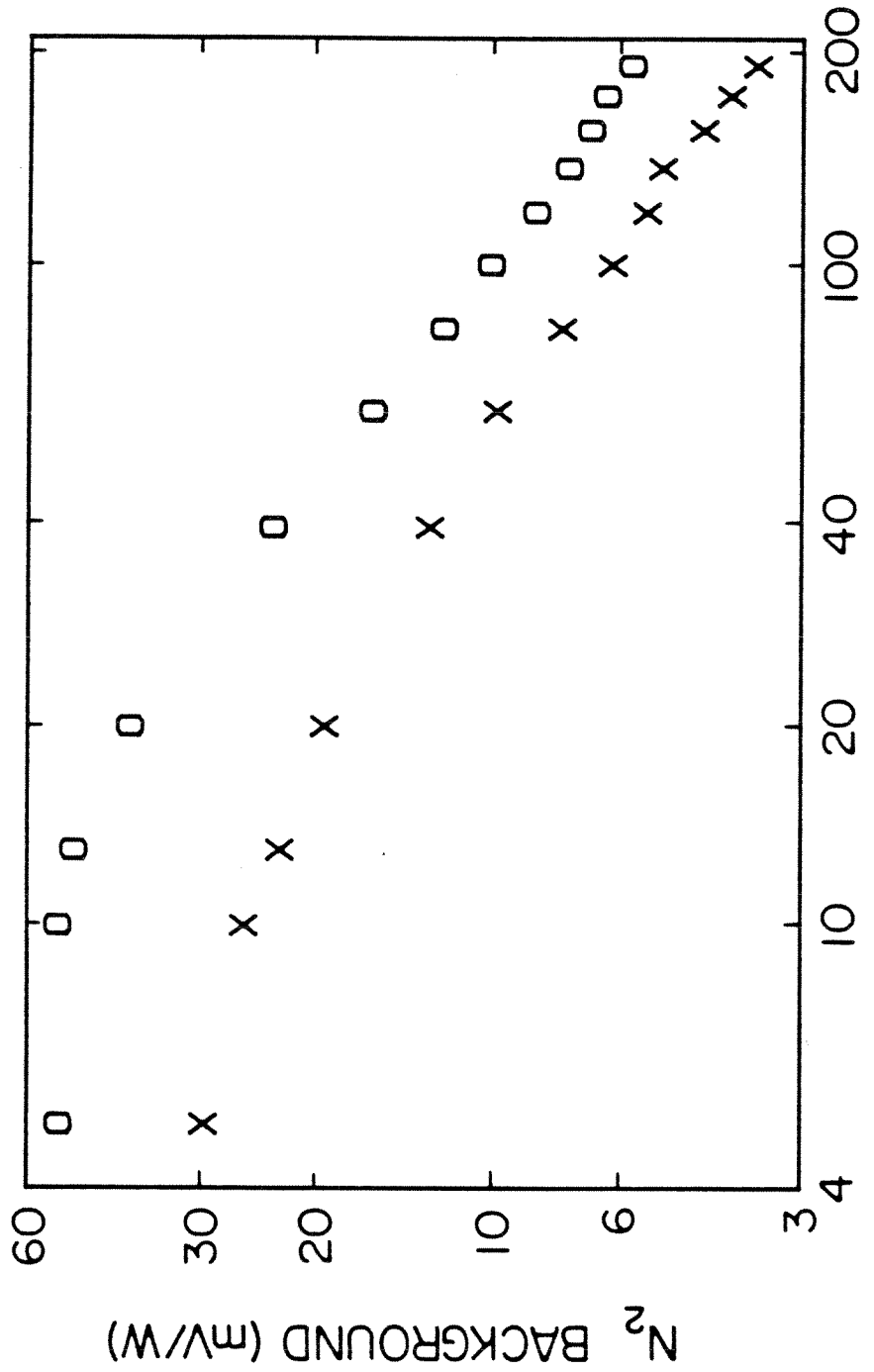

Figure 4.5. Logarithmic plot of OAD-2 background signal vs. modulation frequency: 0 - 760 torr; X - 300 torr.

TABLE 4.2. SUMMARY OF THE SIGNAL-TO-BACKGROUND RATIO AND THE MINIMUM DETECTABLE ATTENUATION COEFFICIENT CALCULATED FROM THE OAD-2 CHOPPED-MODE ETHYLENE DATA.

	$\frac{\text{signal}}{\text{background}}$		α_{min} [$\times 10^{-5}$ cm^{-1}]	
pressure [torr]	13 Hz		13 Hz	
760	22.7		33.0	
600	20.4		28.5	
500	18.2		24.5	
400	13.5		23.2	
350	11.3		23.5	
300	9.38		23.0	
250	6.97		23.5	
200	5.23		23.7	
150	3.64		23.4	
100	2.34		21.9	
50	1.32		18.0	
frequency [Hz]	300 torr	760 torr	300 torr	760 torr
200	26.7	44.3	→ 7.63	16.6
180	26.0	43.0	7.85	17.1
160	25.2	45.5	8.11	16.1
140	23.8	→ 46.7	8.55	→ 15.7
120	23.5	46.1	8.67	15.9
100	23.5	45.7	8.63	16.1
80	20.6	44.3	9.96	16.5
60	18.0	41.5	11.5	17.7
40	15.6	37.2	13.4	19.8
20	11.0	28.7	19.3	25.8
13	9.38	22.7	23.0	33.0

ratio. Thus we have

$$\alpha_{min} = \frac{\text{background signal}}{\text{responsivity}} \quad . \tag{4.17}$$

This value is also shown in Table 4.2. At pressure above 400 torr, the extrapolated values of G were used. Note that at 13 Hz, α_{min} depends very little on total pressure between 100 and 500 torr. At 760 torr, the lowest value is at 140 Hz. However, the best operating point is at 300 torr and 200 Hz, in contrast to the conclusion reached from the signal-to-background ratio.

4.3 Monodeuterated Ammonia

As stated earlier, monodeuterated ammonia (NH_2D) was chosen as the absorbing gas for operation in the Stark voltage modulation and Stark polarization modulation modes. As each of the spectrophone cells was operated in these new modes, chopped-mode measurements were also made in order to compare operation in the three modes and to verify the proper operation of the spectrophones. The chopped-mode results will be presented here; the comparison to the other modulation techniques will be done in the next two chapters.

4.3.1 The Stark Spectrophone Cell OAD-1

The NH_2D was made by mixing 400 torr each of NH_3 and ND_3 in a large manifold. In theory, this mixture partitions into NH_3:NH_2D:NHD_2:ND_3 in the ratios 1:3:3:1. The OAD-1 spectrophone was filled with 0.85 torr of this mixture and brought to a total pressure of 760 torr with pure N_2. Although a calculated 0.32 torr of NH_2D was placed in the spectrophone, an unknown fraction of the molecules are known to adsorb onto the walls and fill lines of the cell. The P(20) line of the 10.6 μm band of the CO_2 laser was used for all the NH_2D measurements. The R(8) CO_2 laser line was used in the chopped-mode to monitor NH_3 absorption (μ = 21.9 $atm^{-1}cm^{-1}$ [2]) in order to observe the stabilization of the gas fill, which typically took over 30 minutes, as determined from changes in the spectrophone signal. Concurrent chopped-mode and Stark voltage modulation mode measurements were then taken as the total pressure was lowered in discrete steps. No ac or dc Stark voltage was applied to the Stark electrodes of the cell for these chopped-mode measurements. The mechanical chopper, and the lock-in amplifier's internal oscillator and input bandpass filter, were all adjusted to approximately 13 Hz. N_2 background signal measurements were also made concurrently in both modes of operation. The P(22) CO_2 laser line was used, since it is not strongly absorbed by either C_2H_4 or NH_3, which

may have adsorbed onto the cell walls or fill lines. Table 4.3 summarizes the NH_2D signal, the N_2 background signal, and the signal-to-background ratio as a function of total pressure.

TABLE 4.3. PERFORMANCE OF THE OAD-1 CELL USING MONODEUTERATED AMMONIA IN THE CHOPPED-MODE.

Total pressure (torr)	Chopped-mode signal (mV/W)	Chopped-mode background (mV/W)	$\frac{\text{signal}}{\text{background}}$
760	924	19.1	48.4
500	529	18.1	29.2
450	445	16.9	26.3
400	362	16.5	21.9
350	287	14.2	20.2
300	208	12.3	16.9
250	144	10.6	13.6
200	93.2	8.6	10.8
150	49.8	6.9	7.22
100	22.0	4.8	4.58
50	4.67	2.6	1.80

The chopped-mode NH_2D signal increased with pressure due to pressure-broadening of the NH_2D absorption line and the 1720 MHz offset between it and the laser frequency, and due to the increase in responsivity. The background signal also increased with pressure and was slightly lower than the OAD-1 background signal shown in Figure 4.4. As before, the normalization laser power in the chopped-mode is one-half of the actual laser power. It is interesting to note that the background signal data in Table 4.3 were taken eight days after the corresponding data in Figure 4.4. During that time, the spectrophone had been removed from and reinserted into the experimental set-up. After realignment, the cell was rotated about its vertical axis (approximately 2.4°) to prevent window reflections from reentering the CO_2 laser. An iris was placed in the path of the beam prior to the spectrophone in order to block the radiation reflected from the spectrophone window. There was concern that rotating the cell in this manner would cause a greater fraction of the beam to strike the walls of the cell and therefore raise the background signal, but this did

not occur. Also, the earlier background measurements were made with the P(14) laser line while the latter measurements used the P(22) line. Since the absorptivities of C_2H_4 at these laser lines at 760 torr are 29.10 and 1.09 $atm^{-1}cm^{-1}$ [2], respectively, it is possible that a trace amount of C_2H_4 remained in the cell despite its thorough evacuation. We also see in Table 4.3 that the signal-to-background ratio increased with pressure, as observed in the chopped-mode C_2H_4 data.

4.3.2 The Stark Spectrophone Cell OAD-2

A series of measurements was next made with the smaller volume cell. The OAD-2 spectrophone cell was identical to the OAD-1 cell except that the width of the main rectangular parallepiped volume was reduced from 11.8 mm to 2 mm, the Stark electrode spacing (l_y) was slightly larger, and the Stark voltage ground connection was moved from the upper part of the stainless steel mounting fixture to the upper cylindrical Stark electrode. As before, the spectrophone was rotated approximately 2.4° about its vertical axis to prevent the reflection from its window from reentering the CO_2 laser. The other degrees of freedom of the spectrophone were carefully adjusted to minimize the chopped-mode N_2 background signal. A CdS half-wave plate was placed in the beam just prior to the spectrophone in order to allow rotation of the direction of the linearly polarized beam. For these chopped-mode measurements, the direction of the laser polarization was adjusted to be either perpendicular (horizontal) or parallel (vertical) to the direction of the Stark field in the spectrophone cell. No beam wander or power variation was detected as the half-wave plate was rotated. The modulation (chopping) frequency was adjusted to approximately 14.5 Hz in order to coincide with the modulation frequency of the Stark polarization modulation data of Chapter 6. A new gas mixture consisting of 600 torr of NH_3 and 300 torr of ND_3 was made in a thoroughly baked-out 1 liter cylinder. The spectrophone was filled with approximately 5 torr of this mixture (2.22 torr of NH_2D), brought to 200 torr with pure N_2, and then, for the 50 torr

measurements, pumped down to a total pressure of 50 torr. This resulted in a calculated 0.56 torr of NH_2D at 50 torr total pressure. The gas fill was allowed to stabilize a considerable length of time before measurements were made. Numerous checks using the chopped-mode, no Stark voltage, and vertical laser polarization, were made throughout the measurements to observe the stability of the gas fill. During one 90 minute period, a 5% decrease in the signal was observed, indicating the gas was being adsorbed onto the cell walls.

Figures 4.6 and 4.7 show the chopped-mode signals for total pressures of 50 torr and 200 torr, respectively, and for both directions of laser polarization, as the dc Stark voltage was slowly varied from 0 to 700 V at 50 torr and 0 to 1000 V at 200 torr. (All of the OAD-2 signals in this section are given in units of mV/W, and the laser power normalization is to the peak laser power, vs. the average laser power exiting the chopper, which was used for the OAD-1 data. This is to allow direct comparison of the chopped-mode signals to the Stark voltage and Stark polarization modulation signals reported in the following two chapters). From Table 3.1, we see that the predicted dc Stark voltage for coincidence between the NH_2D absorption line and the laser line is 381 and 508 V, for $|M_J| = 4$ and 3, respectively. At 50 torr, where the two lines can be resolved, the maxima of the signal do indeed occur very near these voltages. Both polarization signals also begin to increase at 650 V due to the $|M_J| = 2$ peak located at 762 V. (Of course, the absolute values of the abscissas in the figures are very sensitive to errors in the measured value of l_y, the Stark electrode separation). The predicted FWHM at 50 torr for the $|M_J| = 4$ and 3 transitions is 375 and 500 V, respectively. The widths observed in Figure 4.6 are reasonable when the theoretical widths are considered.

At 200 torr, the higher pressure allowed the dc Stark voltage to be adjusted over a larger range of 0 to 1000 V. At this higher pressure, the individual transitions seen at 50 torr were pressure-broadened into a single peak. This was reasonable

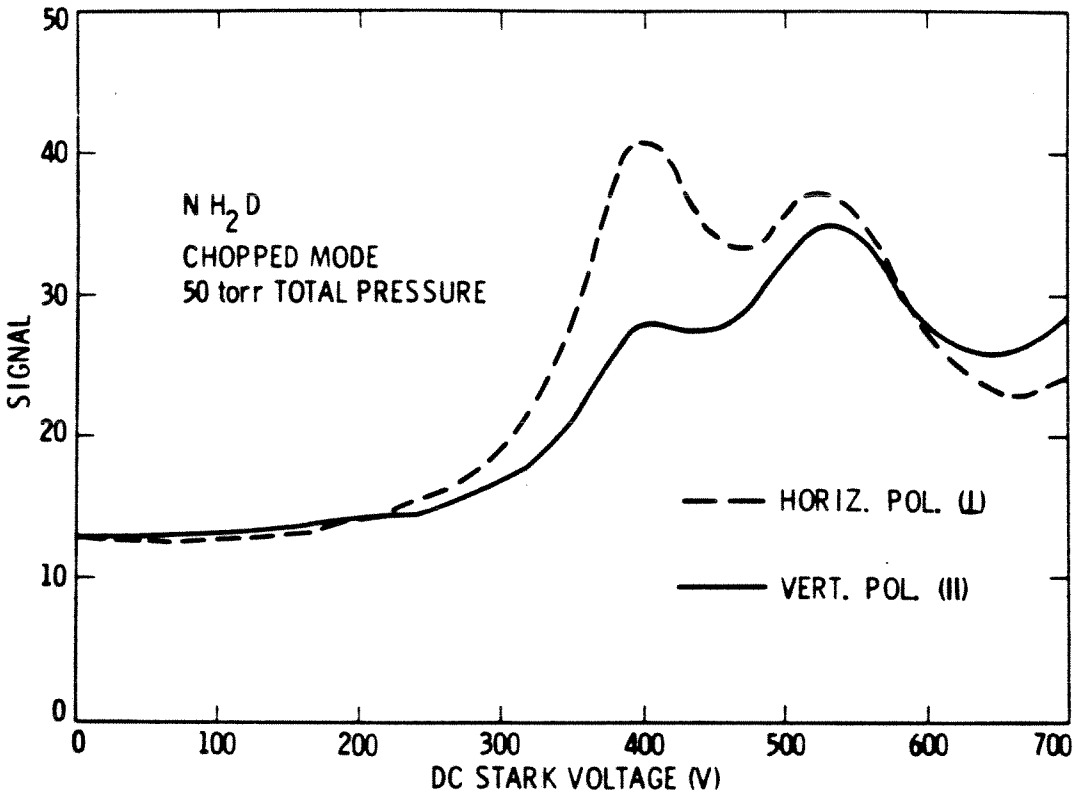

Figure 4.6. Chopped-mode OAD-2 signal in mV/W vs. the dc Stark voltage at 50 torr. Normalization was to peak laser power and the frequency was 14.5 Hz.

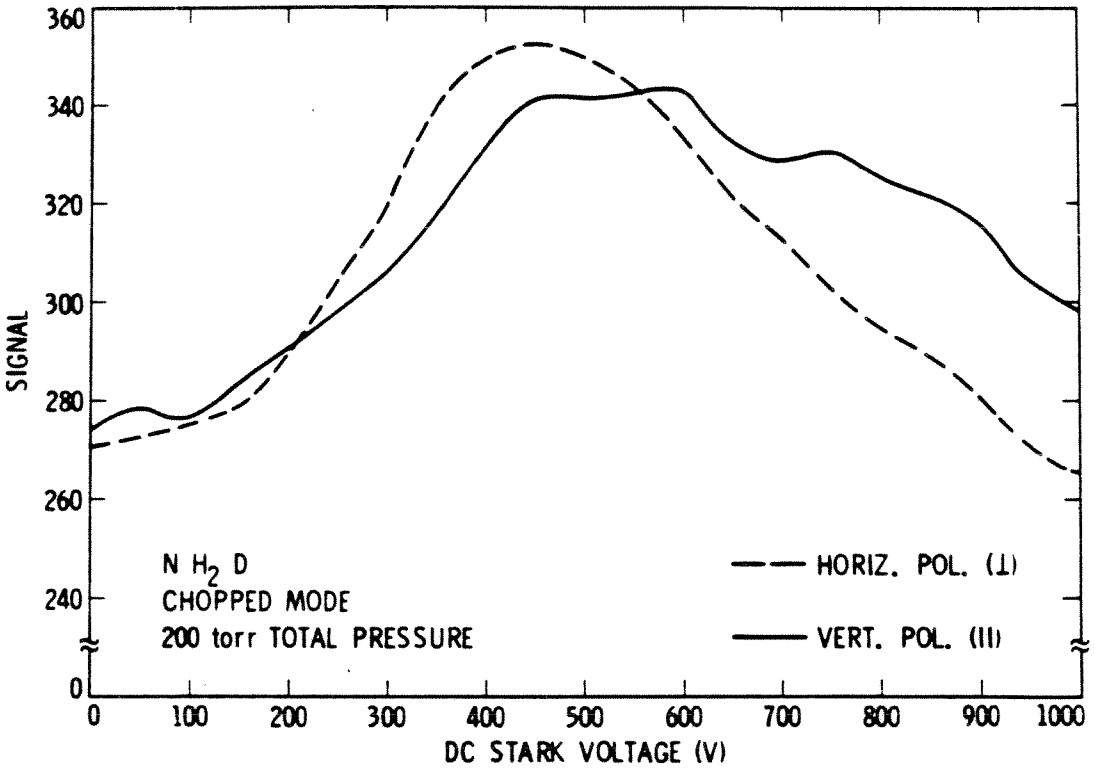

Figure 4.7. Chopped-mode OAD-2 signal in mV/W vs. the dc Stark voltage at 200 torr. Normalization was to peak laser power and the frequency was 14.5 Hz.

since the predicted FWHM at 200 torr for the $|M_J| = 4$ and 3 transitions is 1500 V and 2000 V, respectively. There is a small peak in the vertical polarization curve near 750 V, which may be due to the predicted $|M_J| = 2$ transition at 762 V. The maximum chopped-mode signal increased by about a factor of 9 due to the higher cell responsivity at 200 torr (× 2.76) and due to the approximate factor of 4 increase in the NH_2D concentration.

The background signal for the OAD-2 cell was measured using pure N_2 under the identical conditions of Figures 4.6 and 4.7. At 50 torr, the chopped-mode background signal was independent of $\bar{E}$, the dc Stark field, and was equal to 0.28 mV/W and 0.15 mV/W with vertical and horizontal polarization, respectively. (All of the chopped-mode OAD-2 background signals were also normalized to the peak laser power). The largest signal-to-background ratio was 280 at 400 V with horizontal laser polarization. The minimum detectable attenuation coefficient, defined in (4.17), was 9.95×10^{-6} cm^{-1} and 5.28×10^{-6} cm^{-1} for vertical and horizontal polarization, respectively. The dependence of the chopped-mode background signal on the direction of laser polarization could be due to either differential absorption by the ZnSe windows, or to the slight tilt of the windows, with a resulting difference in the total absorption of the laser beam by the cell walls.

At 200 torr, the background signal was again independent of $\bar{E}$ and was equal to 0.83 mV/W and 0.49 mV/W for vertical and horizontal laser polarization, respectively. The increase in the cell's responsivity at 200 torr explains the higher background signal. The largest signal-to-background ratio was 720 at 450 V with horizontal laser polarization. The minimum detectable attenuation coefficient for vertical and horizontal polarization was 1.08×10^{-5} cm^{-1} and 6.40×10^{-6} cm^{-1}, respectively.

Although the NH_2D chopped-mode OAD-2 measurements were reported here, we are primarily interested in comparing these results to the results obtained from

operating the spectrophone in the new Stark voltage modulation and Stark polarization modulation modes. This will be done in the following two chapters.

4.4 Chapter 4 References

[1] "Condenser Microphones and Microphone Preamplifiers", (May 1977), Bruel & Kjaer DK-2850 Naerum, Denmark

[2] R.R. Patty, G.M. Russworm, W.A. McClenny, and D.R. Morgan: Appl. Opt. 13(12), 2850-2854(Dec. 1974)

5. STARK VOLTAGE MODULATION

5.1 Theory

5.1.1 Introduction

In Chapter 2, an expression was derived for the microphone output voltage of a spectrophone in the conventional chopped laser radiation mode of operation. Under typical operating conditions, this expression became (2.82)

$$\tilde{v}_m = S_{oc}\tilde{p} = \frac{-v_b r_d^2}{8x_b\left[Y + \frac{(\pi r_d^2)^2 \gamma p_A (V_c + V_m)}{8\pi V_c V_m}\right]} \frac{i(\gamma-1)(\alpha l_c \tilde{W})}{\omega\left(1 + \frac{i}{\omega t_c}\right)V_c} \quad , \tag{5.1}$$

where $\tilde{W}$ is the ac component of the incident laser power at the modulation frequency ω, and α is the linear attenuation coefficient of the gas. Modulation of the incident laser power with a light chopper is the prevalent technique of signal generation in use. As stated in Chapter 2, a serious limitation in detecting small absorption strengths arises from the synchronous background signal found in all optoacoustic detectors. This synchronous background signal results from the modulation necessary to generate the desired signal. The sources of the background signal already discussed include window bulk and surface absorption, absorption at the cell walls of radiation scattered from the optical surfaces and chopper blades, absorption by aerosols in the gas, direct acoustic coupling from the chopper to the microphone, and absorbing contaminant gases present in the spectrophone. It is apparent that all of these sources of background signal are modulated by the light chopper just as the desired absorption by the gas sample is modulated. Many schemes for reducing the background signal have been proposed and some have been tried (see Chapter 1), but most of the ideas have retained the basic chopped-light mode of operation, and have concentrated on improving the geometry of the spectrophone and its illumination. These techniques have succeeded in

lowering the background signal, but not to the extent desired, so that the background signal and not noise remained the limiting factor. This chapter describes a new technique of modulation for optoacoustic detection which completely eliminates the light chopper from the experiment and which has lowered the minimum detectable attenuation coefficient by more than two orders of magnitude [1,2].

5.1.2 Signal Generation

Stark voltage modulation of the optical absorption inside the spectrophone is accomplished by the application of a time-varying electric field to the gas sample instead of chopping the laser illumination. The minimum absorption during one period of modulation in the Stark voltage modulation mode is not zero, as it is in the chopped mode; rather, the output signal is due to the change in absorption caused by the changing electric field. The conventional OAD cell is modified to include a pair of parallel metal plates that can be used to apply a large electric field to the gas. The applied electric field consists of a dc component, $\bar{E}$, and an ac component, at frequency ω, $\tilde{E}$, which causes a modulation of the linear attenuation coefficient α. The exact time dependence of $\alpha(t)$ is periodic and is determined by:

(1) The particular Stark effect of the molecule(s) being measured (e.g., the strength of the linear Stark effect);

(2) The position of the laser wavelength with respect to resonances in the molecules;

(3) The dc component of the electric field, $\bar{E}$;

(4) The amplitude of the ac component of the electric field, $\tilde{E}$;

(5) The frequency of modulation, ω;

(6) The alignment of the laser polarization with the direction of the electric field in the spectrophone.

Phase-synchronous detection is used to pick out the component of $\alpha(t)$ at frequency ω, $\tilde{\alpha}$, and thus (5.1) becomes

$$\tilde{v}_m = S_{oc}\tilde{p} = \frac{-v_b r_d^2}{8x_b\left[Y + \frac{(\pi r_d^2)^2 \gamma p_A (V_c + V_m)}{8\pi V_c V_m}\right]} \frac{i(\gamma-1)(l_c W\,\tilde{\alpha})}{\omega\left[1 + \frac{i}{\omega t_c}\right]V_c} \quad . \tag{5.2}$$

Since the laser power W is constant, the sources of background signal listed previously are eliminated. If the limiting case of very small field modulation $\tilde{E}$ is considered, the amplitude of $\tilde{\alpha}$ will be proportional to the electric field modulation amplitude $\tilde{E}$, times the slope of the α vs. $\bar{E}$ curve. (In general, this technique is referred to as derivative detection, and the proportionality of the signal to $\tilde{E}$ and $\frac{d\alpha}{d\bar{E}}$ is derived and discussed further in Appendix A). Thus the signal at ω is zero if $\bar{E}$ is adjusted so that the Stark-shifted absorption line exactly coincides with the laser line. (The lowest frequency component of $\alpha(t)$ will then be 2ω). It is desirable to slowly vary $\bar{E}$ through a range which brings the absorption line into and then out of coincidence with the laser line. The resulting plot of the Stark voltage modulation signal vs. $\bar{E}$ yields the derivative of the α vs. $\bar{E}$ curve. (In Chapter 4, we saw that the α vs. $\bar{E}$ curve can be obtained in the chopped mode by varying $\bar{E}$). A new degree of discrimination is thus possible between molecules which have overlapping absorption spectra but which exhibit different Stark modulation "signatures". Such signatures may also be used to distinguish between signals from a near-resonant weak absorption line and the far wings of a very strong absorption line.

5.1.3 Residual Background Signal

Since Stark modulation eliminates the chopper, the intensity modulation of the window absorption, aerosol absorption, contaminant absorption, light scattering, and acoustic pickup are all eliminated. However, a residual background signal

is still possible, which may be due to:

(1) Ground loop coupling between the sinusoidal current of the Stark electrodes and the microphone signal;

(2) Electrostatic forces on the microphone diaphragm from the sinusoidal Stark electric field;

(3) A pressure pulsation or vibration created by movement of the electrodes due to the modulated electrostatic force between them;

(4) A Stark-modulated absorption in the contaminating gases.

We will now discuss these possible sources of the residual background of the Stark voltage modulation mode and their expected magnitudes. The output voltage of the Burleigh PZ-70 high-voltage operational amplifier, which supplied the Stark voltage, was limited to a range of 0 to 1000 V. Since $\tilde{v}_s \leq \bar{v}_s$, we will use $\tilde{v}_s = \bar{v}_s = 500$ V as "worst case" values in the following residual background signal calculations, although our actual experimental values were smaller. Also, we will arbitrarily compare each source of background signal to 1μV, which was the upper limit on the background signal established in our later experiments.

Ground Loop Coupling

The first possible source of Stark mode background signal is coupling between the current going to the Stark electrodes and the microphone signal. The capacitance of the closely spaced Stark electrodes is given by

$$C_{OAD} = \frac{\varepsilon_0 \varepsilon_r A_e}{l_y} \quad , \tag{5.3}$$

where ε_0 is the permittivity of free space, ε_r is the relative permittivity of the medium between the electrodes, A_e is the area of each electrode, and l_y is their

separation. The Stark spectrophone electrodes (OAD-2) had a separation of $l_y = 1.07 \times 10^{-3}$ m, a length of 2×10^{-2} m, and a width of 1.59×10^{-2} m yielding $A_e = 3.18 \times 10^{-4}\ m^2$. The medium between the electrodes consisted of the gas mixture ($\varepsilon_r \approx 1$), glass spacers ($\varepsilon_r \approx 5$), and a small amount of epoxy. The measured value of C_{OAD} was 17.7 pF (9.9 pF for the OAD-1 cell) using a capacitance meter, yielding

$$\varepsilon_r = 6.7 \quad . \tag{5.4}$$

The magnitude of the current going to the electrodes is given by

$$|\tilde{J}| = \omega C_{OAD} |\tilde{v}_s| \quad , \tag{5.5}$$

where $|\tilde{v}_s|$ is the ac Stark voltage applied to the electrodes.

Letting f = 13 Hz, and $\tilde{v}_s$ = 500 V,we see that

$$|\tilde{J}| = 7.2 \times 10^{-7}\ A \quad . \tag{5.6}$$

This current could cause a background signal voltage if its path shared an impedance Z with the path of the signal current. Dividing the 1 μV reference background signal by (5.6) results in

$$Z = 1.4\ \Omega \quad . \tag{5.7}$$

If Z were purely capacitive, the capacitance at 13 Hz would be

$$C = 8850\ \mu F \quad . \tag{5.8}$$

Refering to Figure 3.3, we see the relative positions of the Stark spectrophone, the microphone, and the electrical connections. The electrical connection directly on the upper Stark electrode for application of the Stark voltage was a feature only on the OAD-2 cell. For the original cell (OAD-1), this connection was made at the side of the mounting fixture at approximately the same level as the microphone diaphragm. In addition, the mounting fixture was earth-grounded through the optical rail, post, and optical table on which it was mounted. Thus the Stark current entering the lower Stark electrode could return to earth ground (the grounded side of the Burleigh PZ-70 op-amp) three different ways:

(1) Through the Burleigh negative output lead connected to the side of the mounting fixture (or to the upper Stark electrode);

(2) Through the mounting fixture, mounting post, and optical table;

(3) Through the signal ground lead connecting the microphone to the preamplifier.

Resistance in the third path could cause a false microphone signal. Thus care should be taken to eliminate ground loops and ensure good electrical connections.

Electrostatic Force on the Microphone Diaphragm

A second possible source of residual background signal is coupling between the large sinusoidal Stark electric field and the microphone diaphragm. A pictorial drawing of the geometry of our Stark spectrophone is shown in Figure 3.3. The microphone, described in Chapter 2, is held in a grounded metal fixture such that its body, and therefore its diaphragm, is electrically connected to the fixture, which is also connected to the upper Stark electrode. The Stark voltage, v_s, is applied to the lower electrode, which, together with the upper electrode, end windows, and glass spacers, form the spectrophone. Two small passages in the mounting fixture, each at 30° from vertical, join to allow acoustic communication between the

spectrophone and the microphone through a dog-leg channel. If an electric field, E, caused by the Stark voltage, v_s, exists near the microphone diaphragm, it will result in a force per unit area on the diaphragm given by

$$p = \frac{F}{A} = \varepsilon E^2 \quad , \tag{5.9}$$

which would deflect the diaphragm and produce a false pressure signal.

It would be quite difficult to analyze the electric field penetration through the dog-leg channel. However, an upper limit for this source of background signal may be found by considering a "straightened out" cylindrical passage of length L and radius a as shown in Figure 5.1. The wall and upper end of the cylinder are grounded and the lower end of the cylinder is closed with a disk at voltage v_s. Solving Laplace's equation in cylindrical coordinates, the potential inside the passage is

$$v(r, z) = \sum_m \frac{2v_s J_0(k_m r)\sinh[k_m(L-z)]}{(k_m a)J_1(k_m a)\sinh(k_m L)} \quad , \tag{5.10}$$

where

$$J_0(k_m a) = 0 \quad , \tag{5.11}$$

and thus

$$k_m a \approx 2.4 \, , \; 5.5 \, , \; 8.7 \, , \; 11.8 \, , \; \cdots \quad . \tag{5.12}$$

We are only interested in the electric field near z = L, since the upper end of the cylinder represents the microphone diaphragm. Using $\vec{E} = -\nabla v$,

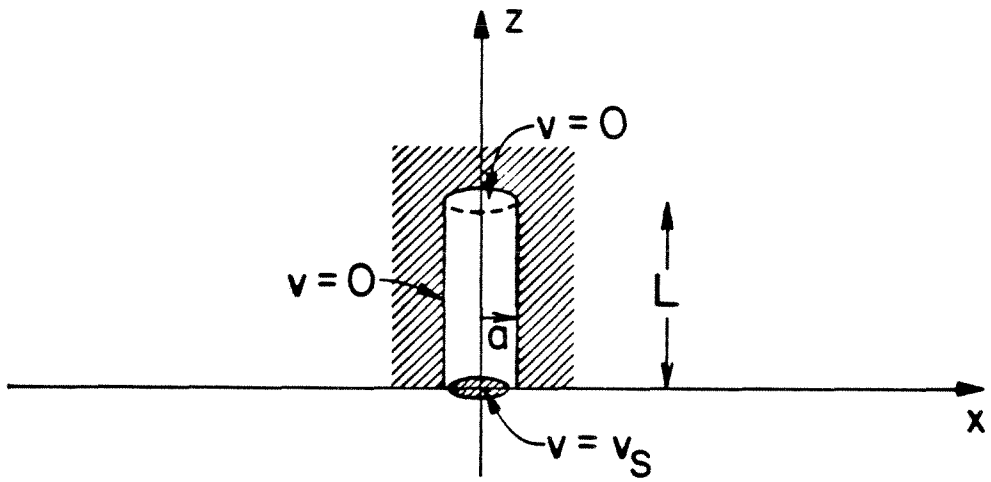

Figure 5.1. Simplified geometry representing the direct interaction of the Stark field with the microphone diaphragm.

$$E(r, L) = E_z(r, L) = \sum_m \frac{2v_s J_0(k_m r)}{aJ_1(k_m a)\sinh(k_m L)} \tag{5.13}$$

Expressing the hyperbolic sine in terms of exponentials,

$$\sinh(k_m L) = \frac{1}{2}\left[e^{k_m L} - e^{-k_m L}\right] \tag{5.14}$$

and letting $L >> a$, we have

$$E_z(r, L) \approx \frac{4v_s J_0(k_1 r)}{aJ_1(k_1 a)} \exp\{-k_1 L\} \tag{5.15}$$

The square of the electric field, E_z, averaged over the end of the cylinder is

$$< E_z^2(r, L) > = \frac{16 v_s^2}{a^2} \exp\left\{-4.8 \frac{L}{a}\right\} \tag{5.16}$$

If we express $v_s(t)$ as

$$v_s(t) = \overline{v_s} + \tilde{v_s} \cos\omega t \tag{5.17}$$

then

$$v_s^2 = \left(\overline{v_s}\right)^2 + 2\overline{v_s}\tilde{v_s} \cos\omega t + \left(\tilde{v_s}\right)^2 \cos^2\omega t \tag{5.18}$$

and the synchronously detected component at ω will be $2\overline{v_s}\tilde{v_s}$.

Combining (5.9) and (5.18), using the values of our spectrophone: $L \approx 2.54 \times 10^{-2}$ m and $a \approx 7.5 \times 10^{-4}$ m, and assuming a worst case of $\overline{v_s} = \tilde{v_s} = 500$ V, the resulting equivalent pressure is

$$|\tilde{p}| = \varepsilon < E_z^2(r, L) > = 3.6 \times 10^{-58} \text{ Pa} \tag{5.19}$$

Thus the background signal due to this effect is very small.

Electrostatic Force on the Stark Electrodes

A third possibility for a residual background signal is an electrostatic "loudspeaker" action of the Stark electrodes. Vibration of the Stark electrodes could produce a false signal by:

(1) Creating a synchronous pressure signal due to the changing cell volume;

(2) Directly vibrating the microphone diaphragm.

The attractive force between the Stark electrodes is given by

$$F = \frac{C_{OAD}^2 v_s^2}{2\varepsilon_0 \varepsilon_r A_e} \quad . \tag{5.20}$$

The ω component of v_s^2 is again given by $2\overline{v_s}\tilde{v_s}$. Assuming that $\overline{v_s}$ = 500 V, $\tilde{v_s}$ = 500 V, and C_{OAD} = 17.7 pF, the peak-to-peak force at frequency ω is 4.15×10^{-3} N. This force will slightly compress the glass spacers which separate the two Stark electrodes. We will neglect the epoxy in the cell and assume that Young's modulus for our glass spacers is 6×10^{10} Nm^{-2}, the value for fused silica, where Young's modulus, E_Y, is defined as

$$E_Y \triangleq \frac{\text{Force/Area}}{\Delta l_y / l_y} \quad . \tag{5.21}$$

The area in (5.21) is the area of contact between the Stark electrodes and the glass spacers, A_g, which is 2.78×10^{-4} m^2 for the OAD-2 cell. Inserting our values into

(5.21), we obtain

$$\frac{\Delta l_y}{l_y} = 2.5 \times 10^{-10} \tag{5.22}$$

and

$$\Delta l_y = 2.7 \times 10^{-13}\ \text{m} \tag{5.23}$$

We will now compute the expected pressure signal due to the electrode vibration. If we assume that the length and width of the cell do not change, then the percentage volume change of the rectangular parallelpiped part of the cell will equal that of l_y. Using the spectrophone volumes listed in Table 4.1, we find that

$$\left|\frac{\Delta V_c}{V_c}\right| = \left|\frac{\Delta p_A}{p_A}\right| = 7.8 \times 10^{-11} \quad . \tag{5.24}$$

Since S_{mp}, the coupled microphone-preamplifier sensitivity, is 39.9 mV/Pa, and if we assume a worst case of p_A = 760 torr = 1.01×10^5 Pa, then the rms background signal will be 0.11 μV. This source of background signal is proportional to the total pressure.

A second possible effect of the vibrating Stark electrodes is direct vibration of the microphone diaphragm. In Chapter 2, we saw that the output voltage of the microphone is given by

$$\tilde{v}_m = -\frac{v_b}{x_b}\tilde{x} \quad , \tag{5.25}$$

where v_b is the microphone bias voltage (200 V), x_b is the biased diaphragm-backplate separation (20 μm), and $\tilde{x}$ is the average displacement of the diaphragm

from equilibrium. Combining (5.23) and (5.25), and assuming that the diaphragm and Stark electrode vibrate with the same amplitude (worst case), we obtain an rms background signal voltage of 0.95 μV. This result is larger than the previous result, and close to our 1μV reference level, but it must be remembered that "worst case" values were used. This source of background signal will depend on the total pressure through the pressure dependence of the diaphragm motion.

The last two sources of background signal were shown to produce small effects. However, if the vibration frequency of the Stark electrode was close to the natural resonance frequency of the cell, an amplification of the effects would occur. We will now compute the resonance frequency of the Stark-electrode vibration in order to see how close it was to our modulation frequency of 13 Hz. If a mass M is suspended by a spring with tension Y_s, the resonant frequency with no losses is

$$f = \frac{1}{2\pi}\left[\frac{Y_s}{M}\right]^{\frac{1}{2}} \quad . \tag{5.26}$$

The approximate mass of one Stark electrode is derived from its volume ($\approx 2 \times 10^{-6}\ m^3$) and the density of stainless steel ($7.5 \times 10^3\ kg\ m^{-3}$), and is 1.5×10^{-2} kg. Using (5.21), we estimate the spring tension Y_s to be

$$|Y_s| = \frac{F}{\Delta l_y} = \frac{A_g E_Y}{l_y} = 1.56 \times 10^{10}\ Nm^{-1} \quad . \tag{5.27}$$

Combining (5.26), (5.27), and the value for M, we find

$$f \approx 162\ kHz \quad . \tag{5.28}$$

At modulation frequencies near 13 Hz, we need not be concerned about resonance enhanced electrode vibration.

5.2 Experimental Results

5.2.1 The Stark Spectrophone Cell OAD-1

Stark voltage modulation was first accomplished using the OAD-1, the P(20) line of the 10.6 μm band of the CO_2 laser, and NH_2D. The gas mixture was the same as described in the OAD-1 NH_2D chopped-mode section (4.3.1) and the data in both modes were taken concurrently as the total pressure was lowered in discrete steps. Conversion from the chopped-mode to the Stark voltage modulation mode consisted of (see Figure 3.1):

(1) Removing the mechanical chopper;

(2) Changing the PAR lock-in amplifier setting from external synchronization to internal synchronization;

(3) Amplifying the internal oscillator output of the lock-in amplifier and adding it to the dc Stark voltage applied to the Stark electrodes.

The mechanical chopper, and the lock-in amplifier's internal oscillator and input bandpass filter, were all adjusted to approximately 13 Hz. For these Stark voltage modulation measurements, we chose a Stark voltage of 200 V peak-to-peak centered at 150 V. (These measurements were made prior to the OAD-2 measurements of Figures 4.6 and 4.7. Consequently, the dc and ac Stark voltage values that would give the largest signal were unknown. Also, the breakdown voltage of the cell had not yet been measured and, therefore, high Stark voltages were avoided). This corresponded to an $\bar{E}$ and $\tilde{E}$ of 1.44×10^5 V/m and 1.92×10^5 V/m peak-to-peak, respectively. From (3.7), we see that the frequency offset between the laser line and the NH_2D $|M_J| = 4$ absorption line center was modulated by 1100 MHz centered at 1220 MHz. No half-wave plate was used here and thus the laser polarization and the Stark electric field were both aligned vertically. Table 5.1 presents the resulting Stark voltage modulation signals and also repeats the corresponding chopped-mode

TABLE 5.1. COMPARISON OF THE OAD-1 STARK VOLTAGE MODULATION AND CHOPPED-MODE SIGNAL.

Total pressure (torr)	Chopped-mode signal (mV/W)	Stark voltage modulation signal (mV)	(mV/W)
760	924	0.160	0.390
500	529	0.706	1.810
450	445	0.842	2.360
400	362	1.000	2.860
350	287	1.400	3.160
300	208	1.500	3.450
250	144	1.450	3.400
200	93.2	1.200	2.810
150	49.8	0.880	2.020
100	22.0	0.411	0.944
50	4.67	0.105	0.239

signal of Table 4.3. Recall that the chopped-mode measurements were made with no dc Stark voltage. The Stark voltage modulation signal is given both with and without normalization to the laser power for comparison with the chopped-mode and Stark voltage modulation background signals. It is maximum at 300 torr due to the particular values of $\bar{E}$ and $\tilde{E}$ (the HWHM of NH_2D at 300 torr is 6030 MHz), and the dependence of the responsivity on pressure. Since the normalization laser power in the chopped-mode is one-half of the actual laser power, the chopped-mode signal, in mV/W, must be divided by 2 in order to compare it to the Stark voltage modulation signal, in mV/W, for a given available laser power.

N_2 background signal measurements were also made concurrently in both modes of operation. Table 5.2 lists the results for the Stark voltage modulation mode as well as repeating the corresponding chopped-mode results of Table 4.3. The P(22) CO_2 laser line was used, since it is not strongly absorbed by either C_2H_4 or NH_3, which may have adsorbed onto the cell walls or fill lines. The Stark voltage modulation background signal was observed to be independent of the laser power, so it was not normalized to the laser power. It was also independent of the total pressure with a mean value of 13.8 μV and a standard deviation of 0.82 μV. Table 5.2 also lists the signal-to-background ratios of each mode. The 13.8 μV mean value was used for

TABLE 5.2. COMPARISON OF THE OAD-1 STARK VOLTAGE MODULATION AND CHOPPED MODE BACKGROUND SIGNALS AND SIGNAL-TO-BACKGROUND RATIOS.

Total pressure (torr)	Chopped-mode background (mV/W)	Stark background (μV)	$\frac{\text{signal}}{\text{background}}$ Chopped	$\frac{\text{signal}}{\text{background}}$ Stark
760	19.1	14.6	48.4	11.6
500	18.1	14.6	29.2	51.2
450	16.9	12.2	26.3	61.0
400	16.5	14.4	21.9	72.5
350	14.2	13.8	20.2	101
300	12.3	12.8	16.9	109
250	10.6	12.9	13.6	105
200	8.6	14.7	10.8	87.0
150	6.9	14.0	7.22	63.8
100	4.8	13.7	4.58	29.8
50	2.6	13.5	1.80	7.61

the Stark background signal, rather than the values listed. The Stark voltage modulation mode offers a significant improvement in signal-to-background ratio over the chopped-mode except at 760 torr. The Stark voltage modulation signal-to-background ratio is maximum at 300 torr, and the improvement over the chopped-mode is maximum at 150 torr where it is higher by a factor of 8.8. Since the Stark voltage modulation background signal is independent of laser power, any increase in laser power over our typical value of 0.5 W, would increase its signal-to-background ratio even further. Also, the values of $\bar{E}$ and $\tilde{E}$ could be chosen to maximize performance (as will be shown later). This would correspond to the position of maximum slope of the α vs. $\bar{E}$ curve. Using the OAD-1 responsivity at 400 torr, and an incident laser power of 1 W, the 13.8 μV mean background signal corresponds to a minimum measurable change in attenuation coefficient, $\tilde{\alpha}$, of 5.2×10^{-8} cm^{-1}. Assuming the background signal could be subtracted from the actual signal, the fluctuation in the background signal, 0.82 μV, corresponds to a minimum $\tilde{\alpha}$ of 3.1×10^{-9} cm^{-1}.

The N_2 background signal in the Stark voltage modulation mode increased with $\tilde{E}$. Since it was independent of laser power and total pressure, the possibility of Stark-modulated absorption by contaminating gases was eliminated. The pressure

independence also rules out a pressure signal from vibrating Stark electrodes. We have shown earlier that direct electrostatic forces on the microphone diaphragm are very small. It appeared that the Stark voltage modulation background signal was due to coupling between the displacement current of the electrodes and the microphone signal. Referring to Figure 3.3, the ground connection of the high-voltage operational amplifier, which supplied the Stark voltage, was to the upper portion of the metal mounting fixture, near the vicinity of the microphone. Later, for the OAD-2 measurements, this ground connection was moved to the upper cylindrical half of the spectrophone. The background signal was then observed to be much lower than 13.8 μV. In fact, it was below 1μV, the lowest upper limit that we could determine due to noise affecting the lock-in amplifier. However, moving the Stark voltage connection back to the original location did not affect the background signal. In retrospect, we feel that the 13.8 μV signal was not a genuine background signal, but rather was the result of ground-loops or 60 Hz line pick-up.

5.2.2 The Stark Spectrophone Cell OAD-2

A series of measurements were next made with the smaller volume cell. The gas mixture was the same as described in the OAD-2 NH_2D chopped-mode section (4.3.2). Figure 5.2 shows the Stark voltage modulation signals for both directions of laser polarization, as the dc Stark voltage was slowly varied from 0 to 700 V at 50 torr. The frequency of modulation was approximately 14.5 Hz, which was chosen to coincide with the modulation frequency of the Stark polarization modulation data of the next chapter. The ac voltage in the Stark-mode was 10 V peak-to-peak corresponding to an $\tilde{E}$ of 9.37×10^3 V/m peak-to-peak and thus a 53.6 and 40.2 MHz peak-to-peak modulation of the NH_2D $|M_J| = 4$ and 3 transitions, respectively. From Table 3.1, we see that the predicted dc Stark voltages for coincidence between the NH_2D transitions and the laser line are 381 and 508 V for $|M_J| = 4$ and 3, respectively. It was stated that the Stark voltage modulation signal should be proportional

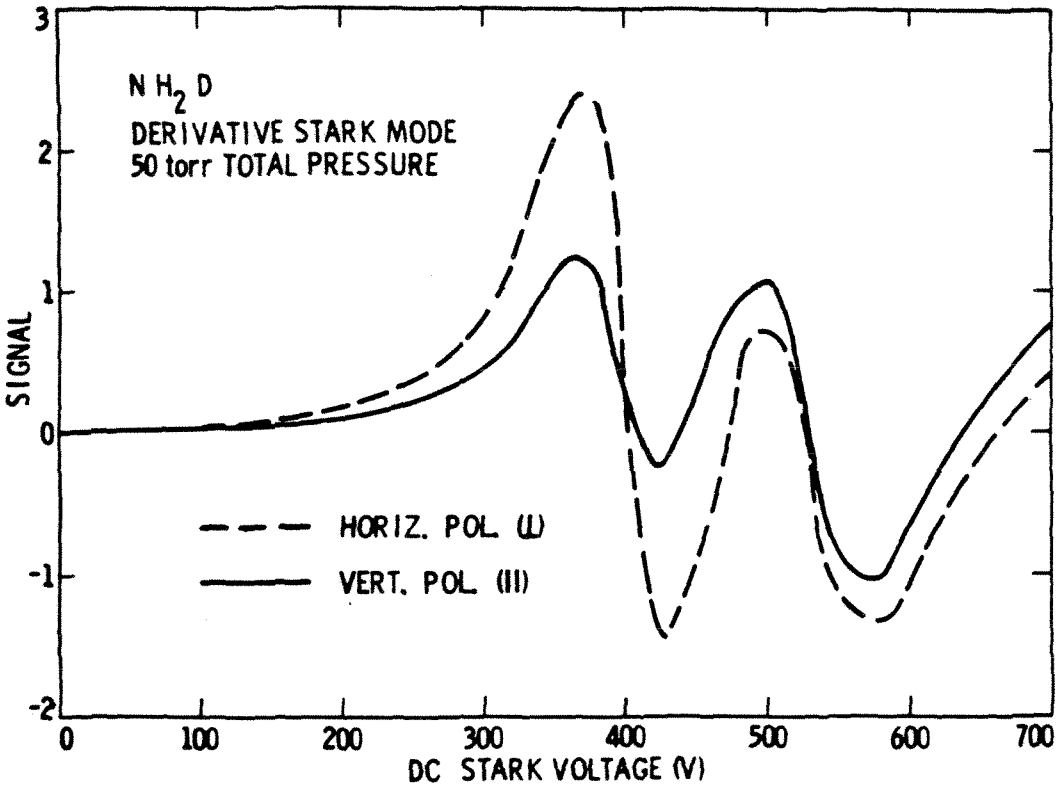

Figure 5.2. Stark voltage modulation OAD-2 signal in mV/W vs. the dc Stark voltage at 50 torr. The ac Stark voltage was 10 V peak-to-peak at 14.5 Hz.

to the first derivative of the α vs. $\bar{E}$ curve. By comparing Figures 4.6 and 5.2, we see that this is indeed the case. The Stark voltage modulation signal is maximum at points of maximum slope of the chopped-mode signal, and is zero at points of zero slope. Note that zero-crossings do indeed occur near 381 and 508 V. It is also apparent that the 150 V operating point for the OAD-1 Stark voltage modulation data was not optimum. This can be seen by comparing the greater than 2 mV/W signal near 375 V in Figure 5.2 to the 0.239 mV/W signal at 50 torr in Table 5.1, which was obtained with a much greater ac Stark voltage of 200 V. The Stark voltage modulation signal may be increased even further by increasing the ac Stark voltage, at the expense of lost resolution in the $\bar{E}$ coordinate (see Appendix A).

The background signal for the OAD-2 cell was measured using pure N_2 under the identical conditions of Figure 5.2. At 10 V peak-to-peak of ac Stark voltage, we were unable to measure a coherent background signal. Noise limited the operation of the lock-in amplifier at higher sensitivities, causing a 5-8 μV fluctuation of the readings. We were able to establish a 1 μV upper limit on the background signal. By increasing the ac Stark voltage to 500 V, centered at 300 V, a 1.7 μV background signal was observed. Assuming a linear relationship, the corresponding background signal at 10 V would be only 34 nV. It was independent of the dc Stark voltage, the total pressure, the direction of the laser polarization, and the laser power. This represents a considerable improvement over the OAD-1 performance. Even if we assume that the Stark voltage modulation background signal was 1 μV, the signal-to-background ratio was 2600 at 375 V with horizontal polarization, and the product of the minimum detectable change in attenuation coefficient, $\tilde{\alpha}$, and the laser power, was 3.59×10^{-8} cm^{-1}W. In section 4.3.2, we saw that the maximum chopped-mode signal-to-background ratio at 50 torr was 280, and that the minimum $\tilde{\alpha}$ was 5.28×10^{-6} cm^{-1}. Thus the improvement over the chopped-mode performance is almost an order of magnitude for the signal-to-background ratio, and over two

orders of magnitude for $\tilde{\alpha}$ with 1 W of laser power.

The improvement in performance of the Stark voltage modulation technique over conventional chopped laser radiation would be even larger than the measured two orders of magnitude if

(1) more laser power were available, and

(2) if the actual residual background signal and the fundamental noise, which are probably much lower than 1 μV, were the limiting factor, rather than non-fundamental noise.

This technique of operating a spectrophone is very attractive as a method of detecting extremely small concentrations of an absorbing gas with excellent discrimination against interfering contaminant gases.

5.3 Chapter 5 References

[1] M.J. Kavaya, J.S. Margolis, and M.S. Shumate: Applied Optics 18(15), 2602-2606 (August 1979)

[2] M.J. Kavaya, J.S. Margolis, and M.S. Shumate: "Optoacoustic Detection Using Stark Modulation", paper presented at the OSA topical conference on Photoacoustic Spectroscopy in Ames, Iowa on August 1, 1979

6. STARK POLARIZATION MODULATION

6.1 Theory

6.1.1 Introduction

In Chapter 5, we saw that the novel technique of modulating the absorption in a spectrophone with an ac Stark electric field was highly successful in lowering the background signal, increasing the signal-to-background ratio, and improving the minimum detectable absorption. This success was primarily due to the elimination of the mechanical light chopper and the many sources of background signal that it caused. In this chapter, the first use of a second novel modulation technique for optoacoustic detection, that of rotating the direction of the laser polarization, is reported [1,2].

6.1.2 Signal Generation

The concept of Stark polarization modulation is a natural extension of Stark voltage modulation in that no light chopper is used, the incident laser intensity is constant, and the Stark effect of the absorbing molecule is utilized. However, in the Stark voltage modulation mode, the direction of the laser polarization was constant, and a modulation of the Stark electric field was employed to modulate the gas absorption. We have shown that the modulated electric field may cause a residual background signal. The Stark polarization modulation mode differs in that the Stark electric field is constant, and the direction of the laser polarization is rotated continuously with a half-wave plate. Figure 6.1 depicts this mode of modulation. Note that the direction of polarization rotates at twice the rotation frequency of the half-wave plate, and that the absorption in the gas is modulated at four times the rotation frequency of the half-wave plate. This occurs since only the direction of the polarization, and not its sign, determines the absorption by the gas. The magnitude of the spectrophone signal will be proportional to the difference in the linear

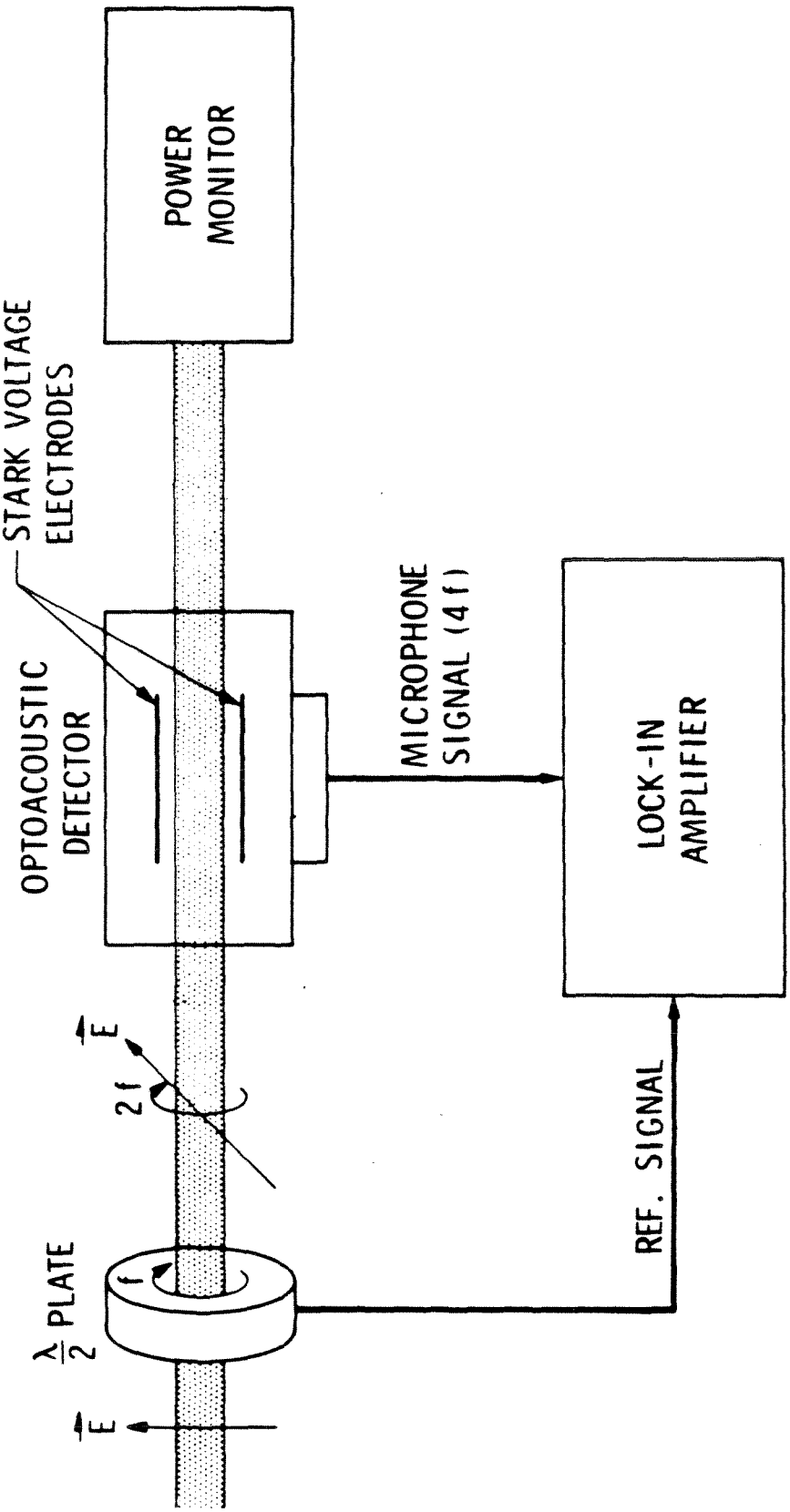

Figure 6.1. Pictorial representation of the Stark polarization modulation mode of optoacoustic detection.

attenuation coefficient, α, when measured with the laser polarization first parallel and then perpendicular to the Stark electric field. Referring to Figure 4.6, it is seen that this difference in α is a function of the dc Stark voltage, and, of course, the absorbing molecule, the laser frequency, and the total pressure. The microphone output voltage will again be given by

$$\tilde{v}_m = S_{oc}\tilde{p} = \frac{-v_b r_d^2}{8x_b\left[Y + \frac{(\pi r_d^2)^2 \gamma p_A (V_c + V_m)}{8\pi V_c V_m}\right]} \frac{i(\gamma-1)(l_c W\tilde{\alpha})}{\omega\left[1 + \frac{i}{\omega t_c}\right]V_c} , \qquad (6.1)$$

where $\tilde{\alpha}$ in this mode is interpreted as the vector difference between the attenuation coefficient for parallel and perpendicular laser polarization, corresponding to the curves of Figure 4.6, for example.

6.1.3 Residual Background Signal

Since Stark polarization modulation also eliminates the mechanical light chopper, the sources of background signal due to the chopper are eliminated. In addition, the sources of background signal due to the ac Stark voltage in the Stark voltage modulation mode, as discussed in Chapter 5, are also eliminated. Some possible sources of a residual background signal in this mode include:

(1) Beam wander due to misalignment or a wedge angle in the half-wave plate which causes the window absorption and/or the radiation which strikes the walls to be modulated;

(2) Acoustic pickup from the half-wave plate rotation mechanism to the microphone;

(3) Intensity modulation of the laser beam by an imperfect waveplate;

(4) Polarization dependent absorption by the windows;

(5) A polarization dependent beam path inside the spectrophone causing the total window and/or wall absorption to be modulated.

The first three sources of background signal would be at the fundamental rotation frequency of the half-wave plate, f, and would be discriminated against by synchronous detection at 4f. Of course, higher harmonics may exist, especially from the half-wave plate rotation mechanism. Measurements also showed that rotating the half-wave plate did not affect the beam intensity. Polarization dependent absorption by the ZnSe windows is conceivable, if the windows experienced strain as they were epoxied to the spectrophone. The fifth source of residual background signal should be small, since the parallel and perpendicular amplitude reflection coefficents for ZnSe at a 2.4° angle of incidence differ by only about 0.1%.

6.2 New Apparatus

As shown in Figure 6.1, the new apparatus required for this mode of modulation consisted of a half-wave plate and the ability to uniformly rotate it. The CdS half-wave plate was described in Chapter 3. A sturdy 2024 Aluminum mount was fabricated which held two close tolerance pre-loaded Fafnir M9307K bearings. An assembly held the half-wave plate and a pulley to the inside race of the bearings. A 1/8 inch diameter o-ring was used to drive the pulley with a 72 RPM Superior Electric SLO-SYN SS250 synchronous/stepping motor. The rotation rate of the half-wave plate was approximately 3.63 Hz resulting in a spectrophone signal at 14.5 Hz. Reflective tape was applied to two opposite quadrants of the half-wave plate pulley, and a Monsanto MCA7 reflective sensor was employed to generate a 7.25 Hz sync signal for the lock-in amplifier. The lock-in amplifier was used in the "2f" detection mode for the polarization rotation measurements, which resulted in detection at 14.5 Hz.

6.3 Experimental Results

Figures 6.2 and 6.3 show the OAD-2 signal in mV/W in the Stark polarization modulation mode at 50 and 200 torr total pressure, respectively. The dc Stark voltage was varied from 0 to 700 V at 50 torr and from 0 to 1000 V at 200 torr. The data were taken with the same gas fill and within a few minutes of the chopped-mode data of Figures 4.6 and 4.7. Comparing Figures 6.2 and 4.6 and Figures 6.3 and 4.7, we see that the signal magnitude in the Stark polarization modulation mode is proportional to the difference between the horizontal and vertical polarization chopped-mode signals, and that the Stark polarization modulation signal changes sign when the two chopped-mode curves cross each other. The maximum signal in Figure 6.2 occurs at 400 V, which is where the separation of the curves in Figure 4.6 is the greatest. The signal in Figure 6.2 is zero at approximately the same voltages where the two curves in Figure 4.6 are equal. The largest polarization modulation signal is about 6 times greater than the largest Stark voltage modulation signal, and about 3 times smaller than the largest chopped-mode signal. As in the Stark voltage modulation, a unique signature of the absorbing molecule is obtained which is useful in discriminating against interfering molecules.

At 200 torr, the maximum Stark polarization modulation signal near 400 V dc increased by about a factor of 2 over the 50 torr maximum. It was shown that the corresponding increase in the maximum chopped-mode signal was a factor of 9. Apart from the mutual increase in the cell responsivity (×2.76), this difference between the modes is due to pressure-broadening at 200 torr, causing the peak absorption to increase by a greater factor than the absorption difference between the two directions of polarization increases. In addition, the distinctiveness of the polarization modulation signature is decreased at the higher pressure. Thus the Stark polarization modulation mode is better suited to lower pressures. These same comments apply to the Stark voltage modulation mode. However, a lower limit on

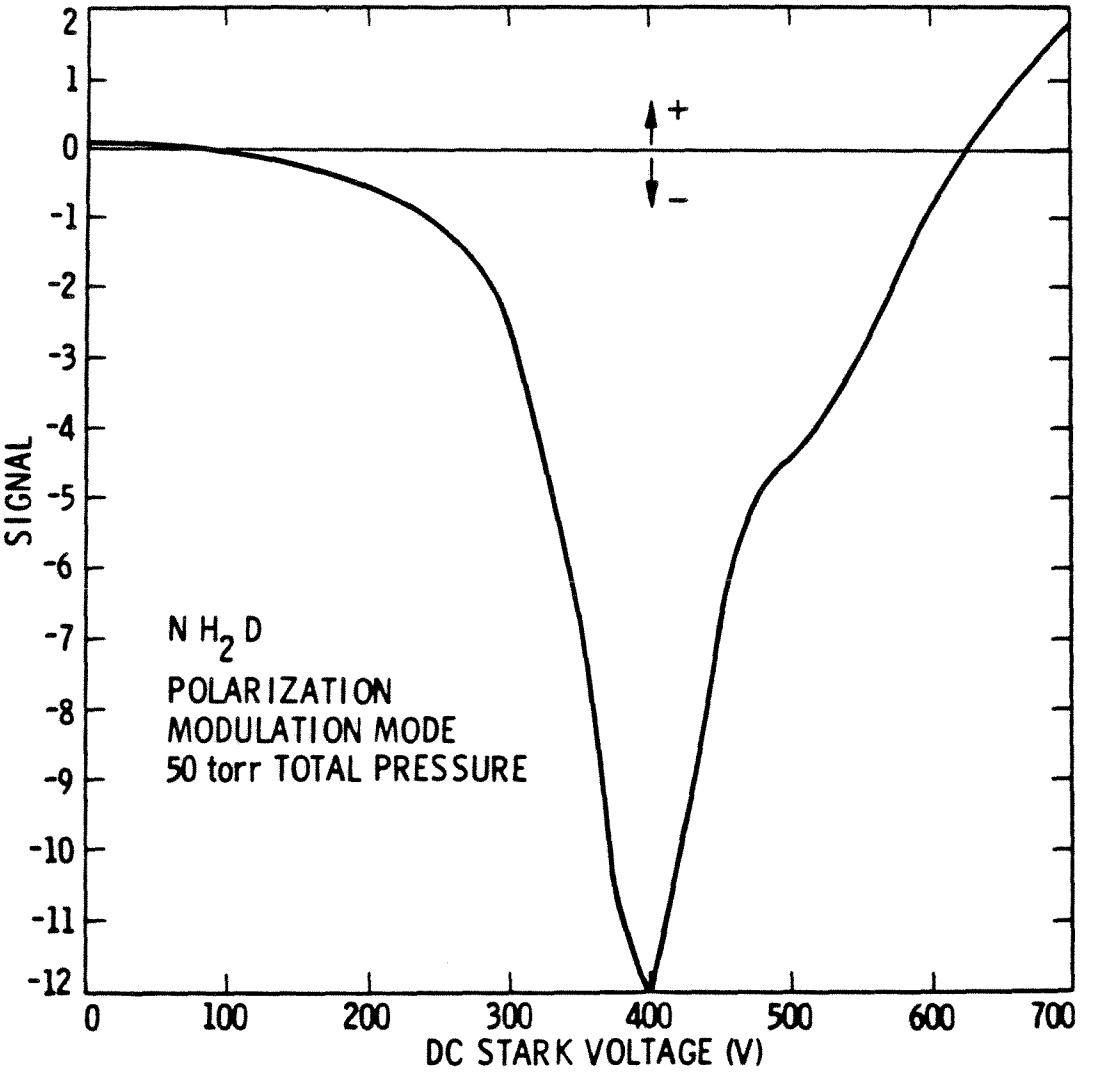

Figure 6.2. Stark polarization modulation OAD-2 signal in mV/W vs. the dc Stark voltage at 50 torr. The detected signal was at 14.5 Hz.

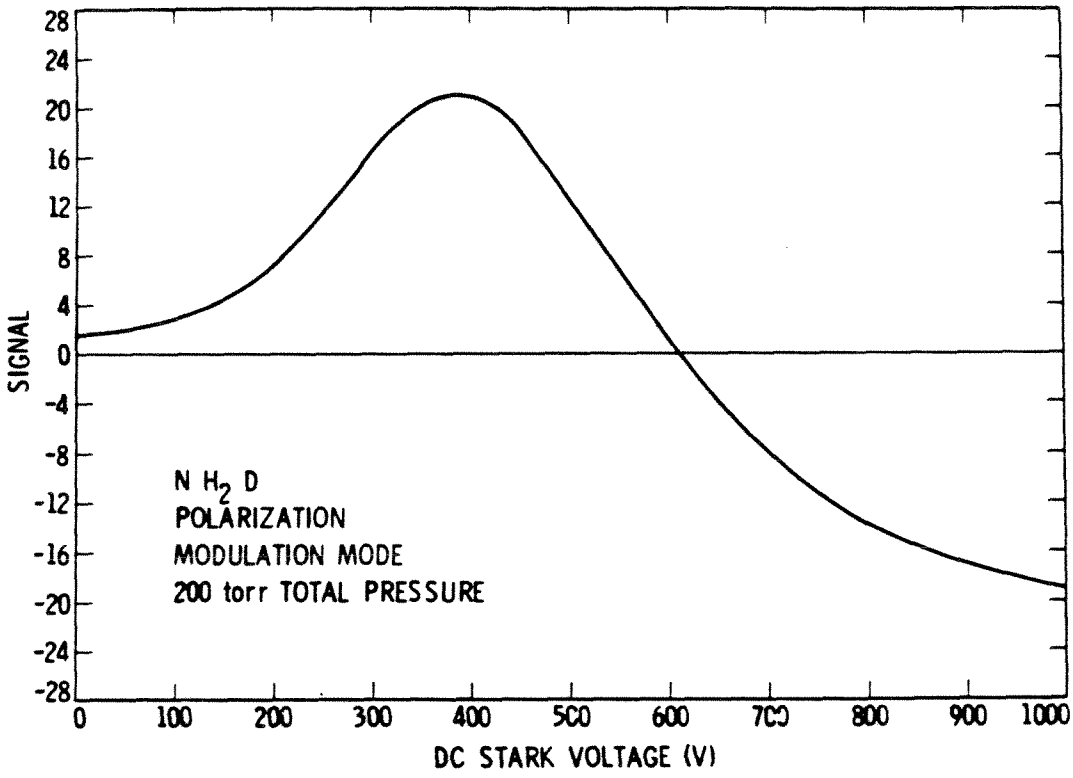

Figure 6.3. Stark polarization modulation OAD-2 signal in mV/W vs. the dc Stark voltage at 200 torr. The detected signal was at 14.5 Hz.

the pressure is established by the electrical breakdown between the Stark electrodes and the decreasing cell responsivity. The particular polarity of Figures 6.2 and 6.3 is due to the phase setting of the lock-in amplifier. From (6.1), we see that the optimum phase setting changes whenever the modulation frequency or total pressure is changed. This is also true if the source of the reference signal for the lock-in amplifier is changed.

Background Measurements

The N_2 background signal was measured at 50, 200, and 760 torr. The results of the background signal measurements in all three modes of operation are summarized in Table 6.1.

TABLE 6.1. SUMMARY OF THE BACKGROUND SIGNAL MEASUREMENTS.

Total Pressure p_A (torr)	Mode	Pol.	ac Stark Voltage v_s (V P-P)	N_2 Background Signal
760	Chopped	Vert.	-	2.34 mV/W
		Horiz.	-	1.47
	Stark Volt.	indep.	10	< 1 μV
	Stark Pol.	-	-	0.90 mV/W
200	Chopped	Vert.	-	0.83 mV/W
		Horiz.	-	0.49
	Stark Volt.	indep.	10	< 1 μV
	Stark Pol.	-	-	0.37 mV/W
50	Chopped	Vert.	-	0.28 mV/W
		Horiz.	-	0.15
	Stark Volt.	indep.	10	< 1 μV
	Stark Pol.	-	-	0.094 mV/W

As in the other modes, the background signal in the rotating polarization mode was independent of the dc Stark voltage. Its magnitude was proportional to the difference in the horizontal and vertical polarization chopped-mode background signals. Thus we may eliminate the rotation mechanism of the half-wave plate as the

primary source of the background signal. At 50 torr, the largest signal-to-background ratio was 127.8 at 400 V and the minimum detectable change in attenuation coefficient, $\tilde{\alpha}$, was 3.4×10^{-5} cm^{-1}. At 200 torr, the same quantities were 57.8 at 400 V and 4.8×10^{-5} cm^{-1}.

The background signal may have been caused by polarization dependent absorption by the ZnSe windows. This is conceivable if the windows experienced strain as they were epoxied to the spectrophone. A second possible cause is the polarization dependent reflection coefficient at each window surface due to the nonzero angle of incidence. This would affect the pattern and intensity of the multiple beam reflections within the cell and thus would affect the total absorption of the beam.

6.4 Chapter 6 References

[1] M.J. Kavaya and J.S. Margolis: "Low-Noise Spectrophone", NASA Tech Briefs 4, No. 1, 46(Spring 1979)

[2] M.J. Kavaya, J.S. Margolis, and M.S. Shumate: "Optoacoustic Detection Using Stark Modulation", paper presented at the OSA topical conference on Photoacoustic Spectroscopy in Ames, Iowa on August 1, 1979

7. SUMMARY AND CONCLUSIONS

An introduction to the principle of optoacoustic detection and a historical sketch of the field was provided. A simple theory was developed for the signal generation and detection in the conventional chopped laser radiation mode of operation. The limiting background signal was discussed and expressions were derived for some of the expected contributions to the background signal. Two novel techniques of optoacoustic detection, Stark voltage modulation and Stark polarization modulation, were then discussed and experimental results were reported. The optoacoustic detector, or spectrophone, which allowed operation in all three modes, was described. The results of the three modes of operation were compared. This comparison was enhanced by the concurrent operation in all three modes using the same spectrophone, gas fill, and experimental conditions.

Chopped-mode operation of the spectrophone closely followed theoretical predictions. The spectrophone responsivity increased with increasing pressure with a 13 Hz modulation frequency and generally decreased with increasing modulation frequency. It was independent of the cell volume over the range of volume of our two spectrophones (1.36 - 3.39 $\times$ 10^{7} m^{3}). The variation with frequency and pressure of the background signal could also be explained over the range of validity of the theory. It increased with increasing pressure at 13 Hz, decreased with increasing modulation frequency, and decreased with increasing cell volume. Both the signal and the background were proportional to laser power.

The Stark voltage modulation mode of operation resulted in an order of magnitude improvement in the signal-to-background ratio and over two orders of magnitude improvement in the minimum detectable change in absorption. Even better performance should be possible by increasing the laser power. The Stark voltage modulation mode background signal was independent of laser power, laser polariza-

tion, and the dc Stark voltage.

The Stark polarization modulation mode did not perform as well as expected. Both the signal-to-background ratio and the minimum detectable absorption were poorer than in the chopped mode. Again, the background signal was independent of the dc Stark voltage.

Both the Stark voltage modulation and the Stark polarization modulation signals exhibited a unique signature of the molecule which could be used to discriminate against interfering molecules. These signatures were explained from the chopped-mode signal profile. Both new modes of modulation are better suited to lower pressure operation, which is limited by electrical breakdown between the Stark electrodes and the decreasing cell responsivity with decreasing pressure.

Two new methods of operating spectrophones have been demonstrated successfully. However, much more work is needed to investigate fully all of the areas mentioned in this report. A three-dimensional theory is needed which applies at low modulation frequencies where the thermal diffusion length in the gas is on the order of the cell dimensions. More experiments, which cover greater frequency and pressure ranges, are desirable to understand the behavior of the signal and the background signal. The effect of the cell and microphone volumes and their ratio could be investigated. Experiments which better identify the source of the background signal in all three modes would be of interest. The Stark modulation mode signal and background signal dependence on the magnitude and frequency of the ac Stark voltage is desirable. An electret microphone could be used instead of the condenser microphone, thus eliminating the bias voltage and the noisy dc to dc converter, and greatly reducing the microphone volume. Combining the electret microphone with a low-noise preamplifier and reducing the sources of nonfundamental noise should allow measurement of the actual limiting background signal and noise.

APPENDIX A

DERIVATIVE DETECTION

Consider a general experimental configuration where the measured signal is dependent on one or more parameters and is periodic in time due to a sinusoidal modulation of one of the parameters. For example, the absorption of monochromatic laser radiation by some gases may be modulated by sinusoidally varying the laser frequency ,ν, or by varying the center frequency ,ν_0, of the absorption line cross section, σ, through the application of a sinusoidal electric field to the gas. If $\sigma(\nu)$ possesses derivatives of all orders in the neighborhood of ν_0, then $\sigma(\nu)$ may be expanded in a Taylor series:

$$\sigma(\nu) = \sigma(\nu_0) + \frac{(\nu-\nu_0)}{1!}\sigma'(\nu_0) + \frac{(\nu-\nu_0)^2}{2!}\sigma''(\nu_0) + \cdots = \sum_{n=0}^{\infty} C_n(\nu-\nu_0)^n \quad , \qquad (A.1)$$

where

$$C_n = \frac{\sigma^{(n)}(\nu)}{n!} \quad \text{at } \nu = \nu_0 \quad . \qquad (A.2)$$

If we define γ as a characteristic frequency of the absorption cross section, such as the half-width at half-maximum (HWHM) of a Lorentzian absorption line, then the modulation is described by

$$\nu - \nu_0 = \beta\gamma + m\gamma\sin\omega t \quad , \qquad (A.3)$$

where β and m are dimensionless offset and modulation amplitude parameters, ω is the modulation frequency, and the peak-to-peak frequency modulation is $2m\gamma$. Thus equation (A.1) becomes

$$\sigma(\nu) \rightarrow \sigma(\beta, m, t) = \sum_{n=0}^{\infty} C_n \gamma^n (\beta + m \sin\omega t)^n$$

$$= \sum_{n=0}^{\infty} C_n \gamma^n \Big[\beta^n + n\beta^{n-1} m \sin\omega t + \frac{n(n-1)}{2!} \beta^{n-2} m^2 \sin^2\omega t$$

$$+ \frac{n(n-1)(n-2)}{3!} \beta^{n-3} m^3 \sin^3\omega t + \cdots \Big] \quad . \tag{A.4}$$

Using the relations

$$\sin^2\omega t = \frac{1}{2} - \frac{1}{2} \cos\omega t \tag{A.5}$$

and

$$\sin^3\omega t = \frac{3}{4} \sin\omega t - \frac{1}{4} \sin 3\omega t \quad , \tag{A.6}$$

equation (A.4) becomes

$$\sigma(\beta, m, t) = \sum_{n=0}^{\infty} C_n \gamma^n \Big[\beta^n + n\beta^{n-1} m \sin\omega t + \frac{n(n-1)}{2!} \beta^{n-2} m^2 \left(\frac{1}{2} - \frac{1}{2} \cos 2\omega t \right)$$

$$+ \frac{n(n-1)(n-2)}{3!} \beta^{n-3} m^3 \left(\frac{3}{4} \sin\omega t - \frac{1}{4} \sin 3\omega t \right) + \cdots \Big] \quad . \tag{A.7}$$

SYNCHRONOUS DETECTION AT ω

If the signal is phase-synchronously detected at the fundamental frequency ω, then only the $\sin\omega t$ and $\cos\omega t$ terms in (A.7) contribute and it becomes:

$$\sigma(\beta, m, t) \rightarrow \sum_{n=0}^{\infty} C_n \gamma^n \Big[n\beta^{n-1} m \sin\omega t + \frac{n(n-1)(n-2)}{3!} \beta^{n-3} m^3 \frac{3}{4} \sin\omega t + \cdots \Big] \quad . \tag{A.8}$$

If $m << 1$, then

$$\sigma(\beta, m, t) \rightarrow \sum_{n=0}^{\infty} C_n \gamma^n n \beta^{n-1} m \sin\omega t \quad . \tag{A.9}$$

Differentiating (A.1) and letting $\nu - \nu_0 = \beta\gamma$, we find that

$$\sigma'(\beta\gamma) = \sum_{n=0}^{\infty} C_n n (\beta\gamma)^{n-1} \quad . \tag{A.10}$$

From (A.9) and (A.10) we see that the synchronous in-phase (sin) amplitude at ω ,σ^{ω}, is related to the first derivative of the absorption curve by

$$\sigma^{\omega}(\beta, m) = m\gamma\sigma' \quad , \tag{A.11}$$

as long as $m << 1$. The signal is linearly proportional to the modulation amplitude m, the HWHM γ, and the first derivative of the absorption curve.

SYNCHRONOUS DETECTION AT 2ω

It is also possible to phase-synchronously detect the signal (A.7) at harmonics of the fundamental frequency ω. The most common case is detection at 2ω. Keeping only the $\sin 2\omega t$ and $\cos 2\omega t$ terms, (A.7) becomes:

$$\sigma(\beta, m, t) \rightarrow \sum_{n=0}^{\infty} C_n \gamma^n \left[\frac{-n(n-1)}{2!} \beta^{n-2} m^2 \frac{1}{2} \cos 2\omega t + \cdots \right] \quad . \tag{A.12}$$

Again we let $m << 1$ and retain only the first term in (A.12). Taking the second derivative of (A.1) and letting $\nu - \nu_0 = \beta\gamma$, we see that the synchronous quadrature (cosine) amplitude at 2ω ,$\sigma^{2\omega}$, is related to the second derivative of the absorption curve by

$$\sigma^{2\omega}(\beta, m) = \frac{-m^2\gamma^2}{4}\sigma'' \quad . \tag{A.13}$$

This signal is quadratic in m and γ, is linearly proportional to the second derivative of the absorption curve, and is usually smaller than the ω signal.

MODULATION BROADENING

From (A.11) and (A.13), we see that the signal may be increased by increasing m, the modulation amplitude parameter. However, this will eventually violate the assumption that $m << 1$, and the signal will no longer be proportional to the derivative of the absorption curve. To see this effect, we will consider the case of a single Lorentzian absorption line (see Table A.1):

$$\sigma(\nu) = \frac{S}{\pi}\frac{\gamma}{(\nu - \nu_0)^2 + \gamma^2} \quad . \tag{A.14}$$

Substituting (A.3) into (A.14), we get

$$\sigma(\beta, m, t) = \frac{S}{\pi\gamma}\frac{1}{(\beta + m\sin\omega t)^2 + 1} \quad . \tag{A.15}$$

The in-phase ω component and the quadrature 2ω component of $\sigma(\beta, m, t)$ are found by Fourier series analysis to be

$$b_1 = \frac{2}{T}\int_{-\frac{T}{2}}^{\frac{T}{2}} \frac{S}{\pi\gamma}\frac{\sin\omega t}{(\beta + m\sin\omega t)^2 + 1}dt \quad , \tag{A.16}$$

and

TABLE A.1. THE LORENTZIAN LINESHAPE AND ITS DERIVATIVES.

Symbol	Function	Maxima
Lorentzian Lineshape		
$\sigma(\nu)$	$\frac{S}{\pi}\frac{\gamma}{(\nu-\nu_0)^2+\gamma^2}$	$\frac{S}{\pi\gamma}$ at $(\nu-\nu_0)=0$
$\frac{d}{d\nu}\sigma(\nu)$	$\frac{-2(\nu-\nu_0)}{[(\nu-\nu_0)^2+\gamma^2]}\sigma(\nu)$	$-\frac{\pm 9S}{8\sqrt{3}\ \pi\gamma^2}$ at $(\nu-\nu_0)=\pm\frac{\gamma}{\sqrt{3}}$
$\frac{d^2}{d\nu^2}\sigma(\nu)$	$\frac{2[3(\nu-\nu_0)^2-\gamma^2]}{[(\nu-\nu_0)^2+\gamma^2]^2}\sigma(\nu)$	$\frac{-2S}{\pi\gamma^3}$ at $(\nu-\nu_0)=0$ $\frac{S}{2\pi\gamma^3}$ at $(\nu-\nu_0)=\pm\gamma$
$\frac{d^3}{d\nu^3}\sigma(\nu)$	$\frac{24(\nu-\nu_0)[\gamma^2-(\nu-\nu_0)^2]}{[(\nu-\nu_0)^2+\gamma^2]^3}\sigma(\nu)$	

$$a_2 = \frac{2}{T}\int_{-\frac{T}{2}}^{\frac{T}{2}} \frac{S}{\pi\gamma}\,\frac{\cos 2\omega t}{(\beta + m\sin\omega t)^2 + 1}\,dt \quad . \tag{A.17}$$

These integrals can be numerically evaluated and plots of $\frac{\gamma b_1}{S}$ and $\frac{\gamma a_2}{S}$ vs. β for various values of m are given in Figures A.1 and A.2. In addition to a larger signal as m increases, the curves broaden in the horizontal or frequency dimension. As the modulation amplitude increases, the coordinate yielding the maximum signal at ω moves further away from the linecenter. The horizontal axis is marked at the values $\beta = \pm \frac{1}{\sqrt{3}} = \pm 0.577$. This is where the true peaks of the first derivative and the zero-crossings of the second derivative should occur for a Lorentzian lineshape. The ω and 2ω signals approach this behavior in the limit as $m \to 0$.

A second common case is the Doppler lineshape (see Table A.2):

$$\sigma(\nu) = \frac{S}{\gamma}\left[\frac{\ln 2}{\pi}\right]^{\frac{1}{2}} \exp\left\{\frac{-(\nu - \nu_0)^2 \ln 2}{\gamma^2}\right\} \quad . \tag{A.18}$$

The peaks of the first derivative and the zero-crossings of the second derivative occur at $\beta = \pm \frac{1}{\sqrt{2\ln 2}} = \pm 0.85$. Figures A.3 and A.4 show plots of $\frac{\gamma b_1}{S}$ and $\frac{\gamma a_2}{S}$ for the Doppler case.

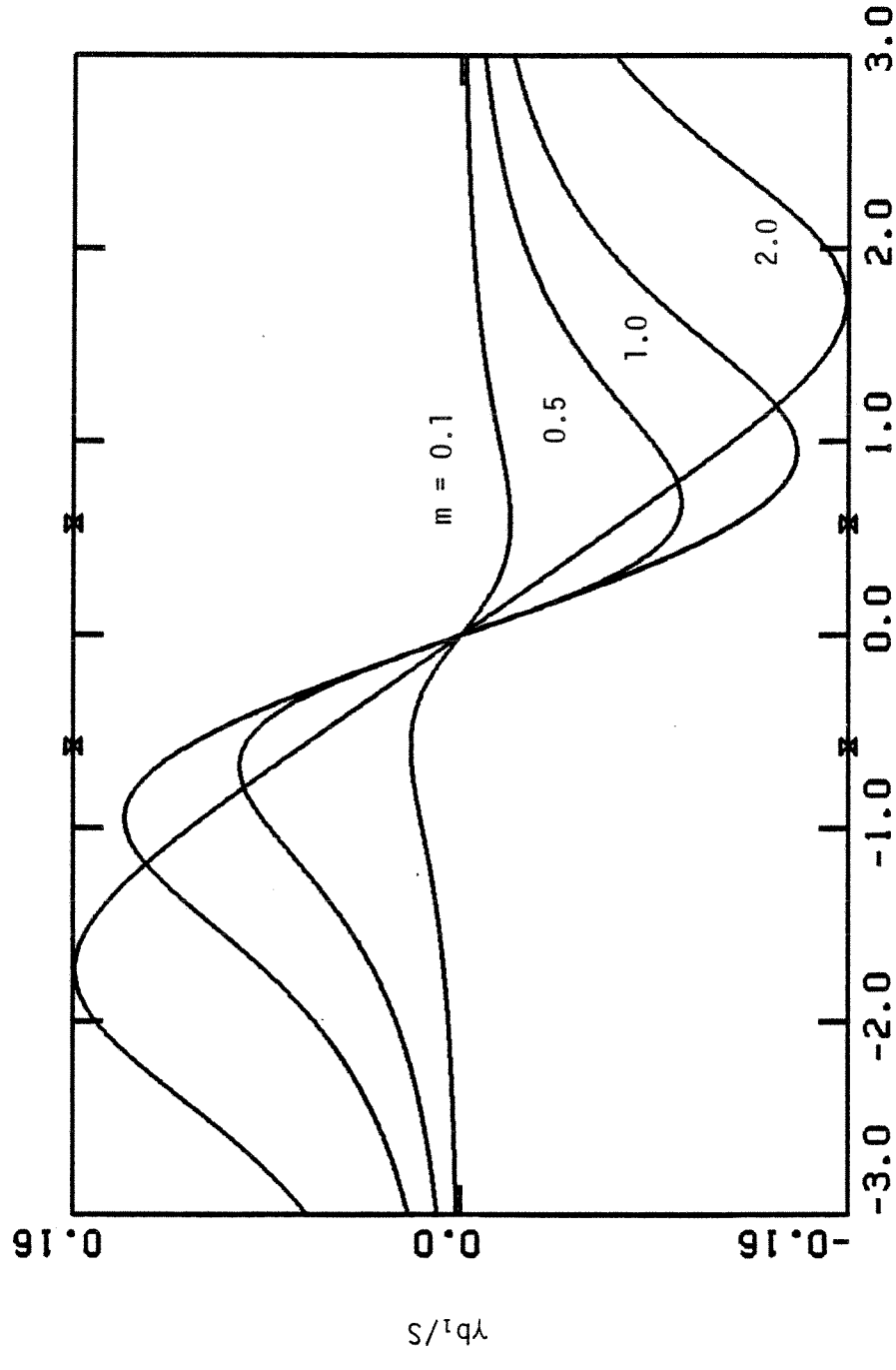

Figure A.1. Lorentzian lineshape in-phase signal at ω vs. the linecenter offset parameter for various values of the modulation amplitude parameter.

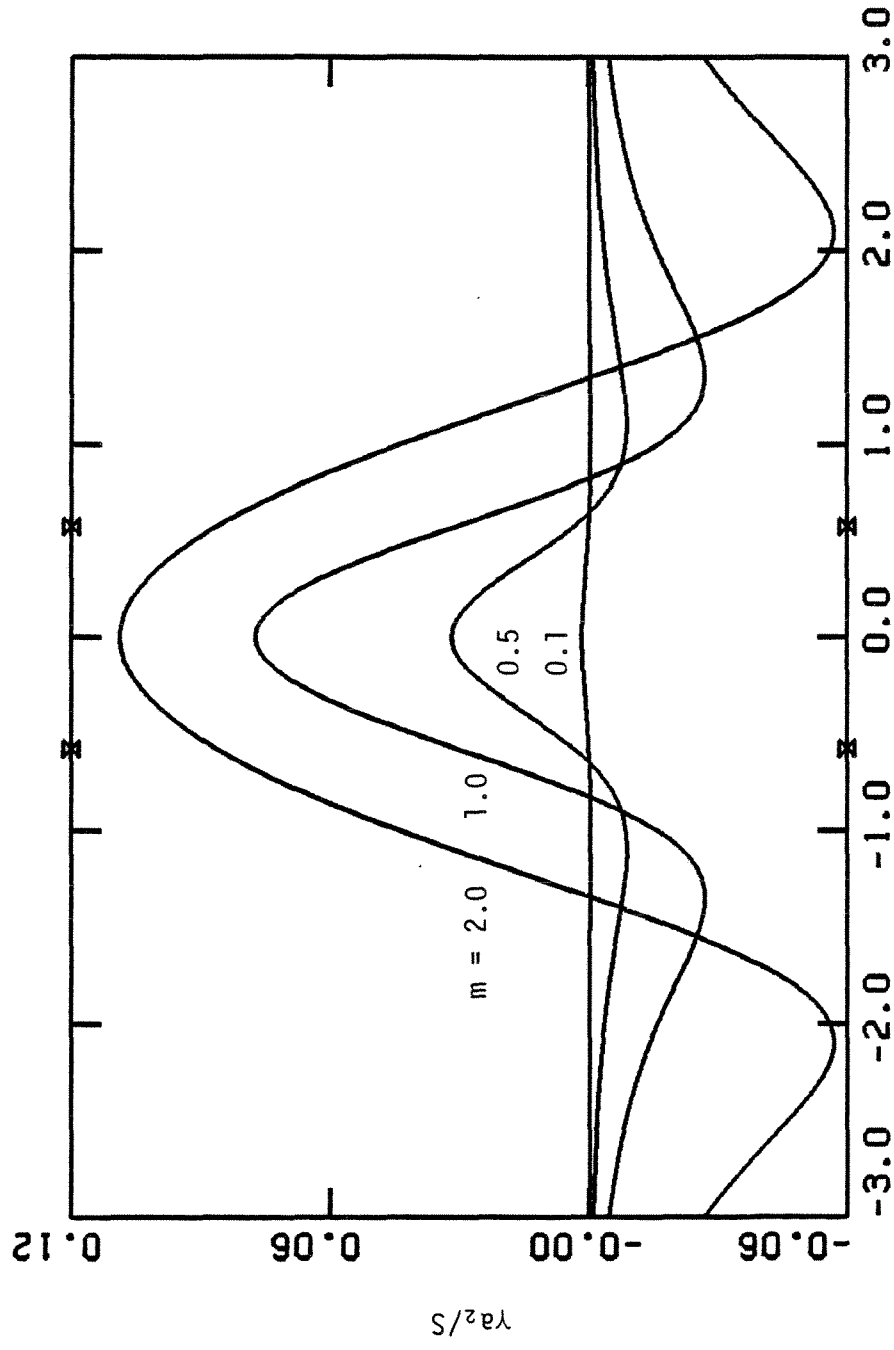

Figure A.2. Lorentzian lineshape quadrature signal at 2ω vs. the linecenter offset parameter for various values of the modulation amplitude parameter.

TABLE A.2. THE DOPPLER LINESHAPE AND ITS DERIVATIVES.

Symbol	Function	Maxima
Doppler Lineshape		$\frac{S}{\gamma}\left[\frac{\ln 2}{\pi}\right]^{\frac{1}{2}}$
$\sigma(\nu)$	$\frac{S}{\gamma}\left[\frac{\ln 2}{\pi}\right]^{\frac{1}{2}} \exp\left\{-\frac{(\nu-\nu_0)^2 \ln 2}{\gamma^2}\right\}$	at $(\nu-\nu_0) = 0$
		$-\frac{\pm S \ln 2}{\gamma^2}\left[\frac{2}{\pi e}\right]^{\frac{1}{2}}$
$\frac{d}{d\nu}\sigma(\nu)$	$\frac{-2 (\ln 2) (\nu-\nu_0)}{\gamma^2}\sigma(\nu)$	at $(\nu-\nu_0) = \frac{\pm\gamma}{\sqrt{2 \ln 2}}$
		$\frac{-2S(\ln 2)^{\frac{3}{2}}}{\gamma^3 \sqrt{\pi}}$
		at $(\nu-\nu_0) = 0$
$\frac{d^2}{d\nu^2}\sigma(\nu)$	$\left[\frac{2 \ln 2}{\gamma^2}\right]\left[\frac{2 \ln 2 (\nu-\nu_0)^2}{\gamma^2} - 1\right]\sigma(\nu)$	$\frac{4S(\ln 2)^{\frac{3}{2}}}{\gamma^3 \sqrt{\pi}\, e^{\frac{3}{2}}}$
		at $(\nu-\nu_0) = \pm\left[\frac{3}{2 \ln 2}\right]^{\frac{1}{2}}\gamma$
$\frac{d^3}{d\nu^3}\sigma(\nu)$	$\left[\frac{4(\ln 2)^2(\nu-\nu_0)}{\gamma^4}\right]\left[3 - \frac{2 \ln 2 (\nu-\nu_0)^2}{\gamma^2}\right]\sigma(\nu)$	

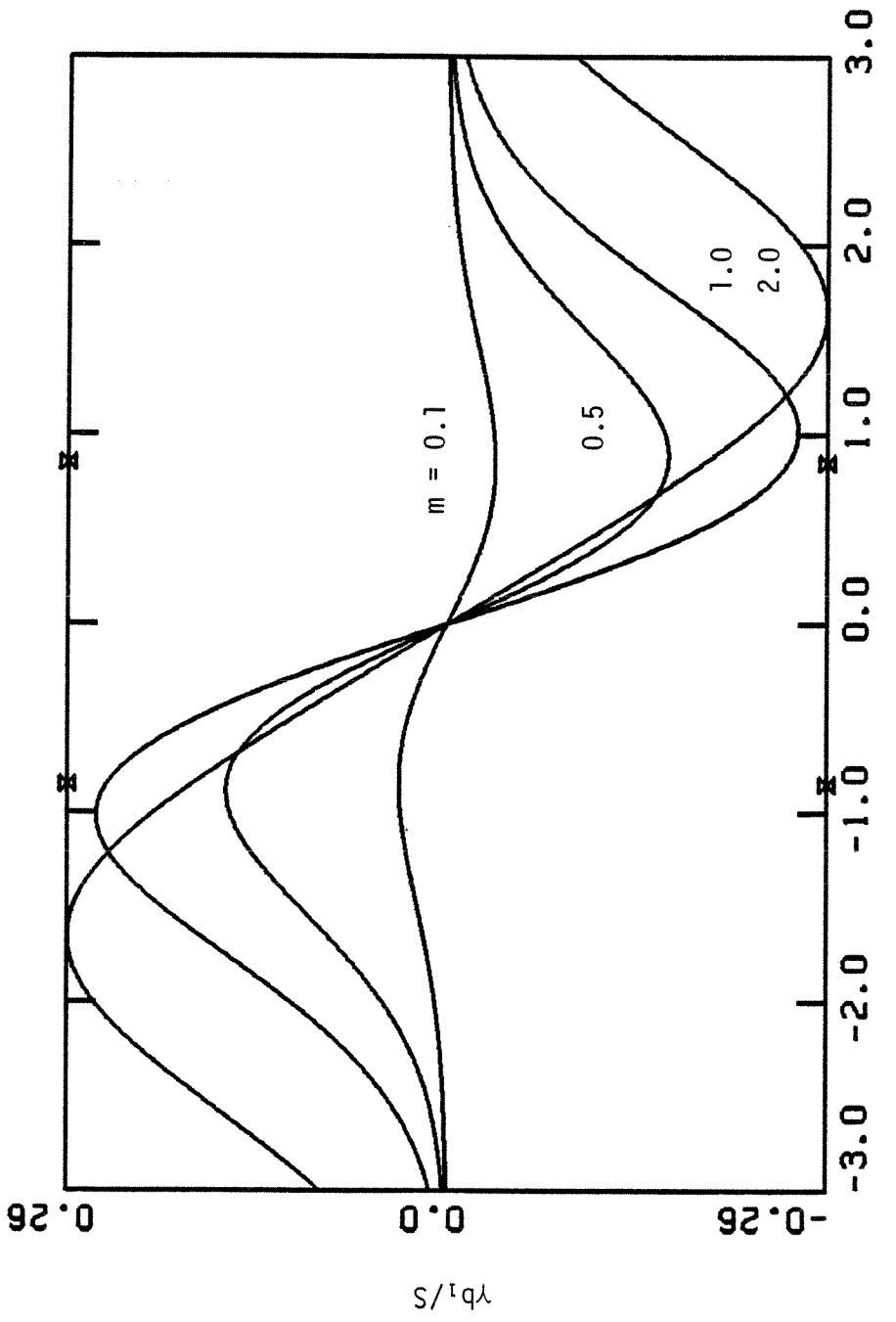

Figure A.3. Doppler lineshape in-phase signal at ω vs. the linecenter offset parameter for various values of the modulation amplitude parameter.

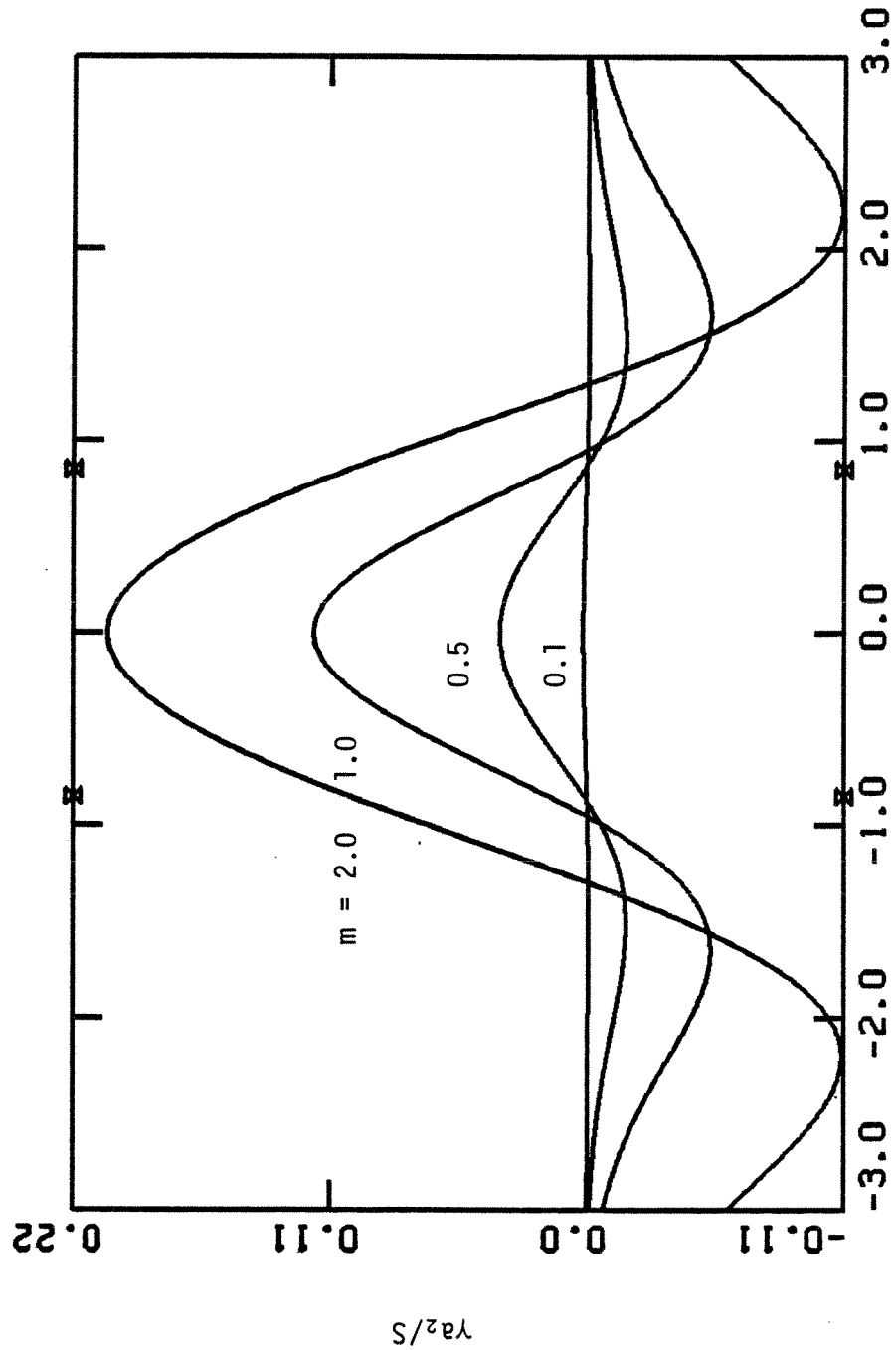

Figure A.4. Doppler lineshape quadrature signal at 2ω vs. the linecenter offset parameter for various values of the modulation amplitude parameter.